DETECTION OF HIGH ENERGY COSMIC RAY SHOWERS BY ATMOSPHERIC FLUORESCENCE

by

Peter G. Halverson

A Dissertation Submitted to the Faculty of the

DEPARTMENT OF PHYSICS

In Partial Fulfillment of the Requirements
For the Degree of

Doctor of Philosophy

In the Graduate College

THE UNIVERSITY OF ARIZONA

1989

STATEMENT BY AUTHOR

This thesis has been submitted in partial fulfillment of requirements for an advanced degree at The University of Arizona and is deposited in the University Library to be made available to borrowers under rules of the library.

Brief quotations from this thesis are allowable without special permission, provided that accurate acknowledgment of source is made. Requests for permission for extended quotation from or reproduction of this manuscript in whole or in part may be granted by the head of the major department or the Dean of the Graduate College when in his or her judgment the proposed use of the material is in the interests of scholarship. In all other instances, however, permission must be obtained from the author.

SIGNED: _____

APPROVAL BY THESIS DIRECTOR

This thesis has been approved on the date shown below:

_____ _____

Theodore Bowen
Professor of Physics

Date

ACKNOWLEDGMENTS

I would like to thank Professor Theodore Bowen who gave me the opportunity, support and guidance that made this experiment possible.

I would also like to thank the following persons who helped in the design and construction of the Side Looking detector:

Dr. Richard Cordaro Charles Bridges
Steven Syracuse Paul DesJarlais
Martha Damento

Thanks also are due to John Saba, Academic Computing Specialist at the University of Arizona Center for Computing and Information Technology, and the unknown person(s) at University of British Columbia who provided prototype LaTeXprograms for formatting PhD dissertations, and to Joe Chuma and Corrie Kost at TRIUMF who provided the PLOTDATA software package which drew the majority of the data curves in this dissertation.

Finally, I would like to thank Bill McGibbon, owner of the Santa Rita Ranch, for allowing us to locate the Side Looking Detector on his land.

Table of Contents

List of Figures

List of Tables

Chapter 1

Introduction

1.1 UHE Cosmic Rays: Why should we study them?

1.1.1 Definitions

Cosmic rays are subatomic particles such as protons, helium nuclei, electrons and gamma rays that are constantly impinging on the top of the earth's atmosphere. The measured energies of these particles range from as low as 10 MeV to as high as 10^{20} eV. [1] Note that 10^{20}eV is an impressive amount of energy for a subatomic particle, about 16 Joules! For the purposes of this dissertation, we shall call cosmic rays with E>10^{15} eV Ultra High Energy (UHE) cosmic rays.

In the following sections we will be referring often to figure 1.1 which was derived from reference [1]. It depicts the integral energy spectrum of cosmic rays as they impinge upon the earth's atmosphere. The horizontal axis is the energy of the particles, and the left vertical axis is the intensity, in events per second per meter^2 per steradian, of all particles of that energy *and higher*. For example, a detector with an acceptance of 1 m^{2}sr would see a particle of energy 10^{18} eV or higher once every 10^{12} seconds, on average. The right vertical axis is also the flux, but in more practical units (for UHE events) of events per year per km^2 per steradian. Portions of the line that are double represent the current disagreement between different experiments.

[1] Due to the high energies involved, we have run out of nomenclature for expressing the energies. Standard usage has 10^9 eV=1 GeV, 10^{12} eV=1 TeV. Recently introduced notation has 10^{15} eV=1 PeV and 10^{18} eV=1 EeV.

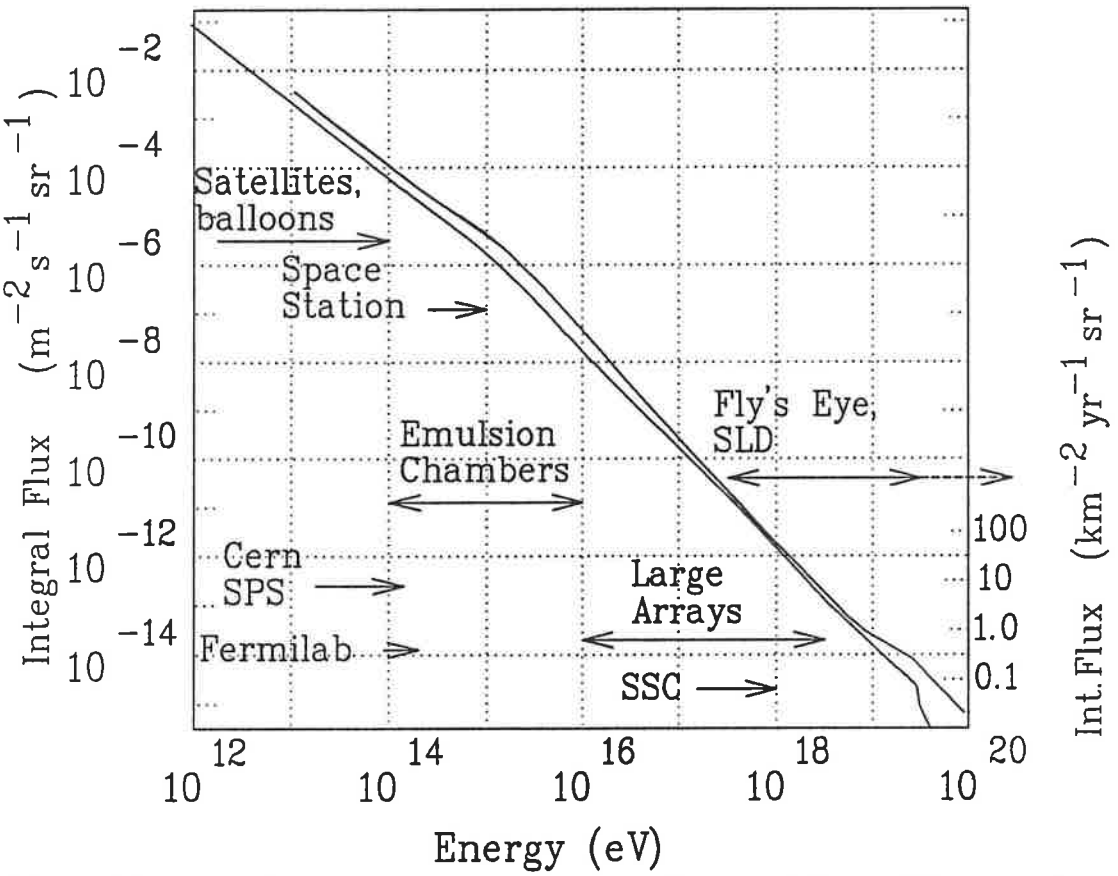

Figure 1.1: Integral spectrum of cosmic rays at the top of the earth's atmosphere.

1.1.2 The Astrophysical Interest in UHE Cosmic Rays

For the more moderate energy cosmic rays, those with energies less than 10^{15} eV, the question of where they come from and how they are created and accelerated is not very difficult to explain, although many of the details will remain unclear until more data, especially data of the type available from space-borne experiments, is available. Most of the information in this section is from Longair's text [2].

Briefly, for the lower energies, possible sources of cosmic rays include the expanding shock wave around a supernova, the "wound up" rotating magnetic fields around pulsars and magnetohydrodynamic turbulence in the plane of the galaxy. These mechanisms have been shown to be plausible sources of the observed energy spectrum up to 10^{17} eV, and of the relative chemical abundances which have been measured in satellite experiments up to energies of 100 TeV.

The spectrum of cosmic rays continues to higher energies, however, and this fact presents a challenge to our understanding of astrophysics and the fundamental rules of physics at very high energies. The basic problem is that if the highest energy particles ($E > 10^{19}$ eV) were produced within our galaxy, we would expect to see an increase of the flux of these particles in the direction of the sources; sources that would likely be concentrated at the galactic core. This enhancement has not been seen. In fact the cosmic ray flux is extremely isotropic at all energies (except, of course, for the lowest sun-produced energies).

To account for the observed isotropy two types of explanation are usually put forth. (1) The highest energy sources are distributed throughout the universe, outside the galaxy. Or (2), the highest energy cosmic rays are produced in an as yet unseen shock which would surround the galaxy at a distance on the order of 10 kpc [2].

[2] A parsec (pc) is equal to 3.26 light years. The radius of the galactic disk is about 15 kpc, its thickness is about 600 pc.

Neither explanation is free of serious problems. Explanation (1) suffers from the enormous energies implied by the distances involved. Unless the hypothetical extragalactic sources are somehow beaming the high energy particles toward us, the amount of energy required of these sources would be fantastic. It has been estimated that since their formation, the observed active galaxies (such as Seyfert galaxies and quasars) or normal galaxies with active cores would have had to convert 10% of their rest mass into high energy cosmic rays to fill the universe with the locally measured cosmic ray energy density of 1 eV/cm^3. (Neutron stars achieve 1% conversion efficiency via gravitational collapse.) In view of these large energy requirements, some exotic sources have been proposed, such as superconducting cosmic strings [3]. The energy requirements are somewhat alleviated if the cosmic rays are confined to our galactic supercluster, but other problems remain. One of these is that for energies greater than 2×10^{19} eV, cosmic ray particles will see the photons of the high frequency tail of the 3°K background radiation greatly blue shifted. These photons will appear as hard gamma rays so that the following reactions become possible:

$$\begin{aligned} \gamma + p &\rightarrow n + \pi^+ \\ \gamma + p &\rightarrow p + \pi^0 \rightarrow p + \gamma + \gamma \\ \gamma + p &\rightarrow p + n\pi \end{aligned}$$

Consequently, one would not expect to see particles of energy higher than 5×10^{19} eV,[4] yet several such particles have been seen. On the other hand, the Fly's Eye experiment does report seeing a "cut-off" in the spectrum [5] at about 3×10^{19} eV, which lends support to the extra-galactic origin and/or local supercluster origin hypothesis [6].

The second hypothesis mentioned above, acceleration of the particles in a shock around the galaxy, also has its problems. It is quite difficult (theoretically) to construct a combination of magnetic fields, gas flows and supply of lower energy particles in a way that will reproduce the observed spectrum up to 10^{20} eV. For

example, a lower energy particle must pass through the shock zone many times, each time picking up more energy, to attain the highest energies. Yet the radius of curvature of a 10^{19} eV proton is 2 kpc in the roughly 3×10^{-6} Gauss magnetic field typical of the galaxy, making for large loops between passes through the shock. Despite the problems, progress has been made in this area by such persons as Jokipii [7], here at the University of Arizona. If this shock exists, it should be observable in the gamma ray spectrum (due to pion production from proton-gas molecule collisions), and in the radio frequencies (synchrotron radiation).

1.1.3 Elementary Particle Physics' Interest in UHE Cosmic Rays

While it is true that at lower energies ($E < 10^{14}$ eV), balloon and satellite-borne experiments have directly observed the cosmic ray particles, at higher energies the flux becomes too low for events to be seen in the limited duration and detector acceptance of such experiments.

Cosmic ray experiments on the ground can run for longer periods of time but now we are no longer observing the original particles. We are instead detecting the shower of *secondary* particles produced after the primary particle strikes the upper atmosphere. In this process (see figure 1.2) a primary proton strikes the nucleus of an air molecule producing a "spray" of mostly protons, neutrons, and pions, and, in principle, any combination of more exotic particles, as long as the rest masses are less than the available center-of-mass energy and the total charge, strangeness, and charm are conserved.

The fate of the π^+ and π^- particles depends in part on the value of $\gamma = (1 - v^2/c^2)^{-1/2}$ with which they are produced. If $\gamma \ll 10^3$ then the lifetime $\gamma\tau$ of the particles will be sufficiently short that they will decay into μ^+ and μ^- particles and their respective neutrino complements. These μ particles, being massive and weakly interacting reach and penetrate the ground where they can be easily detected by underground scintillators.

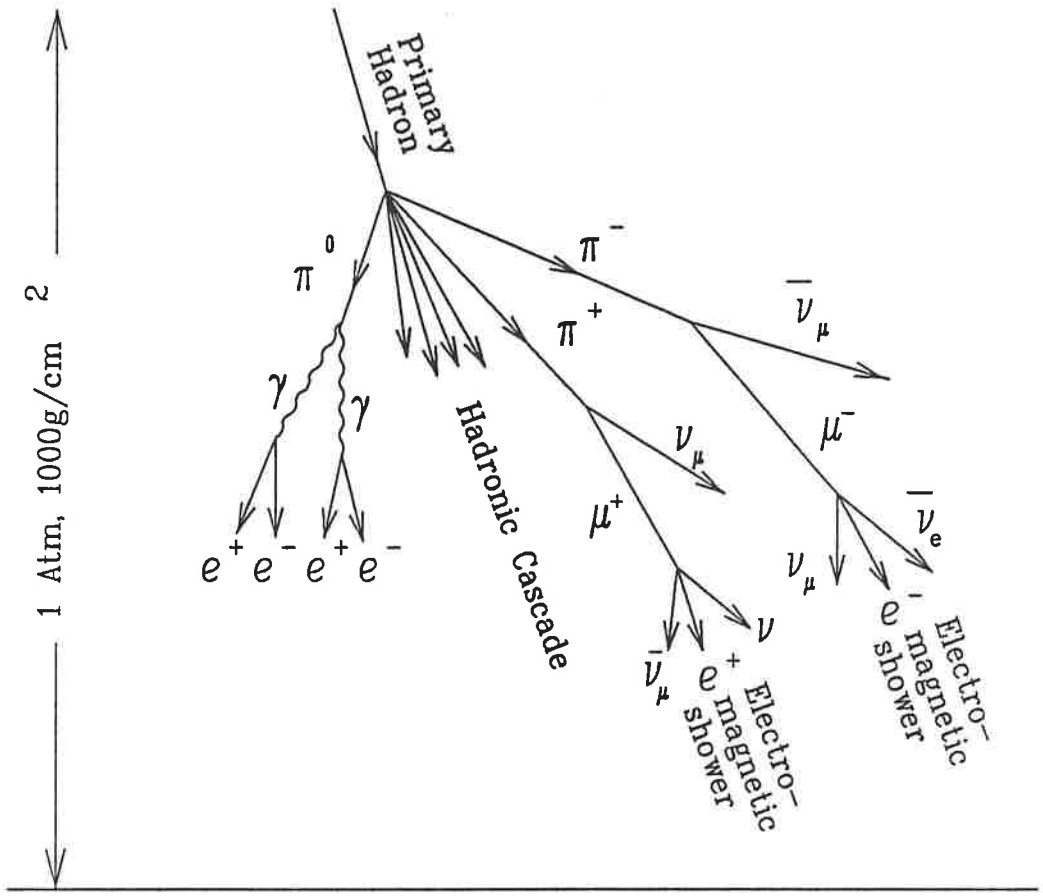

Figure 1.2: Schematic diagram of a hadronic cascade.

If, however, $\gamma \gg 10^3$ then the π^+ and π^- particles will not decay before reaching the ground but instead will form hadronic "sub-showers". The transition from one regime to the other occurs when the energy $E_\pi = \gamma m_\pi c^2 \approx 1.4 \times 10^{11}$ eV. This will begin to happen for (very roughly) primary energies greater than 10^{12} eV.

The π^0 particles decay rapidly ($\tau_{\pi^0} \approx 8 \times 10^{-17}$ sec) into a pair of gamma rays that interact electromagnetically with other nuclei further down to produce e^+e^- pairs. These will bremsstrahlung to produce gamma rays again and the

process can repeat itself thus creating an *electromagnetic cascade.* From the top of the atmosphere to the ground there is about 1000 g/cm^2 of air, which is 28 radiation lengths; thus, there can be up to $\frac{1}{3} \times 2^{28}$ e^- particles, $\frac{1}{3} \times 2^{28}$ e^+ particles, $\frac{1}{3} \times 2^{28}$ γ's for each π^0 by the time the electromagnetic showers reach sea level. (These are rough, order-of-magnitude estimates.) (Generally, there will not be enough energy to produce this many e^+e^- pairs; much of the energy goes into ionization and excitation of the air.)

As was alluded to earlier, there will be many of these showers in a typical hadronic event due to the spray of energetic nuclear fragments and fast π^+ and π^+ particles after the first and subsequent collisions. Unfortunately, due to the probabilistic nature of the nuclear fragmentation process, the actual number of showers in an event is subject to large fluctuations which makes it difficult to convert the number $N_{e\pm}$ of e^+ and e^- particles (which is what is usually measured) back to the primary energy. As a rule of thumb, one can say that at sea level, there will be roughly one particle (e^+ or e^-) for every 3 GeV of energy in the electromagnetic cascades. The reader can look forward to figures 3.1 and 3.2 to check this generalization.

In some cases, the primary particle in an electromagnetic cascade will be a gamma ray, instead of a proton or other hadron. In this situation, the gamma being just a high energy photon has a low cross section for producing π's in the first interaction; therefore, a gamma induced cascade will contain mostly γ, e^+ and e^- particles. Monte-Carlo cascade simulations predict that gamma-induced showers should have $< \frac{1}{10}$th the muon content of hadronic showers. Thus so-called muon-poor cascades are assumed to be due to gamma primaries in the current generation of gamma-ray telescopes. These devices have managed to detect pulsars such as Cygnus X-3 and Hercules X-1 in the light of 10^{14} eV gamma rays [8]. This type of astronomy is not possible with charged cosmic rays, such as protons, due to the deflection of these particles by the magnetic fields present in the galaxy. Yet even this point has become controversial as will be explained below.

Historically, the early development of elementary particle physics was made possible by the "free" source of particles in the cosmic ray showers. Particles that have been discovered in cosmic ray experiments are listed below:

1932–1947	e^+, μ, π
1948	K^+, K^-
1951–1953	Λ,Ξ^-, K^0, Σ^+
1988	mystery particles in muon-rich gamma showers?

Getting back to gamma ray astronomy, the last entry in the preceding table refers to a recent development in that field [8]. As mentioned above, gamma induced showers should be deficient in muons at the ground level. Also, if one sees a point source of cosmic ray events, it presumably has to be a source seen in the "light" of neutral particles such as gamma rays since an image seen in the "light" of protons or other charged particles would be blurred by magnetic fields. Neutral atoms are ruled out due to electron stripping by interstellar gas enroute. Neutrons are ruled out mostly because they would β-decay before reaching us. The most likely and expected particle, γ rays, have difficulty because of the amazing discovery that the high energy showers contain far too many muons, by at least an order of magnitude, to be compatible with present theories of particle interaction [9].

Assuming the data provided by the experiments is to be trusted, it seems we are left with two exotic possibilities: (1) the particles we are seeing are something new or (2) the present theories that predict muon poor cascades begin to break down at these energies ($E \approx 10^{14}$ eV).

Considering the above questions, it appears the we must try to improve our understanding and capabilities in the following areas:

- Searching for point sources of high energy cosmic rays.

- Searching for cosmic ray particles with energies greater than 10^{20} eV and gathering enough data to unambiguously plot the energy spectrum at lower energies.
- Studying the details of cascade development at ultra-high energies.

The first two items are problems for which the Side Looking Detector that this dissertation describes is well suited. The last item will require imaging of the entire cascade, something which only the Fly's Eye can presently accomplish.

1.2 Detection of UHE Cosmic Rays

The detection of cosmic rays has a long history and many types of detector. This section assumes the reader is familiar with basic particle detection techniques, however, the author has included Appendix C which offers a brief review.

UHE cosmic ray experiments have special problems that have driven the evolution of detectors as will be discussed below.

First, and most obviously, UHE experiments have to be big. As experiments have sought to extend the observed primary spectrum to increasingly high energies, the integral flux (the flux of all particles with energy greater than E) has rapidly fallen off. Below 10^{15}eV, the flux scales as $E^{-1.6}$. Referring back to figure 1.1, we can see that for energies above the "knee" at 10^{15} eV, the flux of cosmic rays falls off even more rapidly. It becomes proportional to $E^{-2.5}$. So for each ten-fold increase in energy, the flux of particles goes down by a factor of about 300. By the time we get up to 10^{19} eV, the flux has dropped to less than one particle per year per km^{2}sr. To do cosmic ray astronomy at 10^{20} eV with a signal of more than 10 particles per year, one would need a detector of 3000 km^{2}sr acceptance.

The next requirement that has driven detector design has been the need to determine the direction from which the primary particles originate. For large

scintillator arrays this has meant the inclusion of high speed electronic timers to measure the relative arrival time of the shower front. From this data the shower axis position and orientation can be determined. In the case of the Fly's Eye and the SLD detectors which see an image of the shower in the atmosphere, the position and orientation of the shower axis is obtained by imaging from two widely separated positions to get a stereoscopic 3-D view.

A third and most challenging requirement is the need to know the composition of the primary particles. In the case of the large scintillator arrays this has been partially met by adding underground scintillators that are sensitive only to the muon content of the showers. This at least allows differentiation of hadron primaries from gamma primaries. A potentially more effective solution is provided by the Fly's Eye which has the capability of imaging the entire evolution of the cascades. The start depth in the atmosphere and rate at which a cascade evolves yields information on the primary particle's composition. A recent development has been the combination of large above-ground and underground scintillator arrays with the Fly's Eye system which should provide even more accurate composition data. Also, another Fly's Eye with greater angular resolution is currently under construction.

It should be noted that the interpretation of the data for the cosmic ray primary composition depends on our understanding of particle interactions at energies many orders of magnitude high than is available from accelerators. Even the proposed Superconducting Super Collider will produce collisions orders of magnitude less energetic than currently observed cosmic ray events. So the determination of the primary composition will require understanding the high energy interactions; yet this understanding will have to be obtained from the same scintillator arrays and Fly's Eye detectors. This makes it only more important to be able to obtain detailed information on the cascade evolution.

The Side Looking Detector, which is described in the next chapter, addresses two of the above concerns. It achieves a very large detector area for moderate cost, making the detection of events above 10^{20} eV feasible. It also allows the determination of the shower axis so we will know the direction from which the primaries are coming. It should be pointed out that the higher the energy, the less the galactic magnetic fields will deflect particles, so at 10^{21} eV, even charged particles will begin to allow some imaging of the cosmic ray sources, a feat that thus far has been reserved to gamma-ray detectors.

1.3 Air Fluorescence Detection of Cascades

As mentioned in the previous section and summarized in appendix C, cosmic ray cascade detection has evolved towards larger collection areas culminating with the Fly's Eye which uses the air fluorescence detection technique. This is also the approach on which the present research is based.

Principle: The electromagnetic cascade of a UHE event ionizes the nitrogen in the atmosphere creating N_2^+ ions which de-excite and emit light in the near ultraviolet spectrum. This light is collected to form an image of the cascade as it progresses down through the atmosphere. The pioneers in this technique were the Cornell University group of Kenneth Greisen, in particular, who worked 10 years on this approach, but without success [10] [11]. The first working example of this approach is the Fly's Eye experiment in Utah [12] [13], and now the Side Looking Detector (SLD), which is the basis of this dissertation.

Work has also been done by Elliot [14] and Bhat [15], in the closely related area of the detection of cosmic X-rays by the observation of flashes of high altitude air fluorescence.

1.3.1 Air Fluorescence Detection of Cascades with the Fly's Eye

As mentioned earlier the idea of using atmosphere as a scintillator for detecting cosmic rays appears to have originated with Kenneth Greisen whose group at Cornell built a prototype detector in Ithaca, New York [10] in 1965. Despite heroic effort on the part of the Ithaca group, the system did not detect any extensive air showers. It appears that the atmospheric conditions and overall technology available to them did not allow sufficient sensitivity [11].

The University of Utah Fly's Eye experiment, which began under the leadership of the late Professor J. Kueffel, was the first system to succeed at detecting cosmic rays by air fluorescence. The SLD is the only other detector to do this (not counting the Fly's Eye II, which is a duplicate of the first Fly's Eye). The Fly's Eye consists of 67 mirrors, each looking at a hexagonal portion of the sky. The mirrors are arranged so that the entire hemisphere is covered. The field of view of each mirror is further subdivided by an array of 12 or 14 photomultiplier tubes at the focus of each mirror. Each PMT sees a small hexagon-shaped portion of the celestial sphere.

A UHE cascade descending through the atmosphere at a typical distance ($\approx$10 km) will be detected by a linear sequence of tubes. In 1983, construction began on a second Fly's Eye, positioned 1 km away from the first, so that the image of the descending cascade could be seen in stereo, thus allowing three dimensional reconstruction.

Note that the Fly's Eye can only operate on clear, moonless nights and well away from light pollution that would obscure the weak fluorescence signal. Also, when a planet or bright star passes within the field of view of a photomultiplier tube, it must be partially turned off (the high voltage is reduced) to prevent damage to the tube.

1.4 Summary: The Need for a New Detector

If we are going to extend our knowledge of the UHE cosmic rays' origin and our understanding of particle interactions for $E \geq 10^{19}$ eV, we must build a detector with a huge acceptance $A\Omega > 1000$ km^{2}sr. We believe that a new detector design, conceptually based on the Fly's Eye but re-designed to provide roughly equal acceptance at lower cost will make such a project possible. The Side Looking Detector that this dissertation will describe is a simple device amenable to mass-production at a reasonable cost. The installation of a number (≈ 30) of SLD units would increase the world UHE cosmic ray detector area by an order of magnitude and would likely make scientific findings that are both unanticipated and significant.

Some of the key parameters of the Side Looking Detector which is described in the remainder of this paper are listed below, and for comparison purposes, similar specifications are listed for the Fly's Eye [16].

Table 1.1: Summary of Specifications of the Side Looking Detector. Data in this table is from later chapters of this dissertation.

Altitude	912 meters (2992 feet)
Atmospheric depth	915 g/cm^2
Latitude	31°52'30" North
Longitude	110°55'40" West
Number of mirrors	1
Mirror Area	4.7 m^2
Focal Length	184 cm
Tubes per mirror	6
Field of view of each tube	≈41° horizontal by .31° vertical
Total Field of view	≈41° horizontal 1.9° vertical ≈0.23 sr
Type of tube	RCA 8575
"Filter" on each tube	Bicron BBQ waveshifter, band pass from <3000 Å to 4400 Å with a peak optical efficiency of ≈ 30% at 4000 Å (Short wavelength limit due to aluminum reflectivity cutoff at ≈3400 Å)
Time resolution	25 ns
Acceptance $A\Omega$	17 km^{2}sr at 10^{18} eV 143 km^{2}sr at 10^{19}, 10^{20} eV (limited by distance of mountains)

Table 1.2: Summary of Specifications of the Fly's Eye

Altitude	1500 meters (5000 feet)
Atmospheric depth	850 g/cm^2
Number of mirrors	67
Area of each mirror	2 m^2
Focal Length	160 cm
Tubes per mirror	12 or 14
Field of view of each tube	.007 sr
Total field of view	whole sky, 2π sr
Type of tube	EMI 9861 custom tubes with UVT windows and Super S-11 cathodes.
Filter in front of each tube	UG1, band pass from 2800 Å to 4200 Å with a peak transmittance of 55% at 3550 Å (Aluminum mirror reflectivity will limit short wavelength sensitivity.)
Time resolution	25 ns
Acceptance $A\Omega$	63 km^{2}sr at 10^{18} eV 790 km^{2}sr at 10^{20} eV

Chapter 2

The Side Looking Detector

2.1 Design

The Side Looking Detector (SLD) is a system for detecting UHE cosmic ray cascades near ground level using the fluorescence of air as a natural scintillator. The overall design is shown in figure 2.1.

It consists of a large acrylic mirror, 2.4 m (8 ft) wide by 2.4 m (8 ft) tall, curved into a cylindrical parabolic shape. To improve the image quality, 18% of the mirror surface was masked off. At the resulting focal line is a system of waveshifter light pipes and photomultiplier tubes (PMTs) to detect the light from distant cosmic ray cascades. For reasons that will soon be apparent, the combination of a PMT and a waveshifter light pipe will be called a BBQ-PMT assembly.

In order to keep our expenses low, we used a novel design for our mirror. We started with two sheets of "Mir-Acryl" plastic, which consists of plexiglass, 1.2 m (4 ft) wide by 2.4 m (8 ft) tall by 0.32 cm (1/8 in) thick, on which a thin front surface layer of aluminum had been deposited. In addition, a thin layer of laquer had been sprayed onto the aluminum coating to retard corrosion and prevent scratching. The reflectivity of the aluminum-laquer combination is better than 90% at 3900 Å [17]. The mirrors started out flat but were bent into a cylindrical parabolic shape by a system of 98 adjustment screws behind the mirrors (see appendix D.1 for more detailed design information). To guide us during the

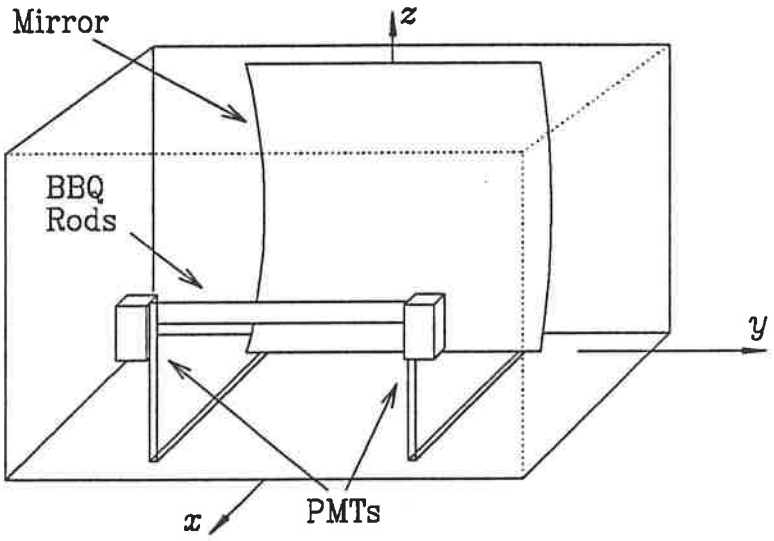

Figure 2.1: Perspective schematic view of the Side Looking Detector showing large 8 foot by 8 foot cylindrical mirror, waveshifter stack at focal line which is between the two rectangular boxes which house the photomultiplier tubes.

adjustment process, a helium-neon laser provided parallel light rays which shone on the mirror, were reflected and converged on the focal line. Any defects in the mirror could be seen as deviations from the focal line and could then be corrected by turning the mirror adjustment screws. The image quality that we achieved in this manner was such that the image of the distant laser fell on a line 10 mm wide, equal to the width of our waveshifter bars.

Because the mirrors are cylindrical, details in the left–right direction are not resolved, while details in the up–down direction are. This permits tracking a cosmic ray cascade as it descends but gives little information on its position in the left–right direction. (Complete tracking information would be available if a second detector were installed to provide stereo viewing of events.) Figures 2.2 and 2.3 show the resolution of the SLD which consists of three wedge-shaped "pixels" of field of view, 0.31° in the vertical direction, and approximately 41° wide.

At the focal line (which is horizontal, and is 169 cm from the middle of

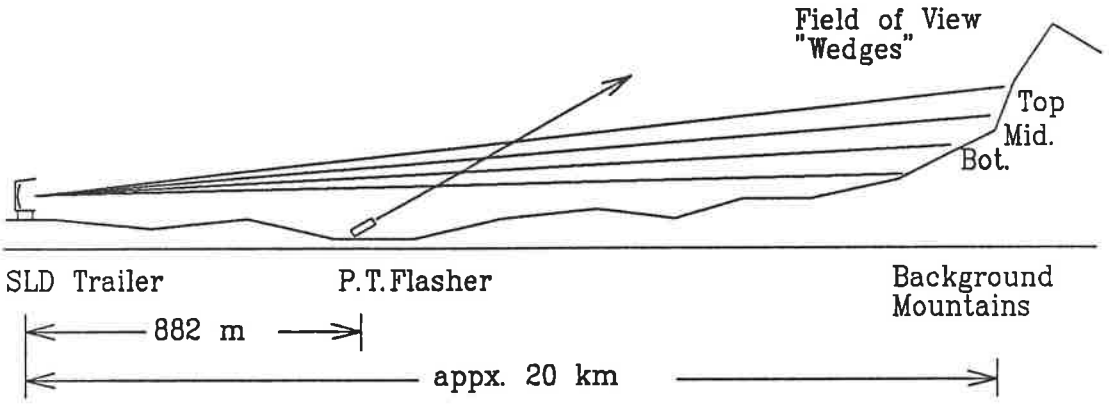

Figure 2.2: Side view of the SLD's fields of view. (Not drawn to scale.) Also shown is the PT emitting a flash of light.

the mirror) are 6 long acrylic plastic rods 1 cm high by 3 cm wide by 163 cm length (see figures 2.4 and 2.5). These rods, which were fabricated by Bicron Corp in Newbury, Ohio, are doped with the waveshifter BBQ at a concentration of 25 mg of waveshifter per liter of acrylic. The waveshifter absorbs in the ultraviolet from $\lambda < 3000$ Å to 4400 Å [18], [19]. However, the mirror's aluminum coating's reflectivity is expected to fall below 50% at a wavelength shorter than 2400Å. For each UV photon the waveshifter absorbs, a photon is re-emitted in the green wavelength range of 4500 Å to 5500 Å. The re-emitted light propagates down the rods, acting as light pipes, to the PMTs at the end where it is converted into an electrical signal. There are losses in this process, of course, which are discussed in section 3.3.3.

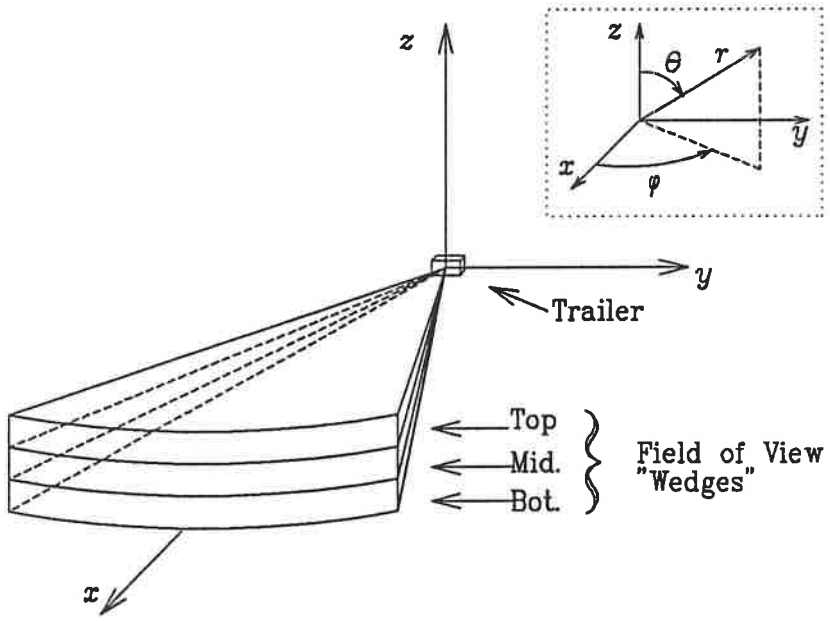

Figure 2.3: Perspective view of the SLD's fields of view. (Not drawn to scale.) Each "wedge" is seen by two BBQ–PMT detector assemblies. Inset shows coordinate system used in simulations and data analysis.

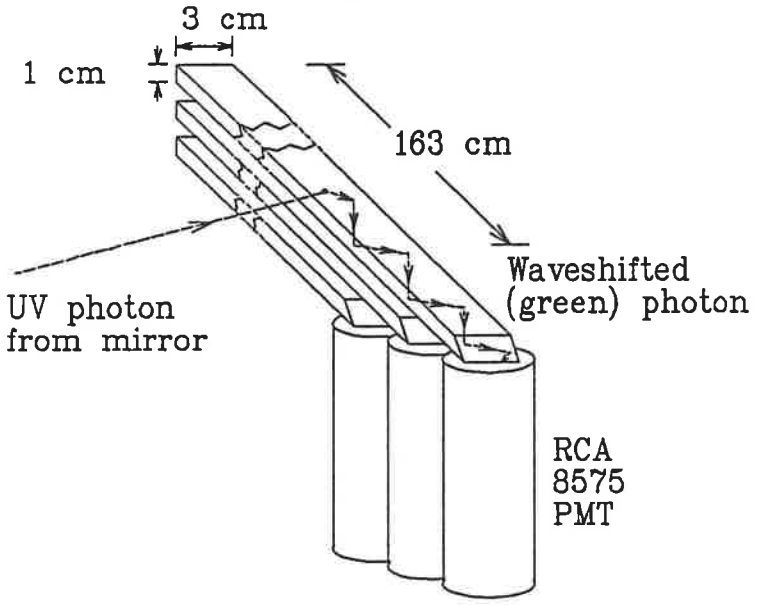

Figure 2.4: Perspective view of the waveshifter rods showing UV light reflected off the mirrors entering the rods. The light is absorbed and re-emitted in the green, whereupon it travels to the PMTs at the end, is detected and converted to an electrical signal. (Only half of the BBQ–PMT assemblies are shown; see next figure.)

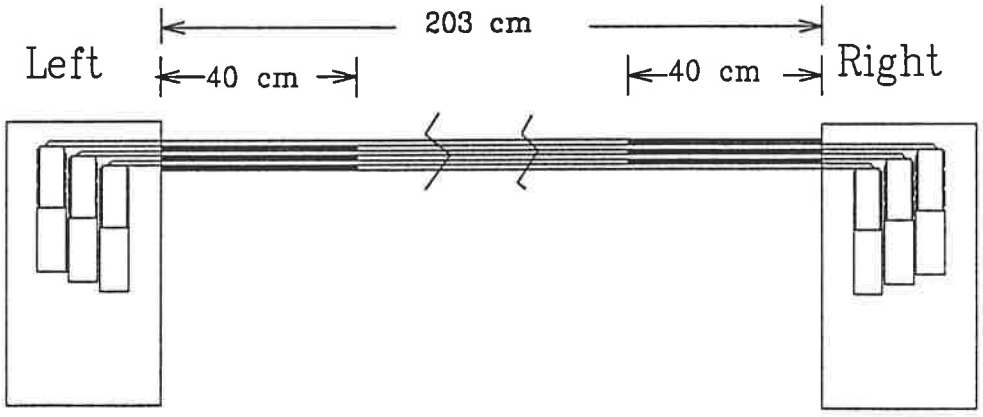

Figure 2.5: Front view of the waveshifter rods showing the interleaving of the left and right BBQ–PMT assemblies. Note the 40 cm regions where there are gaps in the sensitive area.

2.2 Site Layout

The SLD is housed in a trailer which is 21 feet long by 8 feet wide by 9 feet tall, not counting the extra height of the wheels. The trailer was originally a cotton picking wagon. We cut off the steel cage from the top and built a plywood shed on the bed of the trailer. It is located at 20,000 South Nogales Highway, Sahuarita Arizona, about 25 miles south of Tucson, at an altitude of 912 meters (2992 feet). Its coordinates are 31°52'30" North, 110°55'40" West. The Santa Rita ranch is lending us the land the trailer is on, which is on the western edge of the Santa Rita Experimental Range.

Two doors on the side of the trailer open to allow the mirrors to view the atmosphere between the SLD and the Santa Rita mountains whose peaks, Mount Wrightson and Mount Hopkins, are 22 km to the south-southeast. The profile of the mountains is such that the straight-line distance from the SLD to the mountain side varies from 17 km to 21 km depending on the direction within the SLD field of view.

Figure 2.6 shows the site as seen from above. At the top is the SLD trailer with doors open. Also shown is the array of three plastic scintillators that were installed for the atmospheric electric detection of cosmic rays experiment [20]. These scintillators, plus two scintillators inside the trailer itself, above the waveshifter PMT assemblies gave information on cosmic ray cascades that landed close to the trailer and could trigger the system in unusual ways. Each scintillator has an area of 97 cm by 15 cm and a thickness of 5 cm and has an RCA 8575 PMT.

While taking data, the doors were opened at right angles to the length of the trailer to restrict the horizontal (left-right) field of view. This was done to reduce the background light reaching the PMTs as there were strong sources of light pollution in the left and right directions: the cities of Tucson and Nogales.

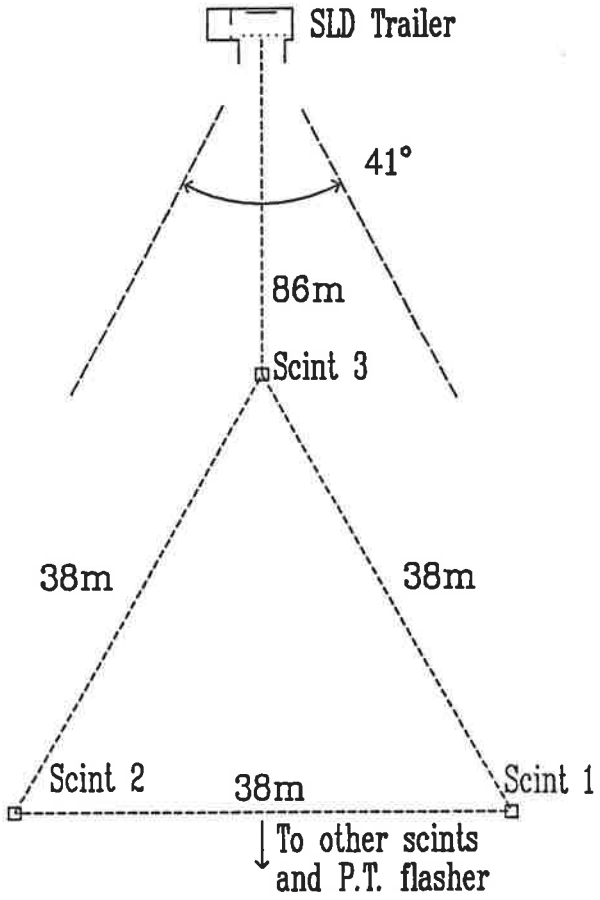

Figure 2.6: View of the SLD looking down.

The disadvantage of keeping the doors in this position is that they partially blocked the field of view of the mirror-detector system for half-angles greater than 12.8°. At 28.3° the view was completely blocked. At a half-angle of 20.5°, the SLD light collecting area was down by 50% so we shall use $2 \times 20.5° = 41°$ as the effective width of the SLD's field of view, but we will have to take into account the obstruction of light in later analysis.

An additional array of three scintillators of the same type was installed 1 km from the SLD, in the middle of the field of view as shown in figure 2.7. These allowed showers which landed far from the trailer to be detected independently by air fluorescence and by the scintillator array.

Also 1 km from the trailer was a test flash lamp which was at the bottom of a long tube that collimated the light. The xenon flash made a diffuse beam of white light which propagated upward and away from the SLD trailer as shown in figure 2.2. The tube was usually at an angle of 60 degrees from the zenith. This light was rich in ultra violet and underwent Rayleigh (molecular) scattering and Mie scattering off of dust particles in the air. From the point of view of the SLD, the scattered light appeared as a spot of light moving upward, much as a cosmic ray cascade would appear as a spot of light, but moving downward. This test flasher, which we nicknamed the "Photon Torpedo" and will henceforth be called the PT, played a crucial role in the setup and debugging of the SLD.

2.3 Electronics

Once the light signal from cosmic rays had entered the six photomultiplier tubes and had been converted into an electrical signal it was first integrated and then amplified and sent to various recording devices which were connected to an IBM XT via a Camac crate and a DSP Technology model 6001 Camac controller. Integration at the PMT anodes converted sharp pulses into step functions with a

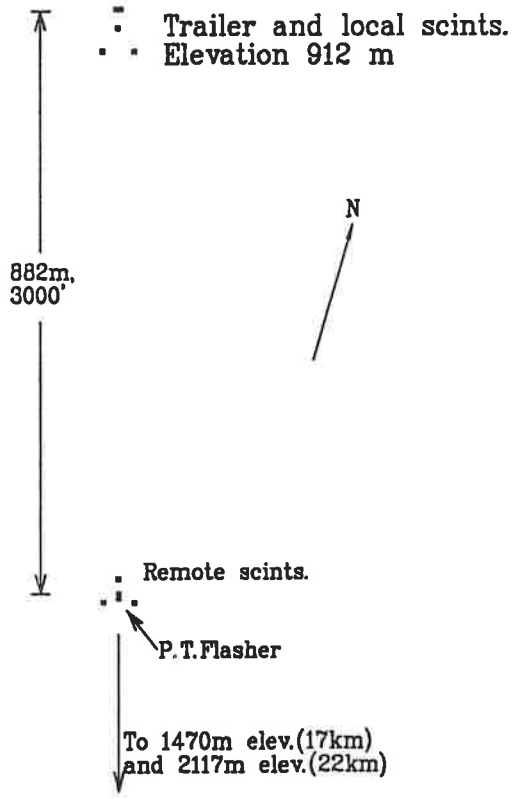

Figure 2.7: View of the SLD looking down but drawn on a smaller scale.

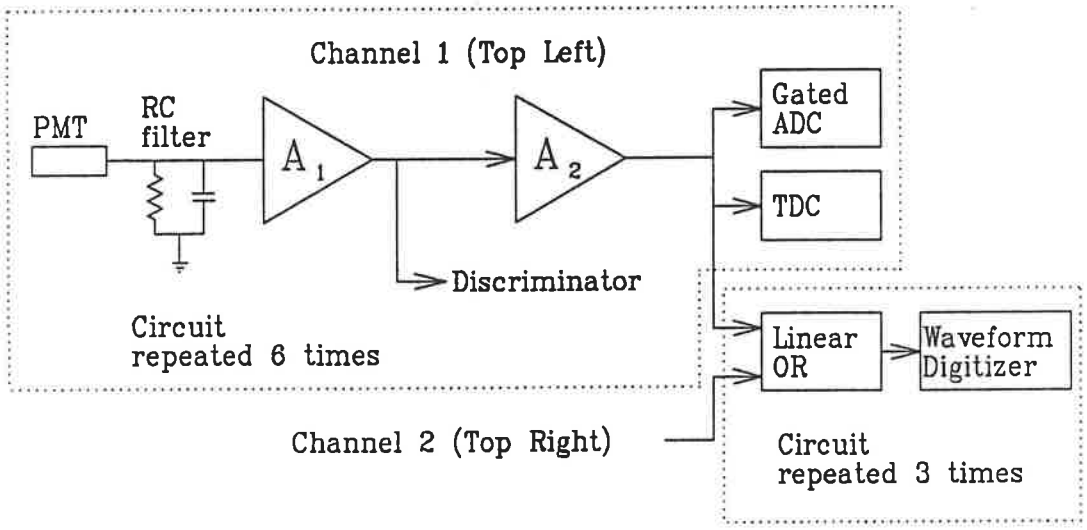

Figure 2.8: Simplified diagram of the data acquisition electronics.

decaying tail. This improved the signal-to-noise ratio and reduced the rate at which false triggers occurred as will be explained in appendix B.1. Figure 2.8 is a simplified diagram of the data acquisition setup. The integrated pulses were amplified and routed to various modules, the function of which will be discussed below.

First in the circuit were six discriminator modules[1] that detected whether the integrated pulse heights from the PMTs exceeded a preset value. As shown in figure 2.9, the discriminator outputs were fed to a majority logic unit which would respond when a threshold number (usually 4 out of 6) of the tubes had sufficient output to trigger the discriminators. A "yes" output from the majority logic unit meant that a flash of light had been received by the system and that further action was to be taken.

This "further action" was primarily the recording of the integrated pulse shapes, a job that was done by a LeCroy 2262 waveform digitizer module. The

[1]Unless indicated otherwise, the electronic modules were made by the author. Schematic diagrams are available upon request.

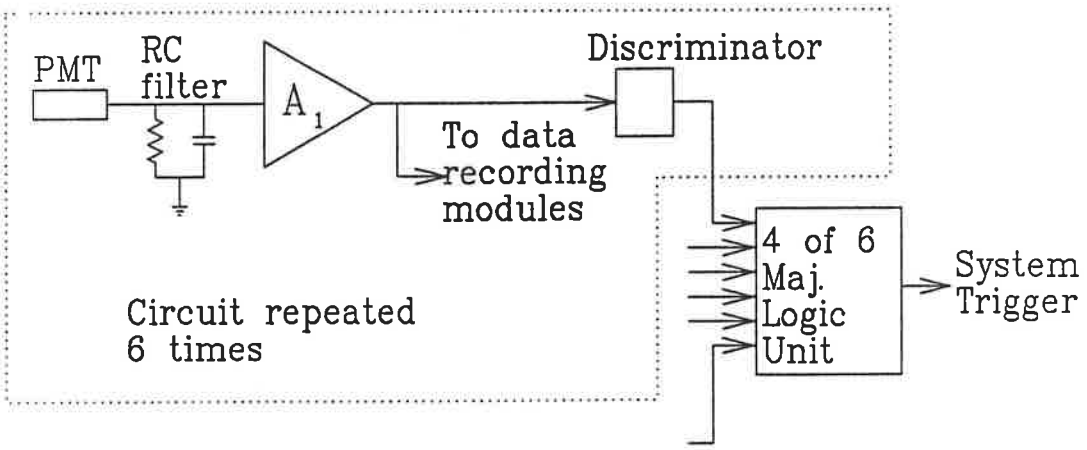

Figure 2.9: Triggering arrangement used in the SLD experiment.

2262 digitizer has 4 inputs, each of which can simultaneously record a signal with a sampling period of 25 ns, a recording time of 7.9 μsec and 10 bit resolution. Since we had six signals, but only 4 digitizer channels, we added the signal from PMT 1 with that of PMT 2, 3 with 4 and 5 with 6. This resulted in 3 signals which were digitized. The 4th digitizer channel was used for various trouble shooting purposes and later became useful for recording electrical transients that had a tendency to accidentally trigger the discriminators.

Another action taken upon triggering was the recording of the size of the pulse. This was done by a DSP Technology 7004 gated integrator. While it is true that the size of the pulses was recorded by the LeCroy 2262 module, the data would only be available after some time consuming calculation by the computer system. This data was needed quickly because the noise in the PMTs and electronics would sometimes falsely trigger the discriminators. Using the pulse integrals, the computer could decide which events were likely to be "real" and could throw out the rest, thus saving disk space and aiding subsequent data analysis. Another benefit is that we had independent pulse size information which in some cases showed strong left-right asymmetries, and this told us that the cosmic ray event was on the extreme left or right side of the field of view.

Also recorded were: (1) A record of which discriminators triggered and when, relative to the time the majority logic unit triggered. This helped in trouble shooting the system and provided information redundant with the digitizer data. (2) The rate at which the discriminators triggered between events. This helped spot malfunctions such as oscillating amplifiers and excessive background light, such as that due to automobile headlights in the field of view. (3) The current of the PMTs. This told us the background light level and helped determine the gain of the tubes. (4) The high voltage on the PMTs. Needed to make sure the power supply was behaving and to monitor the PMT gain. (5) Weather data including temperature, humidity, wind speed and direction. This data was crucial for the atmospheric electricity experiment, but it was also helpful in tracking down the cause of certain strange events which were apparently caused by wind creating static electric sparks which looked like Cherenkov light. (6) Universal time of each event. This was so that if an unusual event such as the 1987 supernova occurred where the absolute time of each event was important this data would be available. Our clock was synchronized by short-wave radio to the NBS station WWV in Colorado which maintains an atomic clock. (7) Yes or no information on whether the near or far scintillator arrays triggered. (8) The time the system was ready for a trigger was recorded. This is called the "live" time, and was about 1% less than the running time.

In addition to the "normal" mode of triggering due to flashes of light in the field of view, the system also triggered when the following conditions were met: (1) If the remote scintillator array triggered and the pulse heights from two out of three of those scintillators exceeded a preset value. (2) If a certain amount of time elapsed (typically 20 minutes) the computer would trigger the system to record background levels and weather data. (3) If a certain amount of time elapsed (also typically 20 minutes), the computer would trigger the system and fire the PT flasher.

As a safety feature, the DC current from the PMT anodes was monitored

by an analog circuit and if any tube exceeded 25 μA, the high voltage was immediately turned off and an alarm sounded. This feature certainly prevented the destruction of the PMTs several times.

2.4 Software

The IBM XT computer system was programmed to run the experiment in two modes: setup and data acquisition. In the setup mode, the system continually monitored and displayed the discriminator trigger rates, high voltage, PMT currents and weather data. This usage of this mode will be described in the next section.

In the data acquisition mode, the computer waited until a trigger arrived from one of the sources described in the previous section. Upon triggering, the computer disabled all the discriminators and logic units to "freeze" the electronics until the data could be transferred to the computer's 10 megabyte disk drive. This prevented a second event from arriving just after the first and confusing the data. Actually, the computer could not respond quickly enough to completely eliminate this problem, so after every possible event, a timer circuit "froze" the electronics for half a second while the computer decided whether the event was worth keeping or should be ignored. The criteria of whether an event should be kept were as follows: If the event was a flash in the field of view, the event was kept if (a) the amplitude of the signal was greater than a threshold value on 4 of 6 PMTs or (b) if the remote or local scintillator array was triggered. If the event was a trigger from either the local or remote scintillator arrays, then the event was kept if the scintillator pulse heights exceeded a threshold on 2 of 3 scintillators, or if a flash of light was seen in the field of view. Finally, the event was kept if it was a computer initiated trigger for system testing and calibration.

Each trigger from the PMTs or scintillators could be analyzed in less than

half a second to the point where the computer could decide whether to keep it. If the data was to be kept, it then took about 3 seconds to record it on disk. If a graphics display was required (because the operator was present and interested in seeing the data immediately) then another 8 seconds was required. Most of the time, the graphics display was not needed, so the dead time was minimal.

All of the data mentioned above was recorded on the disk system. In addition, the program could record comments typed in by the person monitoring the experiment. This allowed notes to be permanently associated with each data run and reduced the need for cumbersome laboratory notebooks in the field.

2.5 Setup and Calibration

Each night of data taking went as follows, barring equipment malfunctions: With the doors closed, the detector room was darkened and equipment, including the high voltages was turned on and allowed to warm up at least 10 minutes. The computer's data taking software was started and put into the setup mode.

Then a small incandescent lamp in a light-tight box with an Oriel $\lambda = 4000$ Å, $d\lambda = 100$ Å interference filter as a window was turned on. This shone UV light evenly on the six BBQ doped light pipes and caused a current in the PMTs. The brightness of the lamp was carefully adjusted to be the same for every run and was chosen to roughly equal the brightness of background light during actual data taking.

Because of the large temperature variations in the SLD experiment (typically 20° C in 24 hours) the PMT high voltage settings would have to be re-adjusted before each run. We were told by the Fly's Eye group and verified for ourselves that the background count rates on the individual discriminators were extremely sensitive to the high voltage settings. For example, we found that at 2000 Volts, a 140 Volt increase would double the tube gain, but cause a 10-fold rate increase. So

by adjusting the HV pots until a given count rate was registered by the computer on each discriminator we were able to set up the SLD consistently before each run.

2.6 Operation

Once the HV on the PMTs had been set, the test lamp was turned off and the doors were opened. The computer software was put in the data acquisition mode. After that there was not much to do other than type in miscellaneous information (which became comments in the data) and to watch for equipment malfunctions.

The most common problem was broken or shorted cables caused by the local rodent population. Another common event was current overload of the PMTs due to cars descending the Madera Canyon road. The best running times tended to be from midnight to 4:30 AM. Data could not be taken before 9 PM because of bright lights nearby.

The final duty of the operator was to shut down the system and close the doors before sunrise. Closing the doors was very important since the 64 square feet of mirror made an excellent solar furnace that quickly scorched cables and melted the plastic handles of misplaced tools.

Chapter 3

The Expected Signal

Before designing the electronics of the SLD system, it was necessary to know what type of signals the electronics would be processing. One needed to know the pulse shape, amplitude and timing of pulses from each of the three field-of-view wedges as well as the nature and magnitude of noise processes that would interfere with the data acquisition process. In the next section, we will consider the evolution of the cosmic ray cascades as they pass through the fields of view. Next we will compute the resulting pulse shapes. Finally, system noise will be considered. The interaction of noise and signal will be of greatest concern in trying to identify cosmic ray events and will be discussed in the next chapter.

3.1 Cosmic Ray Cascade Development

As was explained in section 1.1.3, a cosmic ray shower begins when a high energy particle (proton, alpha particle) strikes the upper atmosphere. Secondary particles are produced, these producing more particles, and so on for many generations of particles. This process continues until the total available energy has been distributed among so many particles that each particle has only enough energy to ionize or excite air molecules before coming to rest.

This process of cascade development has been extensively studied and modeled in Monte-Carlo simulations, but the simple empirical formulas of Greisen[21] are still valid. These will be used throughout this chapter.

Let us begin with the following definitions: [1]

N = no. of particles in the cascade at atmospheric depth X (mostly e^+ and e^- particles)

E_0 = primary energy (eV)

ϵ_0 = critical energy = 84.2 MeV

r_l = radiation length = path length for one electron to lose energy ϵ_0

= 37.3 g/cm^2 for air

X = thickness of material traversed by cascade (g/cm)^2

$\beta_0 = \ln \frac{E_0}{\epsilon_0}$

We now compute the so-called shower age:

$$s \approx \frac{3(X/r_l)}{(X/r_l) + 2\beta_0}. \tag{3.1}$$

3.1.1 The Longitudinal Distribution

Given the above definitions, we can write down the number of particles as a function of atmospheric thickness, or depth and primary energy:

$$N(E_0, X) \approx \frac{.31}{\beta_0^{1/2}} e^{(X/r_l)(1-1.5 \ln s)} \tag{3.2}$$

Equation 3.2 is known as the NKG formula for the longitudinal development of a purely electromagnetic cascade; that is, initiated by a e^+, e^- or γ.

We may convert from atmospheric depth to altitude by fitting the "standard atmosphere" [22] to an exponential and integrating the atmospheric density to calculate the total mass above a unit of horizontal surface area. The result of such a calculation gives (see Appendix A.2)

$$X = 1033 e^{-(h/7519)} \text{g/cm}^2, \tag{3.3}$$

where h is the altitude above sea level in meters.

[1] A complete list of the definitions used in this dissertation is in appendix A.1.

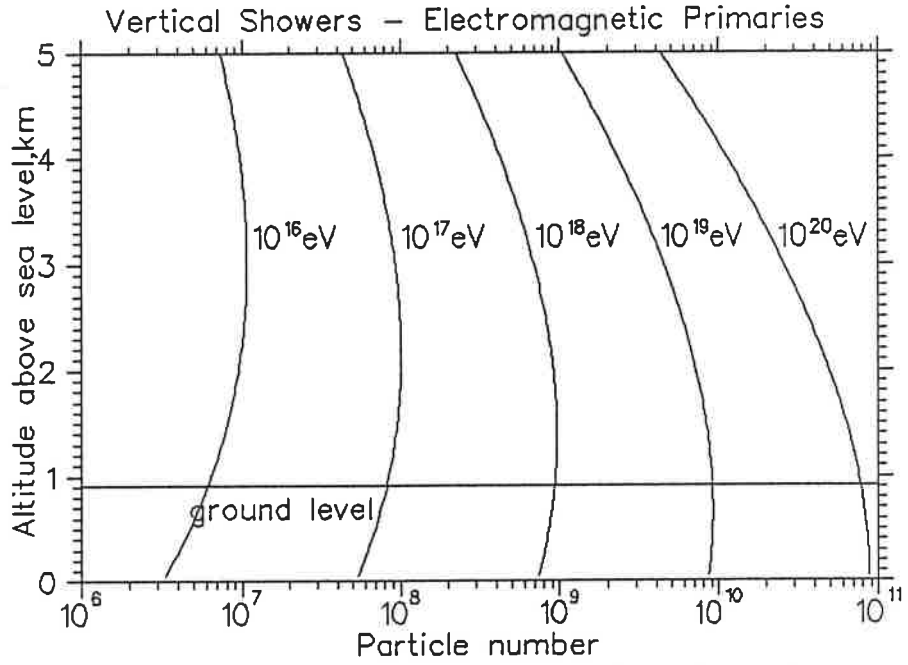

Figure 3.1: Cascade evolution as a function of altitude for various primary energies.

Combining equations 3.2 and 3.3 gives the cascade's number of particles as a function of altitude above sea-level and is plotted for various energies in figure 3.1. It is important to note that at the altitude of the experiment, showers with 10^{19}eV of energy are just reaching the maximum number of particles.

The discussion thus far has assumed that the cascade was purely electromagnetic; however, at the energies the SLD is sensitive to, the primaries are likely to be protons or atomic nuclei which will produce cascades that behave somewhat differently. This is because not all of the energy is put into an electromagnetic cascade in the first interaction.

Instead, the cascade evolution will be dominated by the first primary particle-nucleus interaction after which roughly half of the energy will be available to start showers, and half remain in the form of hadrons that start new showers further down. Thus, a hadron initiated shower will have many overlapping electromagnetic cascades in it as new ones are produced as long as particles in the

shower core have sufficient energy to produces π's. The multiplicity, or number of particles (mainly π's), produced in the first interaction will also influence how quickly the shower develops. This is energy dependent and increases with energy, tending to cause the shower to reach maximum at shallower depths.

Another difference from pure electromagnetic showers will be that the depth at which the first interaction occurs is highly variable since the hadron interaction length for protons in air is 70 g/cm^2. This is the *average* depth of first interaction. The depth of first interaction for a particular event can be much deeper or shallower. For heavier nuclei, the interaction length is shorter; for iron it is 15 g/cm^2. These effects will cause fluctuations in the depth at which showers of a given energy reach their maximum but it also opens the possibility of determining the composition of the primaries if the depth of first interaction can be measured or if enough data is collected to allow statistical analysis.

Sokolsky, in his book [23], offers the following empirical formula to fit the development of hadronic showers seen by the Fly's Eye:

$$N(E_0, X) \approx N_{max} \left(\frac{X - X_0}{X_{max} - X_0} \right)^{(X_{max}-X)/\lambda} e^{(X_{max}-X)/\lambda} \tag{3.4}$$

where X_0 is the depth of the first interaction (which is assumed to be 70 g/cm^2 in later calculations), $\lambda = 70$g/cm^2 and N_{max} is the number of e^+ and e^- particles at the point of maximum development.

$$N_{max} = (1.1 \text{ to } 1.6) E_0(\text{GeV}) \tag{3.5}$$

The coefficient in front of the E_0 is model dependent and was set to the middle of the range for the calculations below.

The depth of maximum development X_{max} is given by the formula

$$X_{max} \approx 0.79 r_1 \beta_0 \tag{3.6}$$

where the factor of 0.79 was chosen to give a good fit to the experimental data in Sokolsky's book.

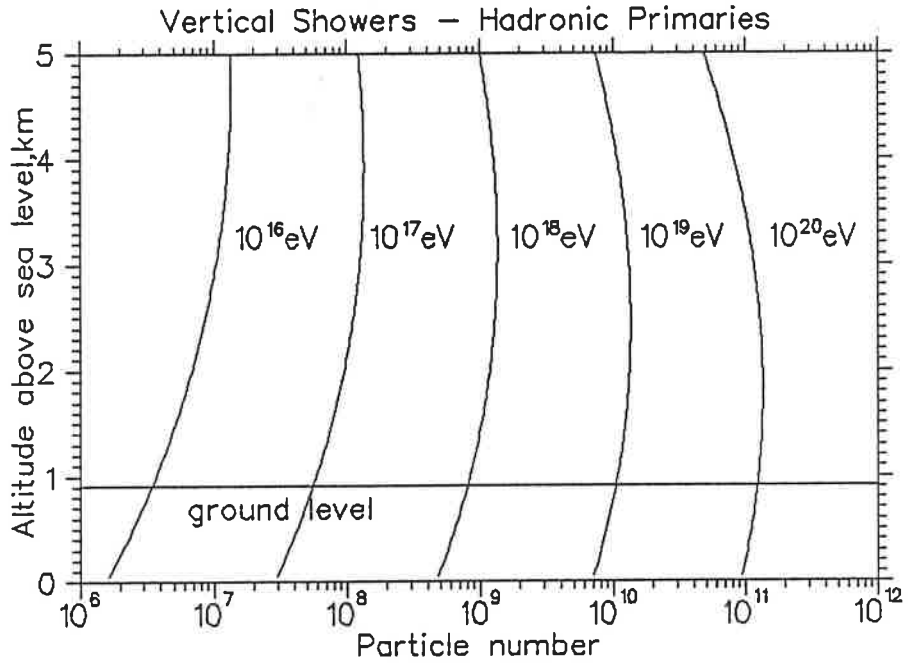

Figure 3.2: Cascade evolution as a function of altitude for various primary energies. Primary particles are assumed to be protons.

$N(E_0, X)$ for hadronic cascades is plotted in figure 3.2

3.1.2 The Lateral Distribution

As the primary cosmic ray is multiplied into numerous secondaries by collisions with air nuclei, the cosmic ray shower begins to grow laterally mainly due to the multiple Coulomb scattering of the electrons ($e^{\pm}$) in their final radiation length of path. Again Greisen's empirical formulas are helpful. Starting with the following definitions:

$$\begin{aligned} E_s &= mc^2(4\pi \cdot 137)^{1/2} = 21.2\text{MeV} \\ r_1 &= E_s/\epsilon_0 = \text{the "scattering" or "Moliere" unit of length} = 9.5\text{g/cm}^2 \text{ in air} \\ x &= \text{distance to core in units of } r_1 \end{aligned} \tag{3.7}$$

E_s is a constant arising in the multiple Coulomb scattering of charged particle. At the altitude of the SLD experiment, $r_1 = 84$ meters.

Greisen introduces an intermediate function $f(x)$ which expresses the density of electrons per unit area of the shower front Δ as follows:

$$\Delta(x) = N\frac{f(x)}{r_1^2} \tag{3.8}$$

where N is the number of electrons at the local depth calculated in equation 3.2. Thus $f(x)$ is a "form function" which describes how the electron density falls off as we move away from the shower core. Note that $\int_0^\infty 2\pi x\Delta(x)dx = N$. Seeking to fit the results of Nishimura and Kamata for the lateral distribution, Greisen offers the following equation for $f(x)$:

$$f(x) = c(s)x^{s-2}(x+1)^{s-4.5} \tag{3.9}$$

where $c(s)$ is a normalization constant with a sliding value:

$$c(s) = \begin{cases} 0.443s^2(1.90-s) & s < 1.6 \\ 0.366s^2(2.07-s)^{5/4} & s < 1.8 \end{cases}$$

For the case of hadronic cascades the lateral distribution will not vary greatly since it will always be dominated by the distributions of the electromagnetic cascades that happen to be peaking at any given point. According to Sokolsky using a shower age s of 1.25 in the lateral distribution formula, equation 3.8, gives good agreement with the Fly's Eye data.

$\Delta(x)$ for proton initiated showers with N_{max} =10^8 ($E_0 \approx 10^{17}$eV) is plotted in figures 3.3 and 3.4 which assume vertical incidence and 30 degrees from vertical, respectively.

3.2 Light Pulse Shape, Amplitude and Timing

The pulses seen by the SLD experiment will have characteristic shapes and widths which are due to the finite speed of the light traveling from the excited air molecules,

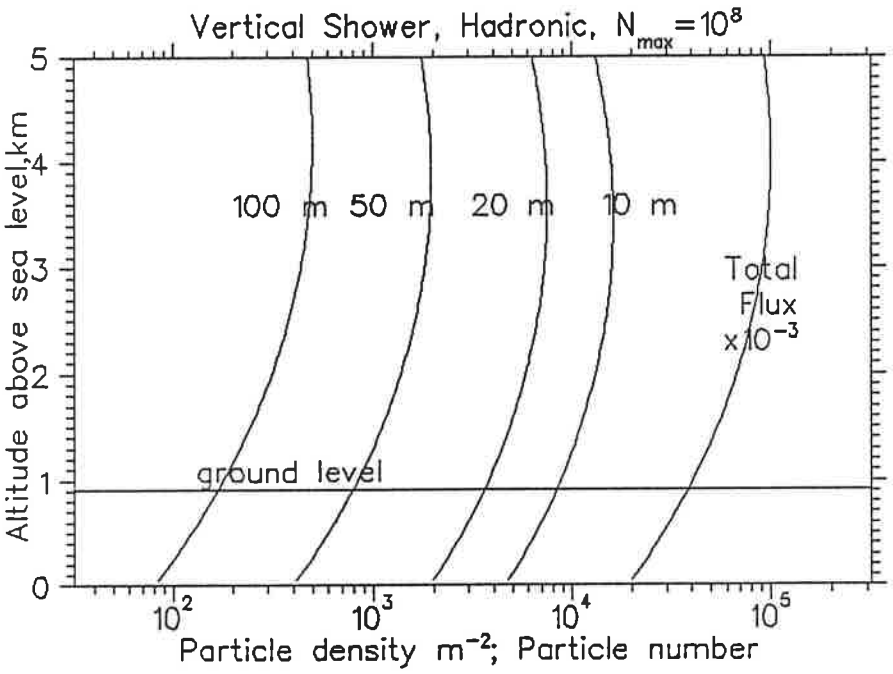

Figure 3.3: Vertical shower, proton initiated, $N_{max} = 10^8$ ($E_0 \approx 10^{17}$ eV); particle density versus altitude at selected distances from the shower core (first four curves). Also shown is the total number of particles (fifth curve).

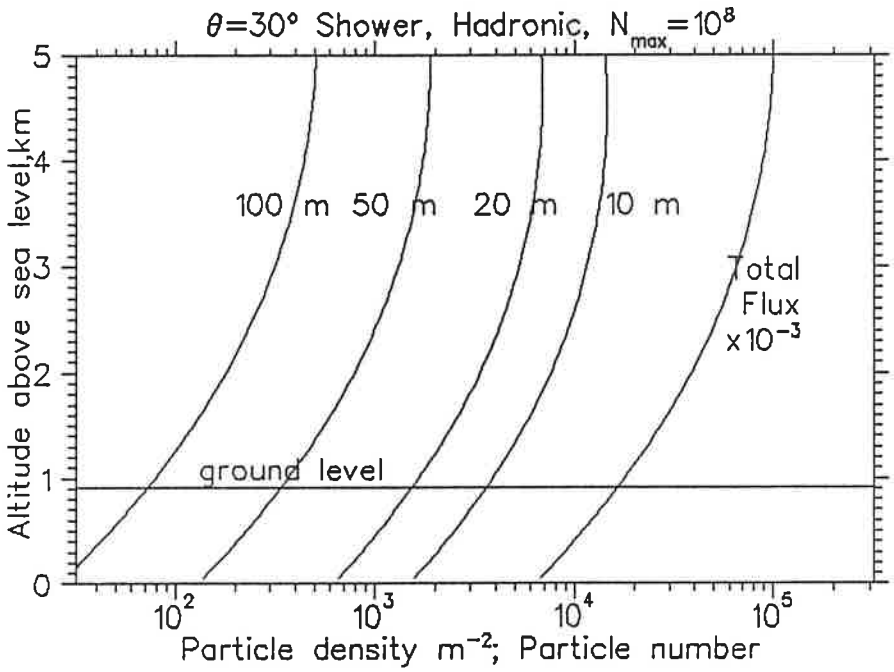

Figure 3.4: Shower slanted 30 degrees from the vertical, proton initiated, $N_{max} = 10^8$ ($E_0 \approx 10^{17}$ eV); particle density versus altitude at selected distances from the shower core (1st four curves). Also shown is the total number of particles (fifth curve).

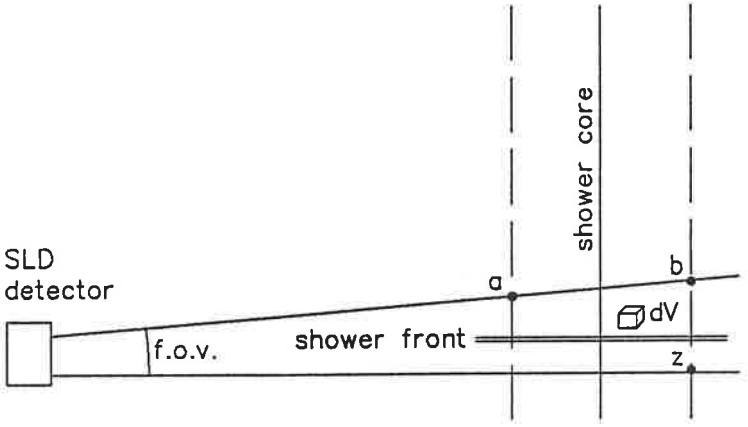

Figure 3.5: Schematic drawing showing a vertical cosmic ray shower passing through the field of view (f.o.v.) of the SLD detector. The region of light production is in the shower front which is traveling downward at the speed of light.

the finite speed of propagation of the cosmic ray cascade and the extent of the cascade in the volume of air that the experiment is observing. The de-excitation time of the air molecules, being less than five nanosecond does not contribute significantly to the signal timing. In this discussion, the speed of propagation of the cascade will be taken to be the speed of light since the particles are highly relativistic for all but final 3 meters of their travel. (The mean range of 1 MeV electrons in air is roughly 0.3 g/cm^{2}or about 2.7 meters at the SLD altitude.)

Figure 3.5 shows schematically a vertical cosmic ray shower propagating downward through the field of view of the SLD experiment. The shower front is the area where ionization of air is occurring and this region is moving downward at the speed of light. The dashed lines represent the lateral extent of the shower which for the purposes of this explanation will be well-defined although in real events, the lateral distribution falls off exponentially.

Referring to figure 3.5, light from points a and b was produced almost

simultaneously. However, because b is farther away from the detector than a, light from b will arrive later. If the shower width w is 50 meters wide, this will account for $wc \approx 150$ nanoseconds of the light pulse's broadening. Light from point z will be produced later than light from point b. If the vertical extent h of the field of view at the shower's distance from the detector happens to be 10 meters, then the pulse will be broadened an additional $hc \approx 30$ nanoseconds.

We can express the above ideas mathematically as follows. Given the following definitions,

$$\begin{aligned}
\vec{r} &= \text{vector pointing to volume element } dV \text{ in the field of view,} \\
t_s(\vec{r}) &= \text{time for shower front to travel from its origin to } dV, \\
\epsilon_p &= \text{no. of photons emitted per electron per unit path length} \\
&\quad \approx 3\text{m}^{-1}, \\
t_t(\vec{r}) &= \text{time for photons to travel from } dV \text{ to the detector,} \\
\Delta(\vec{r}) &= \text{number of particles } (e^+, e^-) \text{ per m}^2 \text{ in the cascade,}
\end{aligned}$$

then the light intensity $I(t)$ (photons/m^2 sec) at the detector can be written

$$I(t) = \frac{1}{4\pi r^2} \int \epsilon_p \Delta(\vec{r}) \delta(t - t_s(\vec{r}) - t_t(\vec{r})) dV \tag{3.10}$$

where the δ is the Dirac delta function.

We will mention for future reference a closely related number, H_p, the time-integrated brightness[2] of an event as observed by the SLD:

$$H_\text{p} \equiv \int_t I(t) dt \qquad \text{(photons per m}^2\text{)}. \tag{3.11}$$

Unfortunately equation 3.10 does not lend itself to straightforward evaluation due to the complicated nature of $\Delta(\vec{r})$. In order to predict the expected pulse shape, a computer program has been written that evaluates equation 3.10, and it has been run for various energies and shower geometries. Results are shown in figures 3.6 through 3.9.

[2]For lack of a better word, I will use the term ***brightness*** to mean time-integrated light intensity.

A few words about these pictures are in order. The top pictures show the density of photon production (photons per m^3). Perspective (A) is that of an observer a short height above the SLD, level with the center of the part of the shower in the field of view. In (B) the observer is to the right of the SLD; the SLD is at the lower left looking to the right and up (vertical scaling is stretched). The lower plots show the number of photons per m^2 per simulation time interval, Δt, arriving at the SLD. The time axes have 100 time intervals of 10 nsec each. Only fluorescent light from the portion of the cascade that is within the SLD's field of view is counted. In plot (D) the individual signals from each of the three field of view wedges are plotted; the top wedge peaks first, then the middle and finally the bottom wedge.

One can see certain trends in the timing: (1) Showers that are further away tend to exhibit longer pulses and have greater time differences between pulses from the three sub-fields of view. (2) Showers that are slanted towards the detector have sharper pulses while showers slanted away are broader.

3.3 Apparent Luminosity of the Cascade

3.3.1 Brightness of Air Fluorescence

The electrons and positrons ionize the air and in particular create N_2^+ ions which emit light at the wavelengths shown in table 3.1. The absolute brightness of the various spectral lines of air fluorescence has been measured by Davidson and O'Neil [24]. These measurements were made with a low energy (50 keV) beam of electrons coming to rest in air. It would be worthwhile to conduct another experiment, with relativistic electrons to verify that these numbers do not change for higher energies since the calibration of this experiment, and that of the Fly's Eye depends on these numbers.

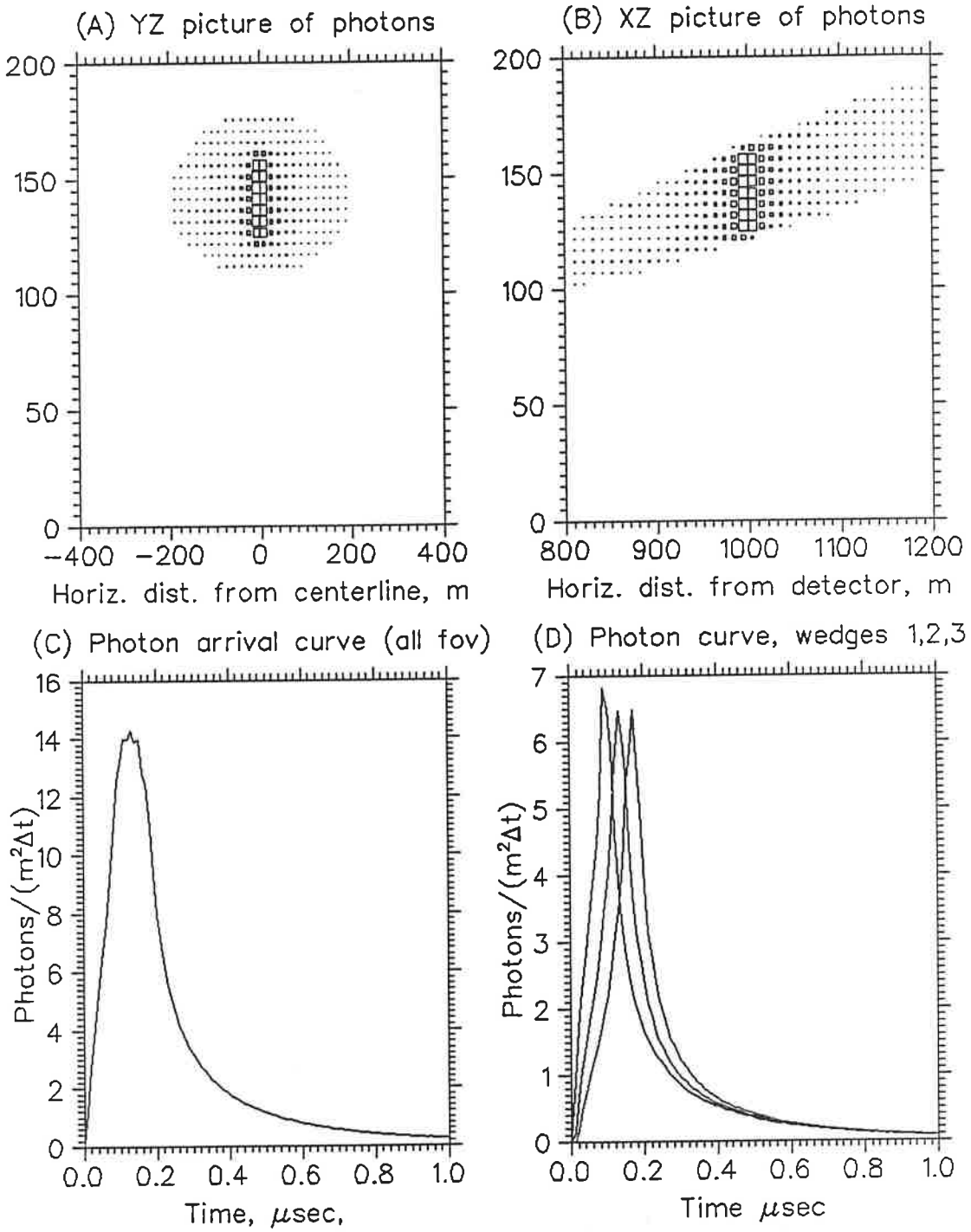

Figure 3.6: Vertical, proton initiated, $N_{max} = 10^8$ shower, 1 km distance, as seen from the detector (a), from the side (b), light pulse for all f.o.v. (c), and for the three f.o.v. wedges (d). (a) and (b) are truncated views limited to areas within the field of view of the SLD.

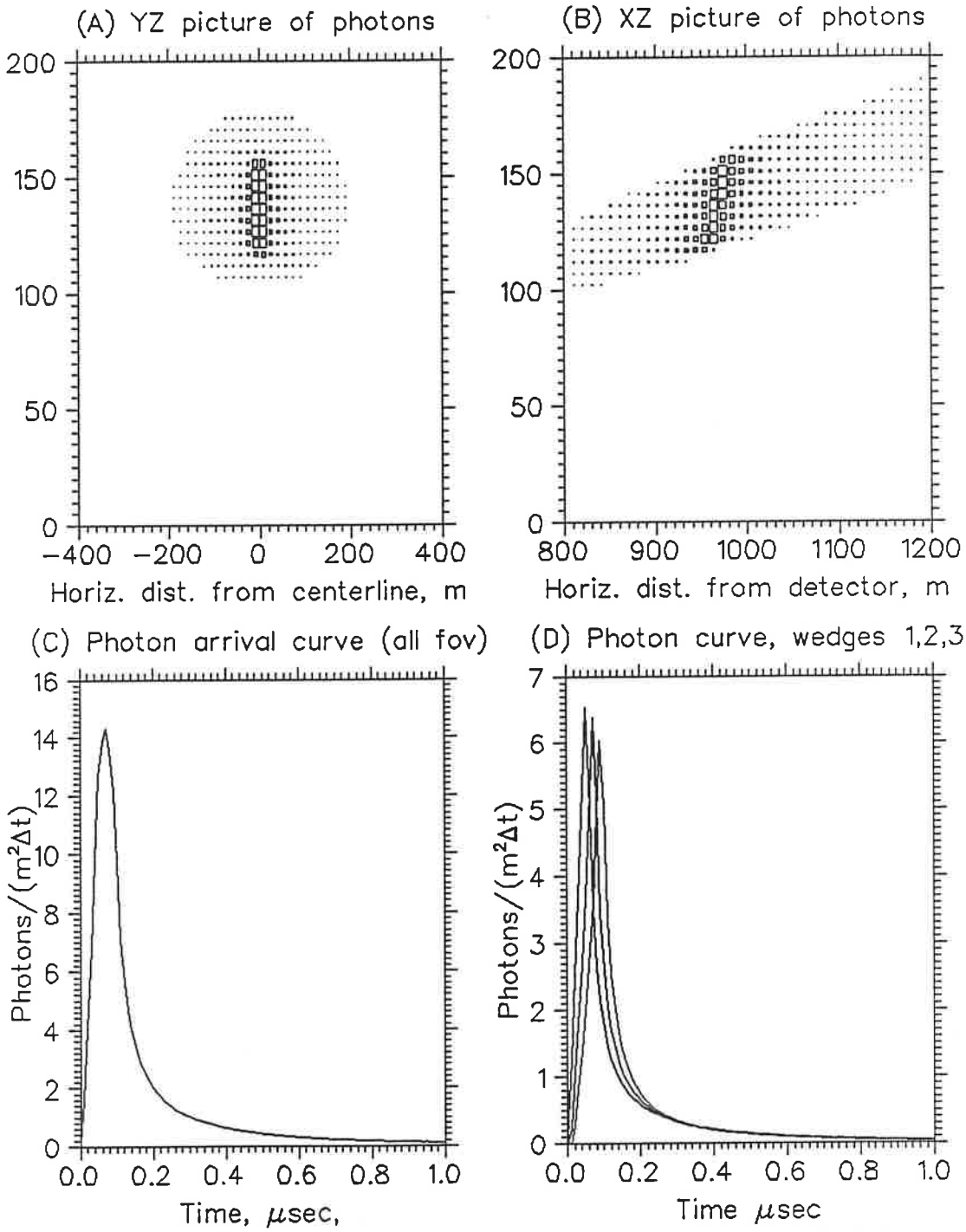

Figure 3.7: $N_{max} = 10^8$ shower, 1 km from the detector, but slanted 30 degrees towards the detector.

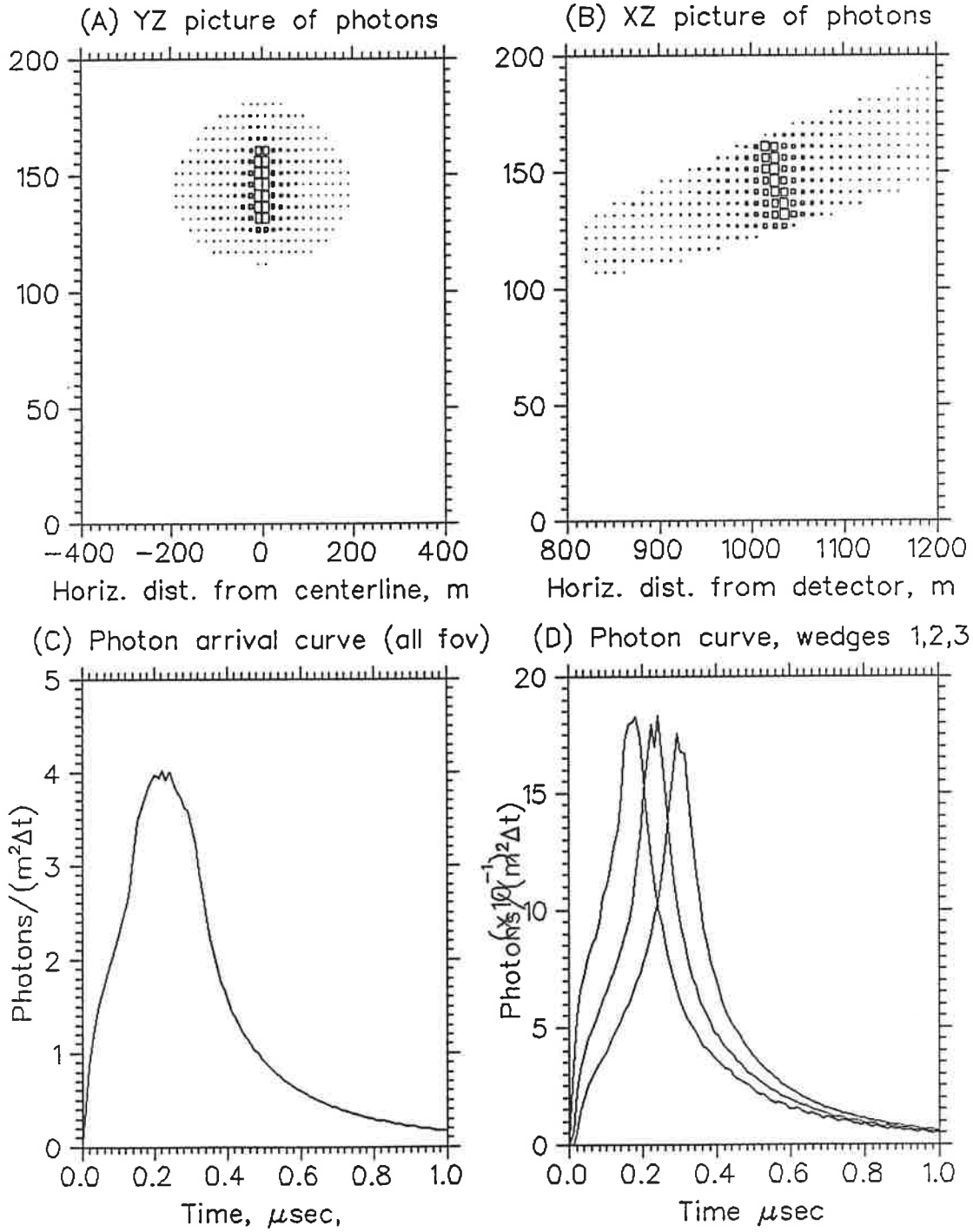

Figure 3.8: $N_{max} = 10^8$ shower, 1 km from the detector, but slanted 30 degrees away from the detector.

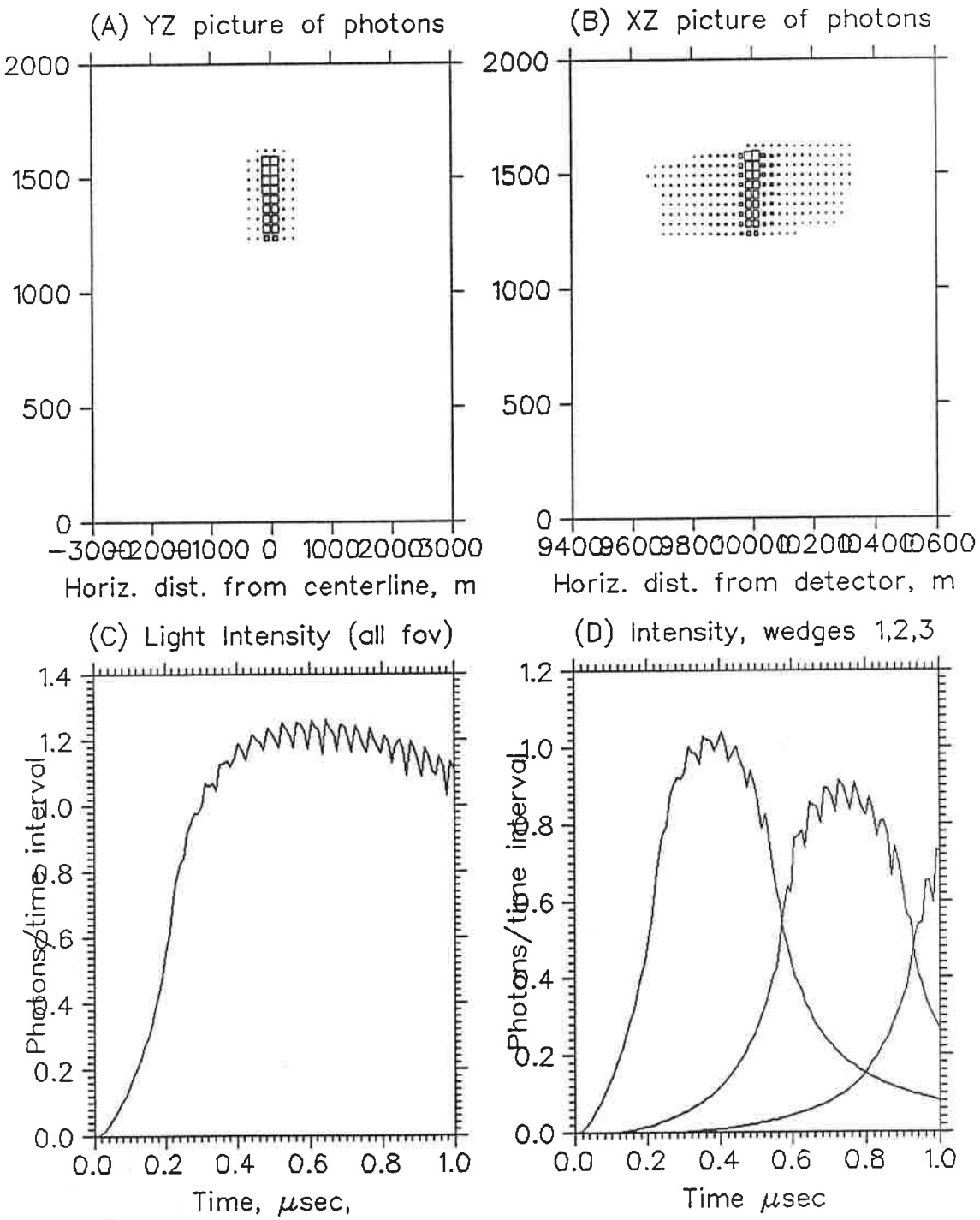

Figure 3.9: Vertical $N_{max} = 10^9$ shower, 10 km from the detector. (Roughness of the timing is due to the simulation step size.)

Since Davidson and O'Neil's data is for a 50 keV electron beam coming to rest in 600 torr air, we must try to convert these numbers into a form applicable to particles that are highly relativistic (i.e. many MeV), and not coming to rest until after many meters of path length. Their data is shown in table 3.1 wherein $\epsilon_{stop}(\lambda)$ is the scintillation efficiency (power out)/(power in) for the stopping electrons.

The energy loss per unit path length $(\frac{dE}{dx})_{600}$ in air at 600 Torr is 0.174 MeV/m. The actual rate of energy loss will increase with pressure, which will tend to increase the energy available to drive the fluorescence process. However, this effect is largely cancelled by the simultaneous increase in the molecular collision rate which will in turn allow a lesser fraction of the available energy to be released in the fluorescence mode rather than as kinetic energy (heat).

The relative dependence of the air fluorescence yield as a function of pressure has been measured by Hartman [25] for each fluorescence band for pressures ranging from 30 to 960 Torr, using a beam of 750 eV electrons coming to a stop in his air sample. This data confirms that the fluorescence yield drops with increasing pressure and while this effect does completely cancel the increase in $\frac{dE}{dx}$ for increasing pressure, the error introduced by ignoring both of the pressure effects while using Davidson's data which was collected at 600 Torr is, at worst, 8% for the pressure at the altitude of the SLD, which is 673 Torr. This is how much we will be underestimating the fluorescence from the 2P nitrogen band which includes the lines at 3371, 3537, 3577, 3756, 3805, 3998 and 4059 Å. The error will be less for the 1N lines at 3914 and 4278 Å. The error is further reduced for distant events since these will be at higher altitudes due to the upward tilt of the SLD's field of view.

Air temperature also has a small effect on the fluorescence efficiency. Over the 40° range of temperature at the SLD site, this will cause variations less than 2% [14].

So ϵ_p, the luminosity per unit length of a minimum ionizing electron or

positron, is given by

$$\begin{aligned} \epsilon_p &= \sum_\lambda \epsilon_p(\lambda) \\ &= \sum_\lambda \epsilon_{\text{stop}}(\lambda) \cdot (\tfrac{dE}{dx})_{600} \cdot \frac{\lambda}{hc} \\ &= 3.2 \text{ photons/meter} \end{aligned} \tag{3.12}$$

The contribution of each wavelength to ϵ_p is shown in the third column of table 3.1.

3.3.2 Attenuation of the Optical Signal

Unfortunately, the air fluorescence light of the cascade is scattered by aerosols in the air (Mie scattering) and by the air molecules themselves (Rayleigh scattering). The aerosol scattering is the dominant loss, and is quite variable. The scattering coefficient, $\alpha(\lambda)$ (km^{-1}), which combines both Mie and Rayleigh effects, is a strong function of wavelength. $\alpha(\lambda)$ increases sharply at shorter wavelengths and is listed in the fourth column of table 3.1. (The method used for determining practical values of $\alpha(\lambda)$ is discussed in Appendix A.3.) Thus, the effective luminosity of a shower will depend on its distance since the fluorescent emission lines will or will not be greatly obscured depending on the wavelength. It is practical to think in terms of the effective efficiency (photons per meter), but modified to take the distance into account:

$$\epsilon_p(r) = \sum_\lambda \epsilon_p(\lambda) \cdot e^{-\alpha(\lambda) r} \tag{3.13}$$

For selected distances, $\epsilon_p(r)$ is shown in the bottom row of table 3.1. Calculated values for $\alpha(\lambda)$ using a typical visibility of 80 km (50 miles), as discussed in Appendix A.3, were used as a reasonable approximation to the scattering at the SLD site.

Table 3.1: Scintillation efficiencies, $\epsilon_p(\lambda)$ of various air fluorescence lines and atmospheric attenuation lengths $\alpha(\lambda)$ at corresponding wavelengths. Also shown are effective efficiencies after scattering losses for distances of 1, 5, 10 and 20 km, assuming 80 km visibility.

λ Å	ϵ_{stop}	$\epsilon_p(\lambda)$ m^{-1}	$\alpha(\lambda)$ km^{-1}	ϵ_p(1 km)	ϵ_p(5 km)	ϵ_p(10 km)	ϵ_p(20 km)
3371	2.1×10^{-5}	1.0	0.16	8.7×10^{-1}	4.5×10^{-1}	2.0×10^{-1}	3.9×10^{-2}
3537	3.2×10^{-6}	.16	0.14	1.4×10^{-1}	8.0×10^{-2}	3.9×10^{-2}	9.4×10^{-3}
3577	1.5×10^{-5}	.78	0.14	6.8×10^{-1}	3.9×10^{-1}	1.9×10^{-1}	4.8×10^{-2}
3756	3.0×10^{-6}	.16	0.12	1.5×10^{-1}	8.9×10^{-2}	4.8×10^{-2}	1.4×10^{-2}
3805	5.2×10^{-6}	.29	0.12	2.6×10^{-1}	1.6×10^{-1}	8.8×10^{-2}	2.7×10^{-2}
3914	7.0×10^{-6}	.40	0.11	3.6×10^{-1}	2.3×10^{-1}	1.3×10^{-1}	4.5×10^{-2}
3998	1.8×10^{-6}	.10	0.10	9.4×10^{-2}	6.2×10^{-2}	3.7×10^{-2}	1.3×10^{-2}
4059	1.8×10^{-6}	.11	0.10	9.6×10^{-2}	6.5×10^{-2}	3.9×10^{-2}	1.5×10^{-2}
4278	2.7×10^{-6}	.17	0.09	1.6×10^{-1}	1.1×10^{-1}	7.2×10^{-2}	3.0×10^{-2}
Total:		3.2		2.8	1.6	0.85	0.24

3.3.3 Light Received by SLD, Electronics Response

In order to design and evaluate the SLD, we had to consider how the system would respond to a signal of brightness H_p(see equation 3.11) photons per m^2.

The number of photoelectrons emitted by the cathode of one the PMTs will be

$$N_{pe} = H_p A_{eff} = H_p A_{mirror} E_{mirror} E_{BBQ} F_{BBQ} E_{PMT} \tag{3.14}$$

where we have introduced A_{eff} to mean the effective area of the mirror–light pipe–PMT system after including the following area and efficiencies:

$A_{mirror} = 4.7 m^2$ area of mirror, taking into account obstructions and masked-off areas

$E_{mirror} \approx 0.9$ reflectance of the mirrors in the 3000–4500 Å range

$E_{BBQ} \approx 0.3$ efficiency of the BBQ light pipe of coupling light from the mirror to the PMT

$F_{BBQ} \approx 0.8$	fraction of focal region actually filled with BBQ rods (see figure 2.5)
$E_{PMT} \approx 0.2$	quantum efficiency of the PMT at the shifted wavelength (5000 Å)
$A_{eff} \approx 0.20 m^2$	product of the above.

For a fast event (optical pulse width $\ll \tau$, the integration time constant at the PMT anode), the size of the pulse at the PMT anode will be determined by G, the PMT gain, and C, the anode and emitter follower capacitance:

$$V = \frac{Q}{C} \tag{3.15}$$

$$= \frac{H_p A_{eff} G e}{C} \text{ Volts} \tag{3.16}$$

For a treatment of what happens to pulses of finite width, see section B.1 and also section 4.2.1.

In the actual SLD the values of R_{back}, G, R and C varied as we tried different configurations but the final values were:

$$I_{back} = 1.1\ \mu A \tag{3.17}$$

$$G = 1.1 \times 10^5$$

$$R = 500 \text{ ohms}$$

$$\tau = 0.3\ \mu sec$$

$$C = \frac{\tau}{R}$$

$$= 600 \text{ pico farads}$$

Using these numbers we can calculate the SLD sensitivities S_Q and S_V:

$$S_Q = A_{eff} G e \tag{3.18}$$

$$= 3.5 \times 10^{-15} \text{ Coulombs/(photon m}^2\text{)}$$

$$S_V = \frac{S_Q}{C} \tag{3.19}$$

$$= 5.8 \times 10^{-6} \text{ Volts/(photon m}^2\text{)}$$

3.4 Background Light

Both the Fly's Eye and the SLD experiments observe the light from cascades on clear, moonless nights. Because of the small amount of light available (10^{10} photons is not much, when observed from 15 km away), the light from the stars, planets, aurora and air glow is a serious problem. Since the background light consists of photons arriving at random times, if a given detector receives N_B photons per time interval, the RMS noise will be equivalent to $\sqrt{N_B}$ photons per time interval.

According to measurements made by Broadfoot and Kendall [26] the background intensity, J_0, due to starlight in the 3400 to 4400 Å wavelength range, is about 400 Rayleighs [3]. This is equivalent to $J_0 = 3.2\times10^{11}$ photons/(sec m^{2}sr).

Because the SLD is not looking directly at the sky, but at a distant mountain range, the actual background light, J, will be somewhat less. The ratio J/J_0 is a function of the reflectivity, $r_{\rm fov}$, of the mountain in the field of view and of the amount of air, $X_{\rm fov}$, between the SLD and the mountain. In another paper [27] we have computed the ratio J/J_0 for various conditions and compared results with measurements made at Mount Hopkins. Using results from that paper:

$$\frac{J}{J_0} = \frac{1}{2} + (r_{\rm fov} - \frac{1}{2J_0}) \int_0^\infty e^{-\alpha_X(\lambda) X_{\rm fov}} j(\lambda) E_{\rm detector}(\lambda) d\lambda \qquad (3.20)$$

where $j(\lambda)$ is the background light seen when looking up, $E_{\rm detector}(\lambda)$ is the detector efficiency and $\alpha_X(\lambda)$ is the atmospheric attenuation coefficient in terms of air thickness.

Because we know the attenuation in terms of distance rather than air thickness we will convert using the following expressions:

$$\begin{aligned} \alpha_X(\lambda) &= \frac{\alpha(\lambda)}{\rho} \\ X &= x\rho \end{aligned}$$

[3] The Rayleigh is a unit of photon brightness defined by the relation $B(\text{Rayleigh}) = \frac{4\pi}{10^6} B(\text{photon cm}^{-2}\text{sr}^{-1}\text{s}^{-1})$

$$X\alpha_X(\lambda) \;=\; x\alpha(\lambda)$$

where $x \approx 20$km is the distance to the mountains, $\rho = 1.08\times10^{-3}\mathrm{g/cm^2}$ is the average air density between the SLD and thus $X_{\mathrm{fov}} \approx 2160\mathrm{g/cm^2}$.

Unfortunately equation 3.20 must be evaluated numerically, so we will only quote the result from reference [27]:

$$\frac{J}{J_0} \approx 0.3$$

Thus our estimated background light is

$$J = 0.3 \cdot 3.2\times10^{11} = 9.6\times10^{10}\mathrm{photons/(sec\ m^2 sr)}$$

The background photoelectron rate at the PMTs, R_{back}will be

$$R_{\mathrm{back}} = JA_{\mathrm{eff}}\Omega = JA_{\mathrm{mirror}}E_{\mathrm{mirror}}E_{\mathrm{BBQ}}F_{\mathrm{BBQ}}E_{\mathrm{PMT}}\Omega \tag{3.21}$$

where

$$\begin{aligned}\Omega &= \Delta\theta_{\mathrm{BBQ}}\Delta\phi_{\mathrm{BBQ}}\\ &= (0.31°)(41°)\\ &= 3.9\times10^{-3}\mathrm{sr}\end{aligned}$$

is the field of view of one PMT and the other values were introduced in section 3.3.3.

Evaluating equation 3.21 we find that the rate is $R_{\mathrm{back}} = 7.5\times10^{7}$ per second or 75 photoelectrons per μsec. (Remember that a typical event is expected to be a pulse about 1 μsec wide.)

3.4.1 Actual Background Light

The background current in the photomultiplier tubes, I_{back}, provides a means of checking these numbers. Using values from a typical run:

$$\begin{aligned} I_{\text{back}} &= GeJA_{\text{eff}}\Omega \\ &= (1.1\times10^{5})(1.6\times10^{-19}\text{Coulombs})\cdot \\ &\quad (9.6\times10^{10}\text{photons}/(\text{sec m}^2\text{sr}))(0.2\text{m}^2)(3.9\times10^{-3}\text{sr}) \\ &= 1.3\ \mu\text{A} \end{aligned}$$

The actual tube current in this run was 1.1 μA for the tubes sampling the center of the SLD field of view.

3.4.2 Noise Due to Background Light

The noise of the PMT electrons leaving the photocathode at random times (therefore Poisson noise), is analysed in Appendix B.1. The square of the rms noise measured at the PMT anode is given by equation B.5 which we will use, after making the following substitutions: $n=0$ therefore $D_n=2$, $R_0=R$. So we have

$$(V_{\text{rms,pe}})^2 = I_{\text{back}}\cdot\frac{GeR^2}{2\tau}. \tag{3.22}$$

Using the values for R_{back}, G, R and τ listed in equation 3.17, the actual noise at the anode was:

$$V_{\text{rms,pe}} = 9.0\times10^{-5}\ \text{Volts}$$

3.5 Noise Due to Electronics

In addition to the photoelectron noise, we have noise due to the electronic components. In the SLD electronics (see figure 2.8), the noise came from the emitter followers, the preamps, amplifiers, linear OR modules and the digitizer. The noise of the preamps and amplifiers, referred to the PMT anode was:

$$V_{\text{rms,elec}} = 1.6\times10^{-4}\ \text{Volts}$$

The noise of the linear OR modules and the digitizer was

$$V_{\text{rms,digit}} = 2.3\times10^{-4} \text{ Volts}$$

We must now combine the effects of the noise sources. Because of a limitation in the available data acquisition electronics, we had to combine the signals of the six PMTs in pairwise fashion. PMTs 1 and 2 were combined, 3 and 4, and 5 and 6. The three pairs made 3 wedge-shaped fields of view which have been referred to as the Top, Middle and Bottom wedges and each fed into a waveform digitizer. Therefore, for each wedge, we have twice the noise and signal contribution of a PMT, $V_{\text{rms,pe}}$, and again twice the noise contribution of the PMT preamps and amplifiers. But we have only once the contribution of the digitizer and the linear OR (which sums the left and right signals), $V_{\text{rms,digit}}$. Thus, the total noise is:

$$(V_{\text{rms,total}})^2 = (2V_{\text{rms,pe}})^2 + (2V_{\text{rms,elec}})^2 + (V_{\text{rms,digit}})^2 \tag{3.23}$$

$$V_{\text{rms,total}} = 2.4\times10^{-4} \text{ Volts} \tag{3.24}$$

3.6 Equivalent Light Noise

A useful way of considering the noise is to convert it to a number comparable to H_{p}, the number of photons per m^2 from cosmic ray events. We will call this H_{rms}, the equivalent light noise.

$$H_{\text{rms}} \equiv \frac{V_{\text{rms,total}}}{S_{\text{V}}} \tag{3.25}$$

$$H_{\text{rms,wedge}} = \frac{V_{\text{rms,total}}}{2S_{\text{V}}} = 30 \text{ photons m}^{-2} \tag{3.26}$$

where S_{V} was defined in 3.19. $H_{\text{rms,wedge}}$ is the equivalent light noise for a field of view wedge, and the factor of two is to account for the presence of two PMT signals coherently added by the linear OR modules.

3.7 The Expected Event Rate, Energy Threshold and Effective Area

In this section, we seek to predict how many events will be seen. First we must decide how to distinguish between noise conspiring to look like an event, and real events.

We will use the following idea: If we choose to ignore signals smaller than a certain threshold, we will eliminate all but a few spurious noise events. The rate R_{acc}, of the spurious events is given by equation B.9 which, after solving for P, the probability of a given discriminator firing in time interval τ, appears as follows:

$$P = (\frac{\tau}{F} R_{acc})^{1/F}. \tag{3.27}$$

In this context, $F = 3$ (3-fold coincidence), $\tau = 10^{-7}$ seconds (the time scale of meaningful details in the signal – compare with figures 3.6 through 3.9), and R_{acc} is the accidental rate at which we are willing to be "fooled" by the noise. We will pick $(R_{acc})^{-1}$=50 hours = 3.6×10^5 seconds.[4] Using these numbers:

$$\begin{aligned} P &= \left\{ \frac{10^{-7}}{3} (3.6\times10^5)^{-1} \right\}^{1/3} \\ &= 4.5 \times 10^{-5} \end{aligned}$$

Consulting a table of integrals of the Gaussian distribution, we find that this value of P implies setting our threshold for ignoring noise to 4 standard deviations:

$$\begin{aligned} H_{\text{thresh}} &= 4 H_{\text{rms,wedge}} \\ &= 120 \text{ photons m}^{-2} \end{aligned} \tag{3.28}$$

Given this threshold and using the results of the preceeding sections, we can compute the expected performance of the SLD system. Results are tabulated in table 3.2.

[4] We are making the additional simplification that the SLD system will capture a predictable fraction of the real signal.

Table 3.2: Distance from SLD, effective area and primary threshold energy for that distance, rate for events of that energy and higher.
Last column shows accumulated rates for progressively larger distances, assuming 80 km visibility and an acceptance angle Ω=1 sr. Note the area less than 1 km from the SLD has been excluded from these calculations.

Distance km	Threshold eV	Area km^2	Rate hour^{-1}	Total Rate hour^{-1}
1	1.2×10^{17}	0.0	0.000	0.000
2	2.4×10^{17}	1.1	0.171	0.293
3	3.5×10^{17}	2.9	0.219	0.478
4	5.1×10^{17}	5.4	0.194	0.603
5	6.8×10^{17}	8.6	0.174	0.691
6	9.1×10^{17}	12.5	0.139	0.755
7	1.1×10^{18}	17.2	0.125	0.799
8	1.3×10^{18}	22.5	0.107	0.831
9	1.6×10^{18}	28.6	0.088	0.853
10	2.0×10^{18}	35.4	0.071	0.870
11	2.4×10^{18}	42.9	0.056	0.881
12	2.9×10^{18}	51.2	0.044	0.890
13	3.5×10^{18}	60.1	0.034	0.897
14	3.8×10^{18}	69.8	0.032	0.902
15	4.6×10^{18}	80.1	0.024	0.905
16	5.6×10^{18}	91.2	0.018	0.908
17	6.1×10^{18}	103.0	0.017	0.910
18	7.4×10^{18}	115.6	0.013	0.912
19	8.1×10^{18}	128.8	0.012	0.913
20	9.9×10^{18}	142.8	0.009	0.914

Expected trigger rate = 0.9 events per hour.

As can be seen from the table, we can expect on the order of 1 event per hour. Most of the events will be close to the SLD, $r < 6$ km, and with primary energy $E_0 \approx 10^{17}$ eV.

At lower energies, the shower must be close to the SLD in order to be bright enough, but for $E_0 > 10^{19}$ eV, the effective area is very large, about 140 km^2. If we could run for 23 nights, averaging 5 hours of live-time per night, we would expect to see energies in excess of 10^{19} eV.

Chapter 4

Events Seen by the Side Looking Detector

The bulk of the infomation coming from the SLD is the data collected by the LeCroy 2262 high speed digitizer. From the digitizer data, we can estimate the distance and energy of cosmic rays events. The following sections show typical events from the SLD.

The SLD system took data for 39 nights over a period of two years accumulating 110 hours of live-time. Most of the data was useful only in the sense that it guided us towards fixing problems and gradually refining our technique. While we had seen many events of the type described below as "Cherenkov" events, we did not see air fluorescence events until the very end. We had, in fact, almost given up hope when the positive results appeared. The difference was a fortuitous combination of cold weather and clear skies, equipment that was fully functional and long moonless winter nights.

In a period of 8 1/2 hours over two nights, we recorded 7 events with the correct "signature" for a large, distant extensive air shower, as seen by air fluorescence. An 8th event was seen by the remote scintillator array and possibly by the SLD; however the low level of the optical signal prevents unambiguous identification. An additional 9th event with the correct "signature" was detected during a test run when we were experimenting with a new trigger scheme which is discussed in appendix B.3 and section 5.2.

4.1 "Cherenkov" Events

Long before the SLD succeeded in seeing cosmic rays by the light of air fluorescence, the system recorded events such as that shown is figure 4.1. These are caused by cascades that are directed in the general direction of the SLD. The Cherenkov light of such an event is "beamed" in the forward direction. Because the light production source travels in parallel with the produced photons at nearly the speed of light, there is a "pileup" effect wherein the the arriving photons are concentrated in an extremely short pulse: $t_r < 10$ ns. This short rise time, and the simultaneity of the signals in each of the three (Top, Middle and Bottom) fields of view are a characteristic signature of Cherenkov events.

For the SLD and the Fly's Eye [28] experiments, the vast majority of events are of this type and must be rejected from any data analysis that uses the light from air fluorescence.

Figure 4.2 represents another type of "problem" event. In this case the cosmic ray cascade passed through the SLD trailer itself. The event triggered an auxiliary scintillator paddle placed in the roof of the trailer, positioned above the PMT-BBQ photodetector assemblies. The exact mechanism by which the pulses were produced is uncertain. Possibilities include Cherenkov light in the BBQ rods, direct excitation of the BBQ waveshifter chemical and direct excitation of the the PMT cathodes.

Such events are easily eliminated due to the time signature of the pulses which is the same as for Cherenkov events. The scintillators in the trailer, and near the trailer (part of Mr. Chen's experiment) are also useful in rejecting these, and nearby Cherenkov events.

A curious effect that caused a good deal of confusion was that the rate of "Cherenkov" events seemed to increase when the wind velocity exceeded 10 km per hour. We discovered that sparks from static electricity (a wool sweater makes

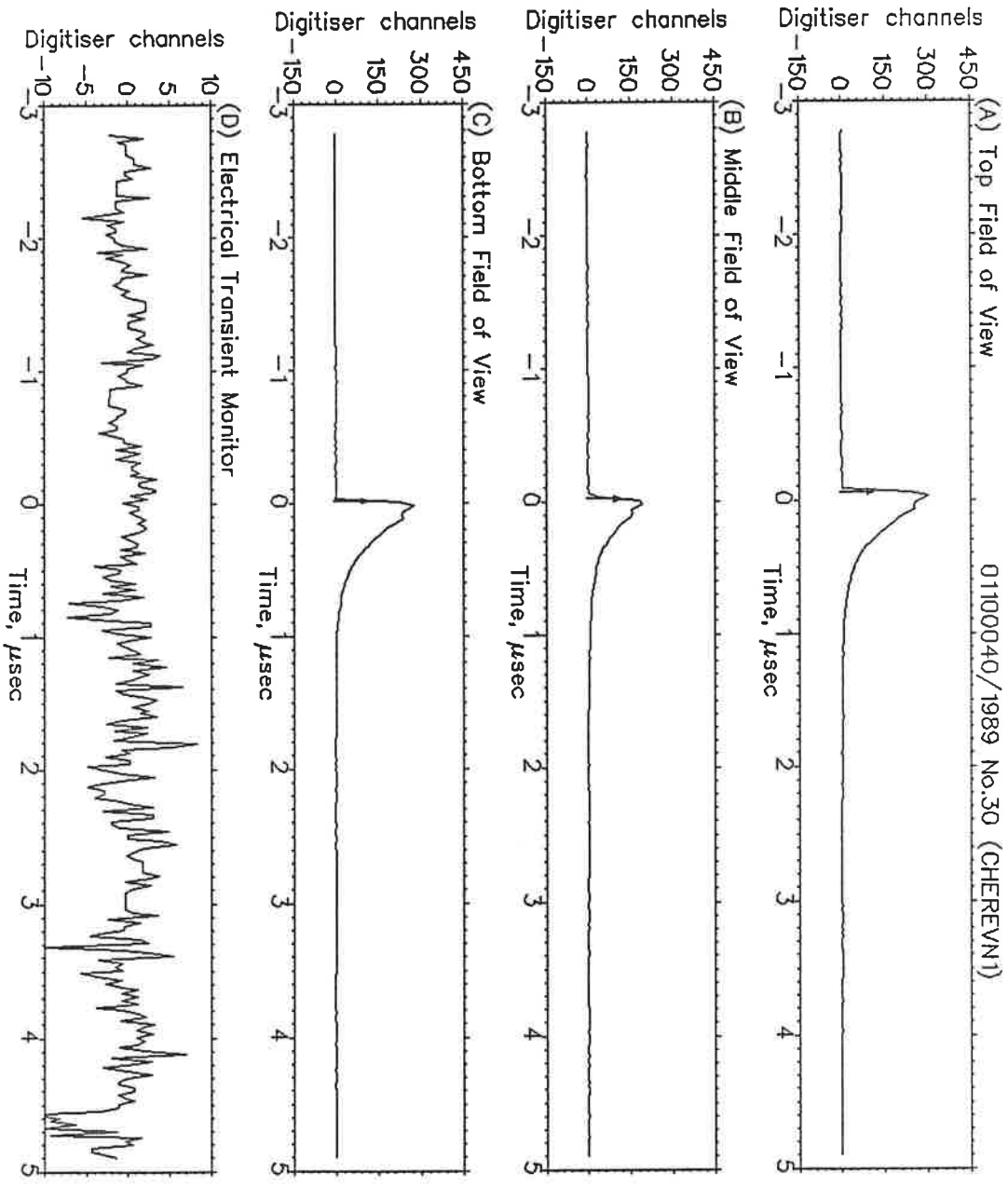

Figure 4.1: Cosmic ray event seen in the light of Cherenkov radiation.

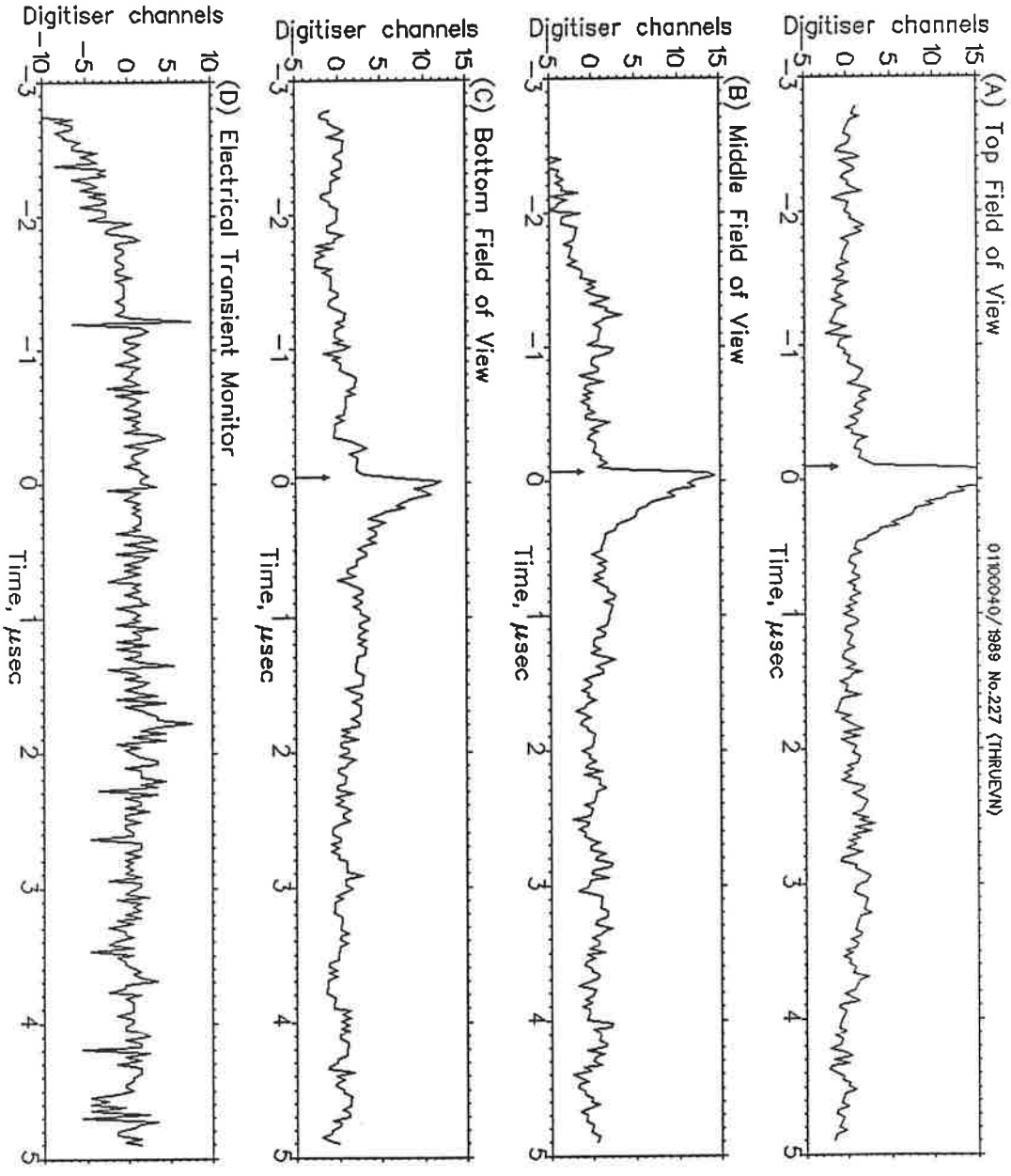

Figure 4.2: Cascade that went through the SLD trailer.

a fine pulse generator) make very fast light pulses that look to the SLD just like Cherenkov light. Moderate winds seem to generate static sparking in and near the trailer. This problem was partly alleviated by eliminating fluttering cloth objects in the trailer and grounding all metallic parts.

4.1.1 Computing the Brightness of a Fast Event

For events in which the digitized signal has a fast rise time followed by an exponential tail, the brightness H_p(photons/m^2) of the event is proportional to the pulse height:

$$\begin{aligned} H_p &= \frac{V}{S_V} \\ &= \frac{N_{ch} V_{ch}}{2 G_A S_V} \\ &= 42 N_{ch} \text{ (photons/m}^2\text{)} \end{aligned} \tag{4.1}$$

where

S_V = the SLD sensitivity (see equation 3.19),
= 5.8×10^{-6} Volts/(photons m^2)

G_A = the voltage gain of the electronics between the PMT anodes and the digitizer inputs,
= 3.1

V_{ch} = voltage of one digitizer channel,
= 1.5 mV

N_{ch} = amplitude of the pulse in number of channels.

The factor of $\frac{1}{2}$ compensates for the combination of two PMT signals into each digitizer channel.

Carrying out these computations, and averaging the results for the three field of view wedges, we find that the event in figure 4.1 had a brightness H_p=1.1$\times 10^3$

photons/m^2. Table 4.1 lists the brightness seen by the individual wedges and includes information on other events that will be discussed below.

4.2 "Air Fluorescence" Events

Figures 4.3 and 4.4 show possible cosmic ray events seen by air fluorescence light. The identification of these events as being seen by air fluorescence as opposed to Cherenkov radiation rests on the timing of the signals. The arrows indicate the time when each curve had reached 35% of its peak height. The 35% criterion was arrived at empirically. It was found to minimize the "skew" or disagreement of the middle wedge time with the midpoint time of the top and bottom wedges for simulated events generated by the PT flasher (see section 4.4).

The event of figure 4.4 was selected because it is a possible example of a combination of air fluorescence light (Top and Middle wedges) and Cherenkov light (Bottom wedge). We suspect that the downward "beam" of Cherenkov light illuminated a part of the ground or trees which was partly in the bottom field of view so we are seeing scattered Cherenkov light contamination.

In the following discussion of event timing, the approximation will be made that the light from the cosmic ray event comes entirely from the shower core – that the light is not spread out laterally. Looking back to figure 3.6(D), this approximation means we will ignore the presumed existance of the "tails" in the curves and will use only the peaks.

If there were two SLD detectors, detector 1 and detector 2, present with overlapping fields of view, then the time differences, Δt_1 and Δt_2 between the top and bottom curves' 35% points for the two detectors would allow us to determine the location and zenith and azimuthal angles of the shower core. This is part of our proposed future use of the SLD concept.

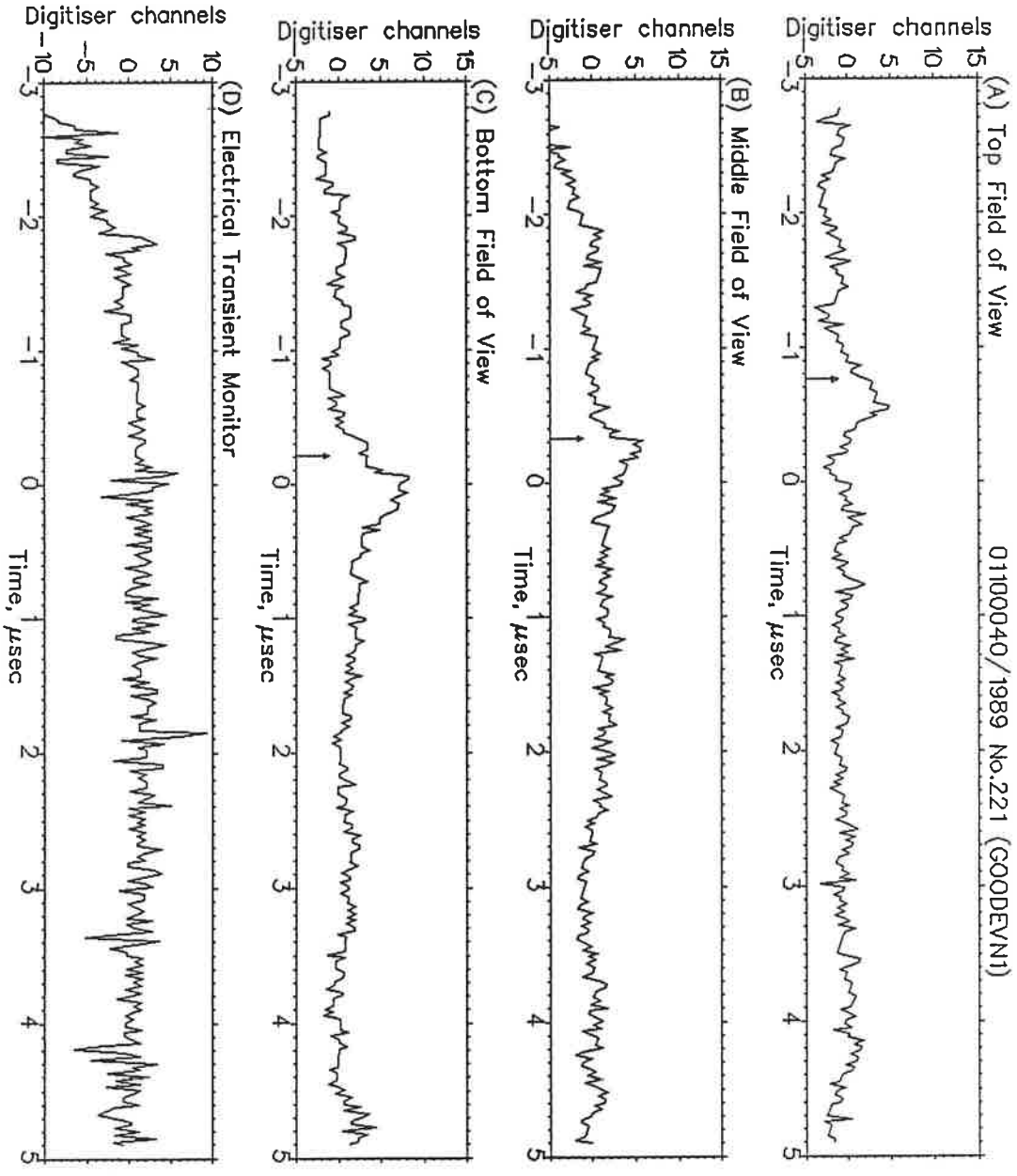

Figure 4.3: "Good event" featuring a time delay between fields of view.

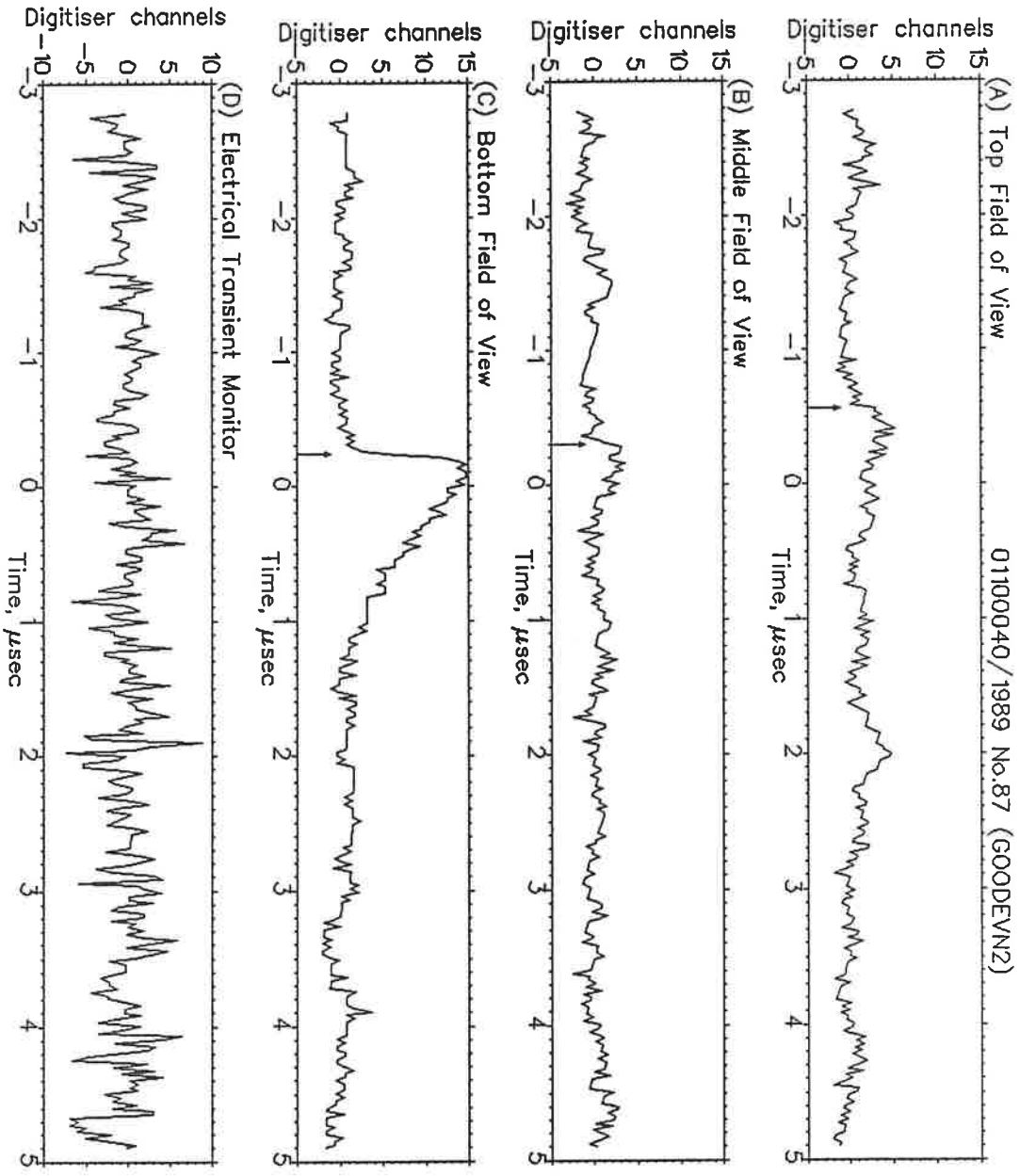

Figure 4.4: "Good event" featuring a time delay between fields of view, and possible Cherenkov contamination in the bottom channel.

However, we have only one time difference, Δt, available to us (the middle time does not improve our information on Δt), and three unknowns, r, θ and ϕ, so in order to proceed it will be necessary to make assumptions about two of the three variables.

First, we will write down an expression for the time difference as if these variables were known:

$$\begin{aligned} \Delta t &= \frac{\Delta h}{c}\left(\frac{1}{\cos\theta} - \tan\theta\cos\phi\right) \\ &= \frac{r\Delta\theta_{\text{fov}}}{c}\left(\frac{1}{\cos\theta} - \tan\theta\cos\phi\right) \end{aligned} \tag{4.2}$$

where r is the distance from the SLD to the trailer, h is the distance from the center of the top wedge to the center of the bottom wedge, $\Delta\theta_{\text{fov}}$=0.022 radians, is the respective vertical angle, θ is the zenith angle, and ϕ is the azimuthal angle with respect to a vector pointing horizontally away from the SLD trailer (see figure 2.1). The first trigonometric term in equation 4.2 accounts for the time the cosmic ray shower takes in passing from the top wedge to the bottom wedge. The second term accounts for the difference in distances from the SLD of the intersection points of the shower core with (approximately) horizontal planes in the middle of the wedges.

If we assume the shower is close to vertical, $\theta \approx 0$, then ϕ does not matter and equation 4.2 becomes:

$$\Delta t \approx \frac{r\Delta\theta_{\text{fov}}}{c};$$

$$r \approx \frac{c}{\Delta\theta_{\text{fov}}}\Delta t \tag{4.3}$$

$$= (1.4\times10^{10}\ \text{msec}^{-1})\cdot\Delta t, \tag{4.4}$$

where Δt is in seconds.

Applying this equation to the events in figures 4.3 and 4.4, we find that $r \approx 8.3$ and 4.6 km respectively.

Table 4.1: Brightness, H_p (photons/m^2), and timing information for selected events. Where it is appropriate, the distance r and number of particles, N, in the shower has been estimated.

Fig	Type	H_p wedge 1	H_p wedge 2	H_p wedge 3	Δt nsec	r km	N e^+,e^-
4.1	Cherenkov	1.3×10^4	8000	1.2×10^4	0	–	–
4.3	"Good"	154	243	596	600	8.3	2.2×10^9
4.4	"Good"	378	132	1530	330	4.6	6.6×10^8
4.6	PT flash	2490	1930	1320	330	0.9	–
4.5	"Remote"	111	228	437	980	>0.9	–

4.2.1 Computing the Brightness of a Slow Event

For events that have a slow risetime or are lacking an exponential tail, the technique of section 4.1.1 is not applicable. Instead we must integrate the current from the PMT through resistor R (see figure 2.8) to arrive at the charge and scale by the appropriate gains:

$$\begin{aligned} H_p &= \frac{Q}{S_Q} \\ &= \frac{1}{S_Q}\int I(t)dt \\ &= \frac{1}{S_Q}\int \frac{V(t)}{R}dt \\ &= \frac{1}{S_Q}\int \frac{N_{ch}(t)V_{ch}}{2RG_A}dt \\ &= \frac{V_{ch}t_{bin}}{2RS_QG_A}\sum_t N_{ch}(t) \\ &= (3.5 \text{ photons/m}^2)\cdot\sum_t N_{ch}(t) \end{aligned} \tag{4.5}$$

where, in addition to the variables introduced in section 4.1.1 we have introduced

S_Q = the SLD charge sensitivity (see equation 3.19),

t_{bin} = width of digitizer bin = 25 ns,

R = resistance to ground at PMT anode.

Once again, the factor of $\frac{1}{2}$ compensates for the combination of two PMT signals into each digitizer channel.

The data analysis software computes the summation and the resulting values of H_p for the events in figures 4.3 and 4.4 are 331 and 255 photons/m^2, respectively. (These are average values for the field of view wedges.) In the calculation of the brightness of the event in figure 4.4 the bottom channel of data was not used because of the suspected Cherenkov contamination. Table 4.1 shows statistics on each of the events including the number of photons in each field of view wedge.

4.2.2 Converting Brightness to Primary Energy

Given the above information, we can compute to within, perhaps, a factor of 2, the primary energy of the cosmic ray events. Continuing with the approximation of all the light being produced in the shower core, the brightness H_p is related to the number, $N(E_0)$, of particles in the shower by the relation

$$\begin{aligned} H_p &= \frac{\epsilon_p(r)N(E_0)}{4\pi r^2} \cdot \frac{\Delta h}{\cos\theta} \\ &= \frac{\epsilon_p(r)N(E_0)}{4\pi r} \cdot \frac{\Delta\theta_{\text{wedge}}}{\cos\theta}. \end{aligned} \tag{4.6}$$

The second factor in equation 4.6 represents the path length of the core through the field of view of a PMT whose vertical extent, $\Delta\theta_{\text{wedge}}$, is 0.62° or 0.011 radians.

Solving for $N(E_0)$ gives

$$N(E_0) = \frac{4\pi r \cos\theta H_p}{\epsilon_p(r)\Delta\theta_{\text{wedge}}}. \tag{4.7}$$

Note that we have to estimate ϵ_p, the effective light production efficiency of the cascade, which is a function of the distance from the SLD: $\epsilon_p(r = 8.3 \text{ km}) =$

1.4, $\epsilon_p(r = 4.6 \text{ km}) = 2.0$ photons per meter per electron for a visibility of 129 km. (See section 3.3 for how ϵ_p is calculated.) The visibility was 129 km (70 miles), unusually clear, the night these events were seen.

With the assumption that $\theta \approx 0$, equation 4.7 gives $N(E_0) = 2.2\times10^9$ and 6.6×10^8 particles for the events of figures 4.3 and 4.4, respectively.

Now that we have the number of particles, $N(E_0)$, we would like to estimate the primary energy, E_0. We can solve equation 3.2 for E_0, but for the present examples interpolating between the curves of figure 3.2 will suffice. We find that at an altitude of 1100 meters we can say $E_0 \approx 0.9\times10^9 N$. Therefore $E_0 \approx 2\times10^{18}$ and 6×10^{17} eV for the events of figures 4.3 and 4.4, respectively.

4.3 A "Remote Array" and "AirFluorescence" Event

The event in figure 4.5 is interesting in that it shows a possible coincidence detection of a cascade by the remote scintillator array and the SLD itself. The late arrival time of the pulses, with respect to the $t = 0$ point on the time axis of each trace, indicates that the optical pulse arrived after the arrival of the signals from the remote scintillator array. This peculiarity can be explained by possibility that the shower core was some distance further away from the SLD than the remote scintillators. The large time differential between top and bottom field of view pulses can be explained by assuming the shower was slanted away from the SLD.

4.4 "Photon Torpedo" Events

As a check of the day-to-day performance of the SLD system we installed a light flasher a distance of 882 m from the trailer (see figures 2.2 and 2.7) which we will call the PT flasher. The PT flasher provided a model of cosmic ray events by emitting a flash of light that underwent Rayleigh and Mie scattering off of the

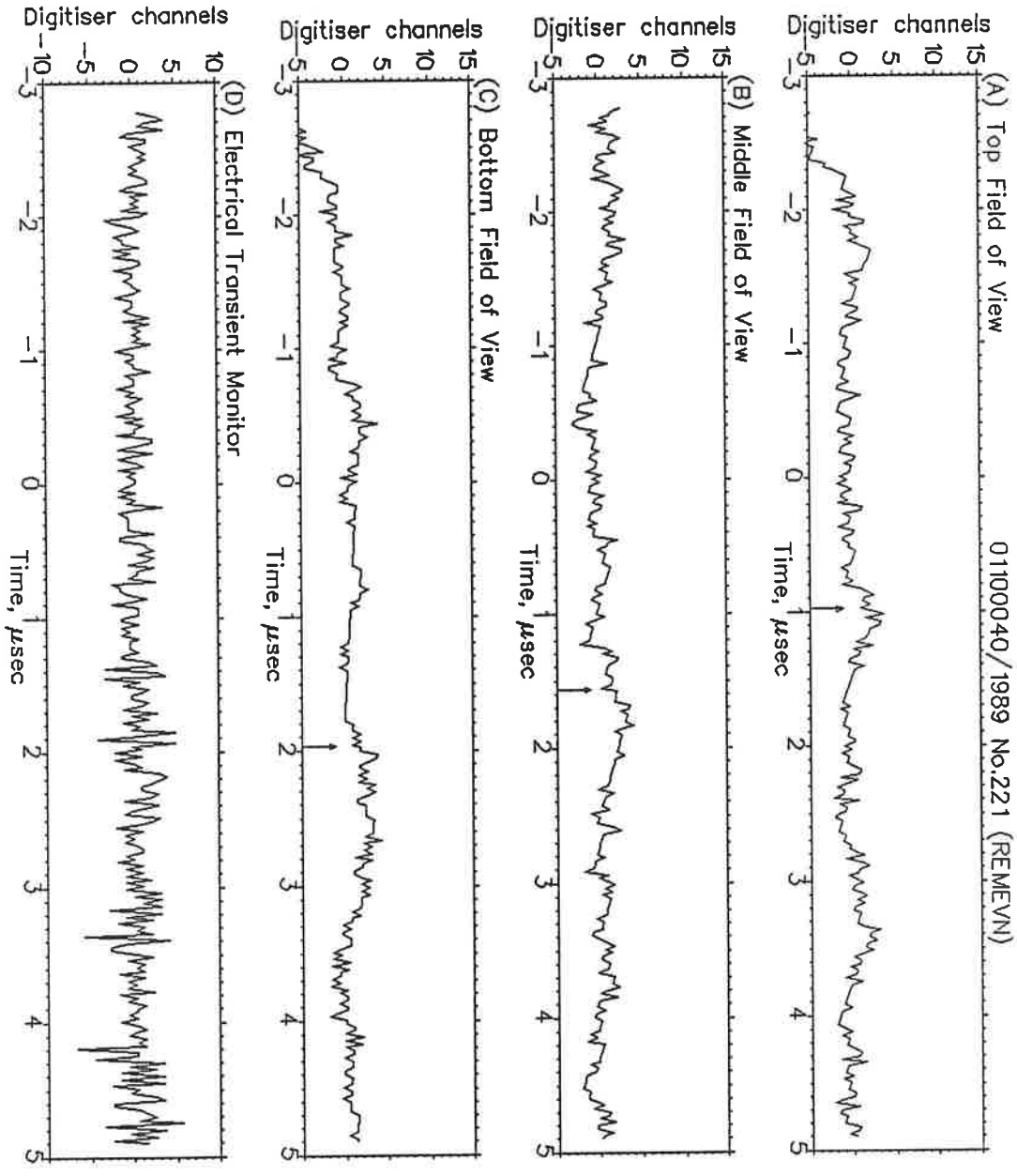

Figure 4.5: Event triggered by the remote scintillator array. Time delay with respect to the $t = 0$ point indicates that the signal from the remote scintillators arrived prior to the optical pulse.

molecules and dust in the air. To the SLD, this looked like a spot of light moving at the speed of light, much as a real event would appear, except that a real event would travel downward, not upward.

Its was fascinating to have someone turn the PT flasher while watching the timing characteristics change on the computer display in the SLD trailer. (We used CB radios to keep in touch.) In the PT event shown in figure 4.6, r=882 m, the orientation is θ=240° (60°+ 180° to account for the backwards propagation with respect to a downward moving event) and ϕ=0. The timing formula, equation 4.2, may be used to predict the time difference, giving an expected $\Delta t = 240$ nsec. The actual time difference for the event in figure 4.6 (using the previously mentioned 35% of pulse height criterion) is 330 nsec.

It may be pointed out that if the PT flasher, which internally consists of a Xenon flash lamp, can appear like a cosmic ray event, then couldn't an aircraft's flash beacon do the same thing? The answer is yes, but... In order to make the PT flasher have both high intensity and a pulse risetime of less than a microsecond required a special low inductance design. In aircraft beacons, the risetime is of no interest to the designers so we can expect the risetime to be at least 5 microseconds, much longer than the expected cosmic ray events.

4.5 Other Events

Figure 4.7 shows (in the top wedge only) pulses from a test light source that was used in determining the gain, G, of the PMTs. The source was a small ($\approx$ 5 mm diameter) "pill" of scintillator plastic that had embedded in it a small quantity of the radioactive isotope Cesium-137. One of the features of the decay scheme of ^{137}Cs is the emission of internal-conversion electrons with precisely .662 MeV of kinetic energy.

The electrons come to rest in the plastic, so all the kinetic energy goes

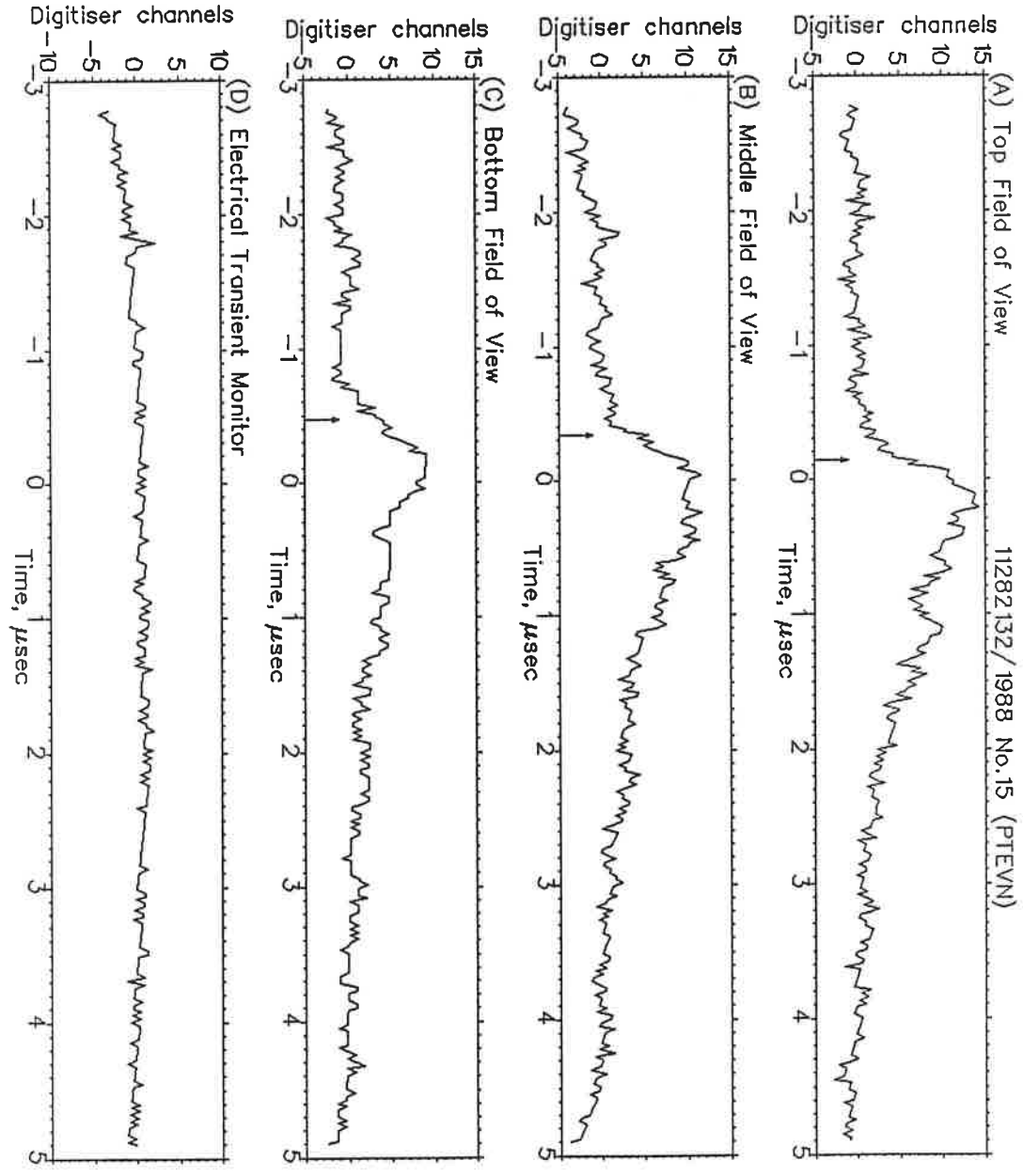

Figure 4.6: "Photon Torpedo" event. Beam of light originated 1km from the SLD and was directed 30°above the horizon away from the SLD.

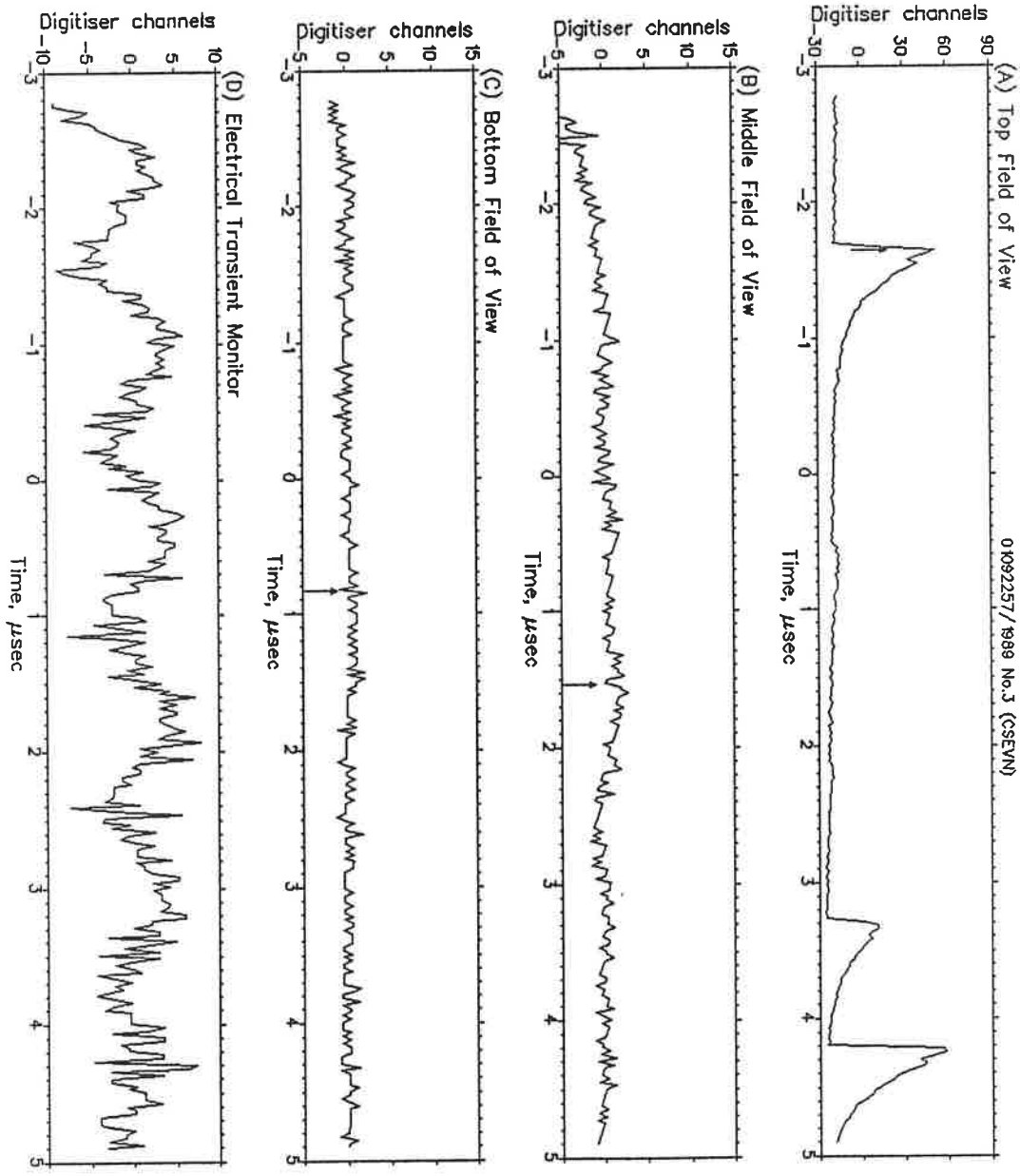

Figure 4.7: Pulses from the light of a radioactive ^{137}Cs source embedded in scintillator placed on the top left PMT photocathode.

into ionizing the plastic's molecules, producing flashes of light. About 100 eV of ionization loss will produce a photon from the scintillator so the pulses of light should have about 6600 photons each. The scintillator "pill" was covered with aluminum foil on the back and side to make sure all the light went out the front, which was applied to the face of the PMT under test. The size of the anode pulses thus produced allowed us to determine the gain of the tube.

Figure 4.8 is included to give a flavor of type of experiment this was. Life was tough out in the desert, and the desert rats and mice were a continuing problem. They chewed through cables, made nests in the PMT housings and in the Camac power supply. The heat deformed the acrylic mirrors and caused the electronics to lose calibration and break down.

The pulses shown in figure 4.8 were caused by arcing in a high voltage cable powering one of the outdoor scintillators. The arcing occurred because an animal tried to eat the cable.

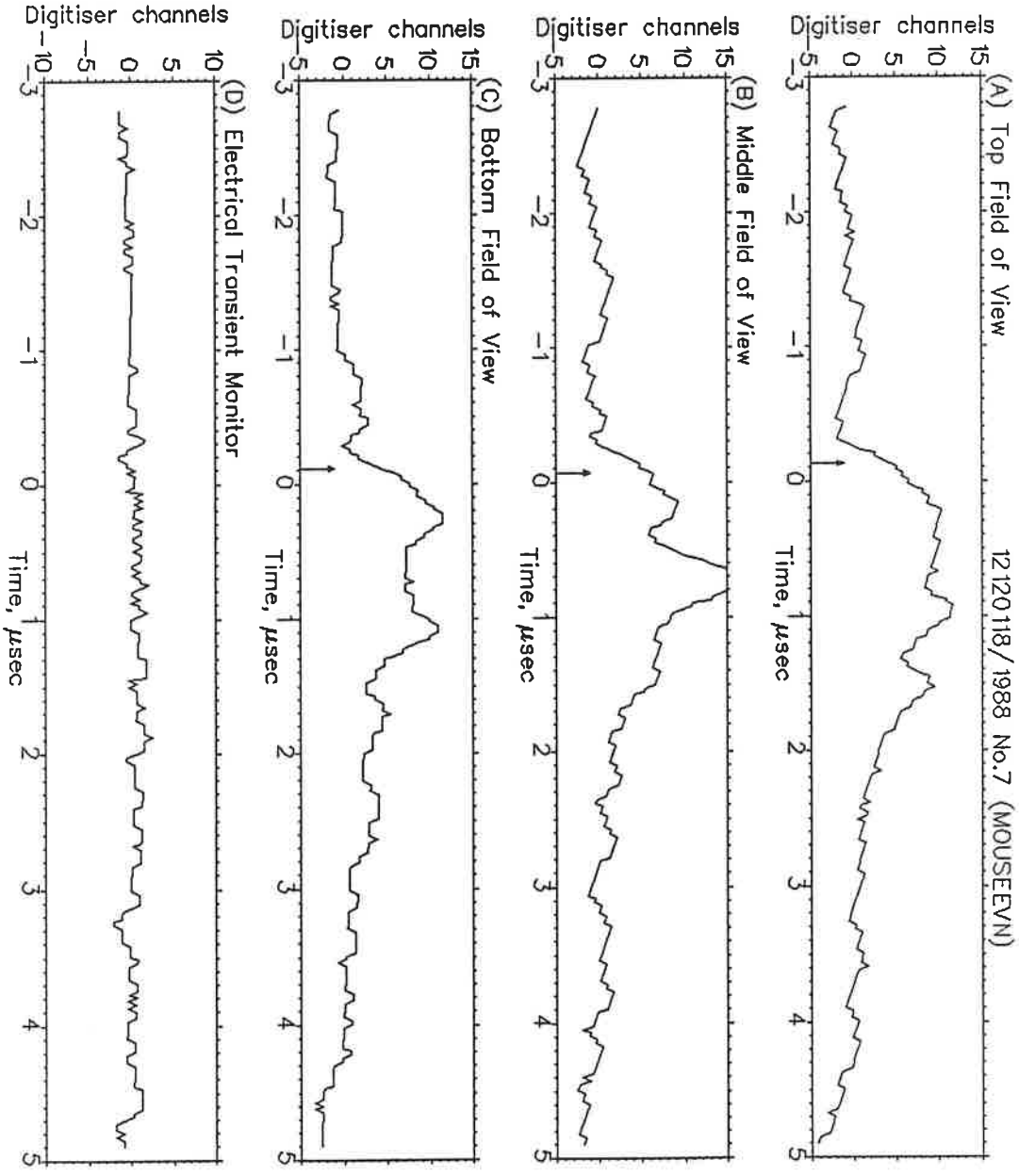

Figure 4.8: "Mouse event." Light from the arcing of a rodent-damaged high voltage cable.

Chapter 5

Conclusions and Future Developments

5.1 Conclusions

We have demonstrated that it is feasible, both technically and economically, to build detectors for extensive air showers using the Side Looking Detector concept, which uses the atmosphere as a scintillator of huge area capable of exploring the cosmic ray spectrum at energies greater than 10^{18} eV.

The prototype SLD took approximately 110 hours of data over 39 nights during the two year period it has been in the field. Of this live time, perhaps 20% can be considered "real" in the sense that the SLD was fully functional and operating under good climactic conditions. Because of the steep fall-off $\sim E_0^{-2.5}$ in the flux of cosmic rays with energy exceeding E_0, a small change in the sensitivity of the apparatus results in a large change in the detectable event rate. Therefore it should not be surprising that most of the "real" events were seen over a two night period when the visibility was exceptionally good and the data acquisition equipment was tuned to the best level of sensitivity achieved in this project.

Altogether 9 events were identified as having the correct "signature" for cascades seen in the light of air fluorescence. One of these events was estimated to have a primary energy E_0 of, very roughly, 2×10^{18} eV.

The energy threshold of detectability of events depends largely on the amount of background light and on the amount of attenuation of light due to Mie and Rayleigh scattering. We estimate that the prototype SLD can see 10^{18} eV

events out to a distance of 7 km and 10^{19} eV as far as 20 km during the periods of 80 km visibility typical of the Tucson area (see table 3.2). This translates into a total acceptance $A\Omega$ of 17 km^{2}sr and 140 km^{2}sr for 10^{18} and 10^{19} eV respectively, assuming an angular acceptance Ω=1 sr.

In order to get unambiguous data on the energy and direction of origin of the cosmic rays, one must build at least two (and preferably three for data cross-checks) SLD detectors for each section of detector area. Therefore the effective acceptance of the SLD approach becomes about 70 km^{2}sr per detector for a threshold of 10^{19} eV. The acceptance is likely to increase as the SLD design is refined, as will be discussed below. At a cost of $20,000 to $50,000 per detector, this is the least expensive way to proceed.

Note that the SLD cannot run when the sun or moon are present, so the time-averaged acceptance should be multiplied by the duty cycle of the detector which would be roughly 20% for a fully operational facility.

The question we might now ask is "where do we go from here?" There is much that could be done in the areas of technical improvements and in the large-scale deployment of the SLD concept.

5.2 Improving the Side Looking Detector

Before proceeding with the mass production of SLD detectors, it would be advisable to use the experience gained in the present experiment to make a more sophisticated design which will be more sensitive, accurate and reliable. The following is a list of possible improvements:

- Larger mirrors. The dimensions of the present SLD apparatus were dictated by the desire of our group to assemble the detector at the university and then transport it to the experiment site. Because of legal constraints on what the

dimensions of our trailer could be, we had to limit the mirror size and focal lengths to 2.4 m (8 ft) square, and 1.8 m (6 ft), respectively. If the optics and enclosure could be assembled at the field location, then a much larger optical collecting area could be achieved. The signal-to-noise ratio will scale as the square root of the mirror area.

- Improved mirror design. One of the more tedious aspects of conducting this experiment was the periodic readjustment of the mirror alignment screws (see section D.1). It is almost essential that a more durable design be found which will allow the figure of the mirrors to be set once, and not have to be readjusted every time there is a large temperature change.

- Narrower bandwidth. A way the increase the signal-to-noise ratio is to narrow the range of wavelengths the SLD is sensitive to. The obvious way to do this would be to put filters in front of the BBQ waveshifter rods. A potentially more efficient way to do this, however, would be to use lower concentrations of the BBQ waveshifter chemical. This would narrow the effective absorption band of the waveshifter bars because the low efficiency "tails" of the absorption spectrum would cease to capture light outside of the wavelength range that we are interested in. This effect can be seen by comparing the BBQ absorption spectra of references [18] and [19] .

- More fields of view. By dividing the field of view of the SLD into finer wedges, one can see more detail in the shower structure and achieve a greater degree of noise rejection. It would certainly be sensible to record separately the data from the six PMTs in the current apparatus rather than mixing the signals in pairs.

- Summed trigger. As mentioned in appendix B.3, we have found that we can improve the trigger efficiency over that of the majority logic currently in use. This is done by summing all of the PMT signals together, and using a single discriminator to trigger the electronics. We have recently tested this idea

and found it to work well. In addition, since there is only one channel, we were able to further improve our noise rejection by adding an extra stage of filtration in front of the discriminator. A disadvantage of this trigger is its sensitivity to Cherenkov light pulses, which often produce a signal in only one of the field-of-view wedges (which would be rejected by a majority logic trigger). This problem can be corrected with the implementation of the next suggested improvement.

- Software event selection. The SLD experiment has recorded thousands of events attributable to Cherenkov radiation for only a handful of events observed in the light of fluorescence radiation. While this behaviour is consistent with the experience of the Fly's Eye group [28], it means that it is desirable to do more to reject the Cherenkov events while increasing the overall trigger sensitivity. In the present experiment the threshold is set to as low a level as possible without resulting in a flood of events. All events are recorded, and are later kept or rejected on the basis of further analysis. If we are to set the threshold even lower, we will be forced to reject more events via software analysis as they arrive; otherwise we will not be able to handle the large amounts of data that will accumulate. This will require a computer controlling the experiment more powerful than the 4.7 MHz 8088 IBM XT currently in use.

- Unmanned, remote operation. A full scale implementation of the SLD concept should use automated detector stations that can run for extended periods (e.g. weeks) without human intervention. Such a system would require less manpower and probably would have a higher duty cycle than a system requiring continuous manning of each detector, as the prototype did. This would require data links, via telephone, radio or perhaps satellite between the home base and the detectors.

5.3 Locating a Future SLD Experiment

For the purposes of further refining the technique and calibrating the equipment, it would be logical to install the SLD at a location such as the Fly's Eye where cosmic ray cascades could be detected both with the new apparatus and with an existing, well-calibrated detector. Such an arrangement would facilitate the fine-tuning of the triggering and data acquisition technique and provide well characterized events for which the SLD response could be saved and incorporated into calibration formulae. The actual location of the Fly's Eye, Dugway Proving Grounds, 70 miles southwest of Salt Lake City, in not ideal for a long-term SLD experiment because of the absence of convenient mountain sides which would provide a suitably dark backdrop for the lowering of the background light level.

In the long run, we will need to find a truly appropriate location for a large scale SLD installation. The criteria for a suitable site include the following:

- Weather. Because the visibility has a strong impact on the effective acceptance $A\Omega$ of the SLD, it is desirable to use locations where the visibility $V \geq 80$ km for most of the year. Although world-wide listings of V are not readily available, we can start by considering areas with low rainfall.

- Topology. Since the Side-Looking Detector concept works best where a dark backdrop, 20 to 30 km away, is available to reduce the background light level, it is desirable to find locations with steep mountain sides, or perhaps canyon walls.

- Light pollution. Areas with low population densities are desirable since these areas will have lower background light levels.

- Accessibility (and utilities). One cannot conduct an experiment if there is no access (or no electricity). Unfortunately, areas with convenient roads (and utilities) will tend to be regions with higher levels of light pollution.

The question of utilities can be circumvented if each detector has its own power source, such as solar panels and storage batteries, or gasoline powered generators.

- Astrophysical considerations. Locating the SLD system in the southern hemisphere would help test the possibility that there exist southern sources of UHE particles that could not have been noticed by northern hemisphere detectors such as the Fly's Eye. Conversely, locating in the northern hemisphere would allow coordination with existing detectors, a useful capability when searching for cosmic ray bursts or time-varying point sources.

Note that the altitude of the SLD system is not an essential consideration in choosing a site. Because vertical events with $E_0 > 10^{19}$ will have over 10^{10} particles almost down to sea-level (fluctuations will cause significant variations in cascade development), high altitude is not a significant asset. High altitude is not a significant disadvantage either, since the highest energy cascades, which might reach maximum development after traversing more than one atmosphere of depth, can still be observed if they are sufficiently inclined. Perhaps a more immediate benefit of a high altitude site would be better visibility, since the air might be both cleaner and drier.

A preliminary scan of world geography with an atlas such as reference [29] leads the author to suggest the following regions as most suitable:

- The United States Southwest region where the SLD prototype and the Fly's Eye are currently situated.
- The western coast of South America has an arid region known as the Atacama Desert. It is in northern Chile, on the western flank of the Andes Mountains. For example, there exists a dry lake bed southeast of the city of Iquiqe which has approximately the right dimensions, is surrounded by mountains and appears to be accessible.

- The western coast of South West Africa is an arid and mountainous region known as the Namib Desert, which may be suitable.
- The central region of Australia is both dry and very isolated. There may be suitable sites in the environs of Alice Springs.

It has been the experience of the author that it is relatively easy to find sites that "on paper" appear to be suitable, yet upon further inspection fail to be practical, usually because of light pollution or lack of accessibility.

It is the intention of the author to promote the construction of detectors of ultra-high energy cosmic rays. At the time of this writing, we are not aware of any method to accomplish this that is more cost-effective than the Side-Looking Detector concept.

Appendix A

Miscellaneous Calculations

A.1 List of Variables and Symbols

For the convenience of the reader (and the author) the most important variables are listed below.

$\alpha(\lambda)$ = attenuation coefficient of light through air due to Mie and Rayleigh scattering (km^{-1}). (Strongly wavelength and weather dependent.)

A_{eff} = effective light collection area of the SLD including mirror surface, light pipe and PMT quantum efficiencies [$=E_{\text{BBQ}}F_{\text{BBQ}}E_{\text{mirror}}E_{\text{PMT}}\cdot$(mirror area)].

C = capacitance of a PMT anode to ground.

$\Delta\theta_{\text{fov}}$ = vertical angle between the center of the top field of view and the bottom field of view (=1.24°).

$\Delta\theta_{\text{wedge}}$ = vertical angle of the field of view of a PMT pair, called a wedge in this paper (=0.62°).

$\Delta\theta_{\text{BBQ}}$ = vertical angle of the field of view of a BBQ waveshifter rod (=0.31°).

$\Delta\phi_{\text{BBQ}}$ = horizontal angle of the field of view of a BBQ waveshifter rod (=41°).

$\Delta(\vec{r})$ = number of charged particles per square meter in a cosmic ray cascade at position $\vec{r}$ (which is assumed to be on the shower front). (See figure 2.3)

E_0 = primary energy of cosmic ray cascade (eV).

E_{BBQ} = ratio of the number of photons entering a PMT to the number entering a BBQ waveshifter rod. Includes the efficiencies of the fluorescent chemical, defects in the rods, and imperfect coupling to the PMT.

E_{mirror} = reflectivity of the SLD mirror.

$E_{\rm PMT}$ = quantum efficiency of the PMT at the wavelength of the BBQ output.

ϵ_0 = critical energy (=84.2 MeV in air).

ϵ_p = number of photons per meter emitted by the ionization track of a relativistic charged particle in air ($\approx$3.1).

$\epsilon_p(r)$ = effective value of ϵ_p after including losses due to light scattering.

$F_{\rm BBQ}$ = fraction of the focal region filled with BBQ waveshifter (=0.8).

G = gain (charge multiplication factor) of a PMT.

$G_{\rm A}$ = voltage gain of the amplifier chain from PMT anode to digitizer input (=3.1).

h = altitude (meters above sea level).

h_{SLD} = altitude of the SLD experiment (= 2992 ft, or 912 m).

H_p = brightness at SLD (time-integrated light intensity) of an event (photons $\rm m^{-2}$).

$H_{\rm rms}$ = noise of the SLD expressed in terms of time-integrated light intensity. Integration time is τ, the RC time constant of the PMT base and electronics (photons $\rm m^{-2}$).

$H_{\rm thresh}$ = event selection threshold brightness of SLD electronics and data analysis software (photons $\rm m^{-2}$).

J = background light intensity in the sensitive wavelength range of the SLD [photons/($\rm m^2$sr)].

N_{pe} = number of photoelectrons emitted by a PMT photocathode due to an event.

Ω = field of view of one PMT-BBQ photodetector assembly (sr).

$\vec{r}$ = position of a point in a cascade with respect to the SLD (=distance from SLD).

R = PMT anode-to-ground resistance (ohms).

$R_{\rm acc}$ = accidental rate = rate at which noise fluctuations exceed $H_{\rm thresh}(\rm sec^{-1})$.

$R_{\rm back}$ = background rate of photoelectrons from a PMT cathode due to dark current and background light ($\rm sec^{-1}$).

$\rho(h)$ = air density (=1.126×10^{-3}g/$\rm cm^3$at SLD altitude).

r_l = radiation length (=37.3 g/$\rm cm^2$ in air).

S_Q = sensitivity of the SLD in terms of the charge at the PMT anode per unit of time-integrated light intensity [coulombs/(photon m^{-2})].

S_V = sensitivity of the SLD in terms of the voltage at the PMT anode per unit of time-integrated light intensity [volts/(photon m^{-2})]. (Applicable only for events with pulse width $\ll \tau$.)

τ = RC time constant of the combined PMT anode and preamp (emitter follower) which effectively form filter stage 0 (=0.3 μsec).

t_{bin} = time of digitizer bin (=25 nanoseconds). (40×10^6 samples per second.)

$V_{rms,pe}$ = photoelectron noise measured at the PMT anode with time constant τ.

X = atmospheric depth (=915 g/cm^2 at SLD).

A.2 The Atmosphere at Low Altitudes

The development of a cosmic ray cascade is a function of the amount of material, i.e. air, that it passes through. This is called the atmospheric depth X, and is usually expressed as the number of grams per square centimeter between the elevation in question and the vacuum of space. Assuming constant gravitational acceleration for the lower 20 km,

$$X(h,\theta) = \frac{p(h)}{g\cos\theta}$$

where $p(h)$ is the pressure at altitude h, in meters above sea level.

Using the 1962 standard atmosphere [22] as a starting point, a good fit to the pressure profile at low altitudes is given by

$$p(h) = p_0 e^{-h/7519} \tag{A.1}$$

where $p_0 = 1.01325\times10^5$ newtons /m^2, the pressure at sea level.

Dividing by equation A.1 by g and converting to cgs units, we obtain

$$X(h) = \frac{X_0 e^{-h/7519}}{\cos\theta} \tag{A.2}$$

where X_0 is 1033 g/cm^2, the vertical atmospheric depth at sea level.

The air density may be fit by the following expression:

$$\rho(h) = 1.243\times10^{-3} e^{-h/9259} \quad \text{g/cm}^3 \tag{A.3}$$

Note that the coefficient in front of the exponent is not the sea level density (although h is still the altitude above sea-level). Instead, the numbers have been adjusted to give good agreement at the SLD altitude and there will be a slight deviation from the correct air density much lower and higher altitudes.

A.3 Light Attenuation at SLD Altitude

Light traveling through the atmosphere will be attenuated due to scattering and absorption before arriving at a distant observer. At the wavelengths of interest, $3371 \leq \lambda \leq 4278$ Å, absorption is not significant since the wavelengths are longer than those in the ozone absorption wavelength range and are below the water and CO_2 absorption bands. At these wavelengths, Rayleigh and Mie scattering will be the dominant effects.

Rayleigh, or molecular scattering is proprtional to $(1/\lambda)^4$ and thus rapidly becomes the dominant effect for the shorter end of our wavelength range. Rayleigh scattering has a slow, $1 + \cos\theta$ angular dependence, so it is important for all scattering angles.

Mie, or aerosol scattering is a complex function of particle size, shape, refractive index, scattering angle and wavelength. Mie scattering tends to be most important for small scattering angles.

Many measurements of the attenuation of light through the atmosphere have been made but none that the author has found are precisely appropriate for the circumstances of the SLD. Two sets of scattering data will be considered, and a "compromise" formula which falls between the data sets will be used.

The first set of data is from figure 7-3 of reference [30] and represents the attenuation over a horizontal path at sea level in a model clear standard atmosphere. This is a worst-case approximation since we are at a higher altitude and the skies in Arizona are clearer than for typical geographic locations. These values of $\alpha(\lambda)$ are listed for selected atmospheric fluorescence wavelengths in table A.1, in the worst-case column.

The second set of data is from figure 7-1 of reference [30] (or page 139 of reference [31]) and is derived from the attenuation of light from above the atmosphere, vertically down to sea level, for 80 km (50 mile) visibility, and 2 precipitable cm of water for one air mass. This represents a best-case since the 80 km visibility is considered excellent and because much of the path is above the aerosols which tend to be concentrated at low altitudes. To use this data, the one air mass has to be converted to an equivalent distance for the average air density that the light will traverse for SLD events. This comes to 9.4 km. The resulting values of $\alpha(\lambda)$ are listed in the best-case column of table A.1.

Kingslake, in reference [31], page 137, gives a formula which approximates $\alpha(\lambda)$ for varying weather conditions as expressed by the visibility V, which is reported daily by the national weather service:

$$\alpha(\lambda) = \frac{3.9}{V}\left(\frac{5300}{\lambda}\right)^{.62V^{1/3}} \tag{A.4}$$

where V is in km and λ is in Ångstroms. The actual visibility at Tucson International Airport, which is 25 miles north of the SLD, varies from 60 to 100 km for typical clear weather, as can be seen in figure A.1. Therefore, the values of $\alpha(\lambda)$ have been computed for V=80 km (50 miles) and listed in the compromise column

Table A.1: Atmospheric attenuation coefficients for worst-case, best-case and a calculated compromise case (visibility V=80 km) for the wavelengths at which the excited nitrogen ions in air will fluoresce.

λ Å	$\alpha(\lambda)$ km^{-1} worst-case	$\alpha(\lambda)$ km^{-1} compromise	$\alpha(\lambda)$ km^{-1} best-case
3371	.33	.16	.11
3537	.32	.14	.085
3577	.31	.14	.081
3756	.27	.12	.070
3805	.26	.12	.066
3914	.25	.11	.058
3998	.24	.10	.051
4059	.23	.099	.049
4278	.22	.086	.046

of table A.1. These are the values that were used to estimate the attenuation of light for cosmic ray events in section 3.3.2.

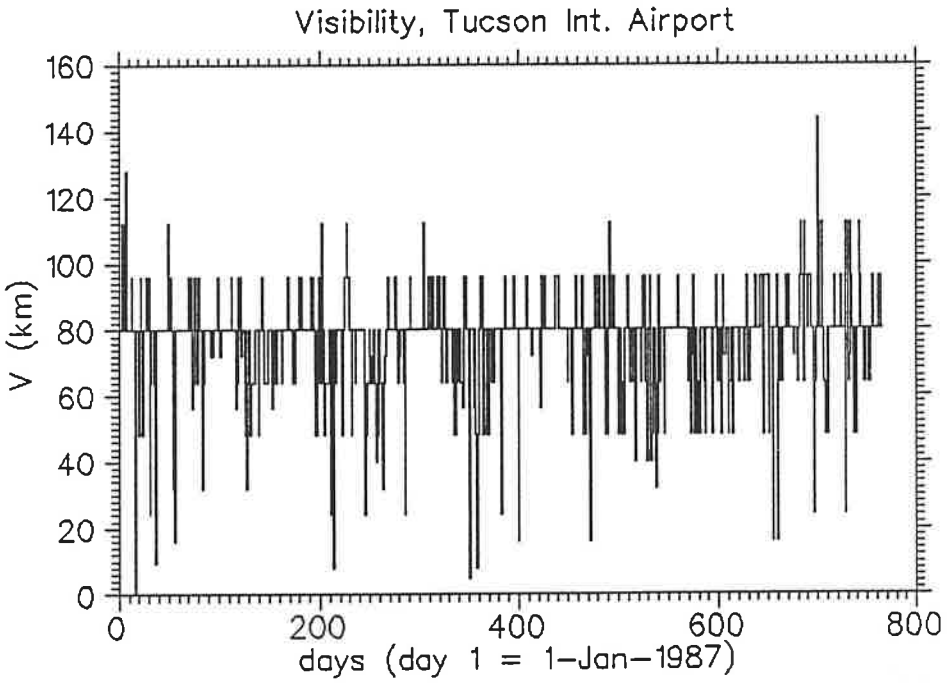

Figure A.1: Visibility at the Tucson International Airport as estimated by the National Weather Service at 5 P.M. MST daily from January 1987 through January 1989.

Appendix B

System Triggering

One of the greatest challenges in making an experiment such as this to work is not so much *getting* the data as it is deciding *when* the data is present. This is the task of the trigger electronics.

The SLD experiment took data whenever all or a majority of the field-of-view inputs detected a photon flux above a certain threshold value. The way that this was done is diagramed in figure 2.9.

The signal from each of the photomultipliers was filtered and amplified and fed to six discriminators. These discriminators' outputs went to a six input majority logic (ML) gate. Whenever a logical true appeared at the ML gate's output, the Camac data taking modules and the computer were triggered.

B.1 Signal Filtering

In this section we will discuss the effect of signal filtering on the reliability of triggering. The largest source of noise in this experiment is the shot noise due to the discrete nature of the number of photons and of the electron charge. Under good conditions, the background light causes a flow of about 100 photo-electrons per μsec. The response of the photomultiplier tubes and amplifiers is very fast; a single electron pulse is $\approx$ 5 nsec wide, without the filters. Since we are interested in events that are hundreds of nanoseconds wide, and since the shot noise is a broadband signal, flat up to about 100 MHz, we can use filters to greatly improve

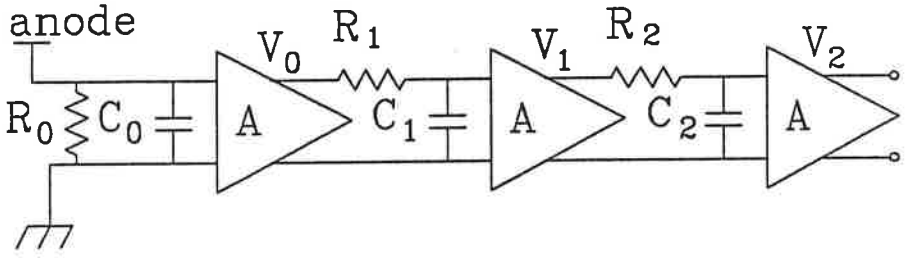

Figure B.1: Arrangement for discussion of effects of filtering on S/N ratio. In the final phase of the experiment, only the zeroth stage was used. In the discussion, the gain of the amplifiers is taken to be one.

the signal-to-noise ratio.

Consider the arrangement shown in figure B.1. Assume the signal entering the filter chain from the PMT anode is a rectangular current pulse t_r seconds wide that contains a total charge q_0. The RC time constant for each stage is τ.

The form of the signal after each stage is easily calculated using the technique of Laplace Transforms.

After the zeroth filter we have

$$V_0 = \frac{R_0 q_0}{t_r}\left\{[(1-e^{-t/\tau})U(t)]_t - [(1-e^{-t/\tau})U(t)]_{t-t_r}\right\} \tag{B.1}$$

where

$$U(t) = \begin{cases} 0 & t<0 \\ 1 & t \geq 0. \end{cases}$$

After filters 1, 2 and 3 we have

$$\begin{aligned} V_1 &= \frac{R_0 q_0}{t_r}\{[(1-(1+t/\tau)e^{-t/\tau})U(t)]_t \\ &\quad -[(1-(1+t/\tau)e^{-t/\tau})U(t)]_{t-t_r}\} \\ V_2 &= \frac{R_0 q_0}{t_r}\{[(1-(1+t/\tau+\frac{1}{2}(t/\tau)^2)e^{-t/\tau})U(t)]_t \end{aligned} \tag{B.2}$$

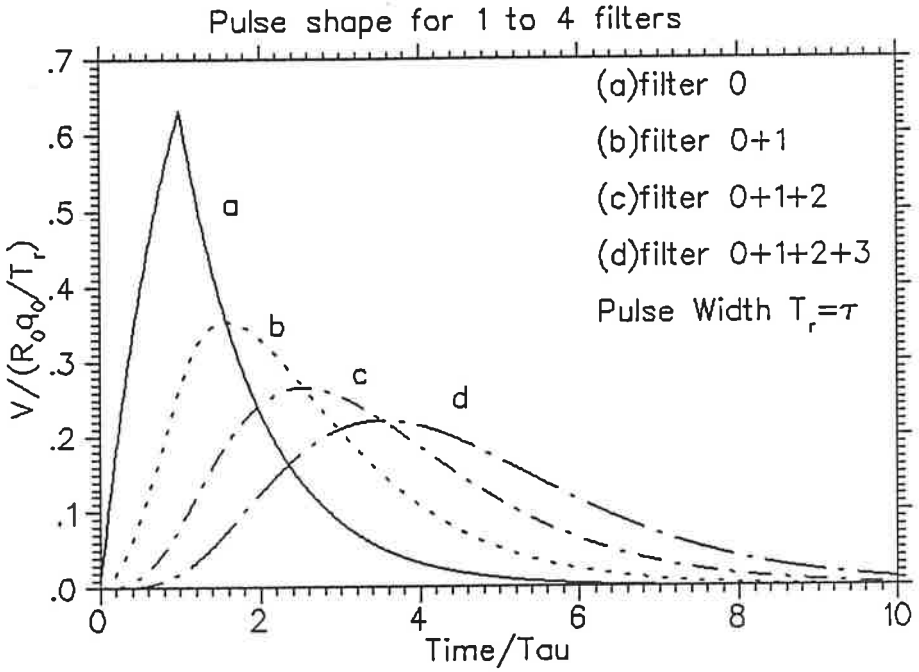

Figure B.2: Pulse shapes after filtering. Input is a rectangle pulse of width τ.

$$-[(1-(1+t/\tau+\frac{1}{2}(t/\tau)^2)e^{-t/\tau})U(t)]_{t-t_r}\} \tag{B.3}$$

$$V_3 = \frac{R_0q_0}{t_r}\{[(1-(1+t/\tau+\frac{1}{2}(t/\tau)^2+\frac{1}{6}(t/\tau)^3)e^{-t/\tau})U(t)]_t$$
$$-[(1-(1+t/\tau+\frac{1}{2}(t/\tau)^2+\frac{1}{6}(t/\tau)^3)e^{-t/\tau})U(t)]_{t-t_r}\} \tag{B.4}$$

The resulting curves are shown in figure B.2.

The noise after each filter is easier to compute than the pulse shapes. Assuming the noise from the PMT is evenly distributed over all frequencies, we can integrate the filter response over all frequencies to get the total noise voltage. Doing this gives the following result:

$$< V_{n,noise}^2 >= \frac{I_{\text{back}}GeR_0^2}{D_n\tau} \tag{B.5}$$

where I_{back} is the PMT anode current due to background light and dark current

and the D_n are constants that come from carrying out the integrals:

$$\begin{aligned} D_0 &= 2 \\ D_1 &= 4 \\ D_2 &= 16/3 \\ D_3 &= 32/5. \end{aligned}$$

Dividing the maximum pulse height by the noise, we arrive at the S/N ratios:

$$\frac{V_{n,peak}}{< V^2_{n,noise} >^{\frac{1}{2}}} = \frac{N_P}{N_B^{1/2}} \left[D_n^{1/2} (\frac{\tau}{t_r})^{1/2} P_n(\frac{\tau}{t_r}) \right] \tag{B.6}$$

where

P_n = the peak pulse voltage after n filters,

N_B = the number of background photoelectrons in time t_r,

N_P = the number of photoelectrons due to the signal.

The quantity in the brackets in equation B.6 can be used as a figure of merit, which is plotted in figure B.3. It is interesting to see that while adding more filters does slightly improve the best S/N ratio if the signal's pulse width is restricted to an optimal range, it does so at the expense of the S/N ratio for pulse widths that are off the optimum. Since the actual pulse widths in this experiment are likely to be highly variable, this is an undesirable feature of multi-stage filtering. We conclude that a single stage of filtering is best for this experiment, especially when one takes into account the practical problems involved in installing and debugging extra filter and amplification stages.

Another benefit of having only the zeroth stage of filtering is that for fast pulses, the pulse height will be proportional to the charge which, in turn, is proportional to number of photons in the event causing the pulse. This allows easy data analysis. Also, the rise time of the pulse will be equal to the time duration of the original photon event.

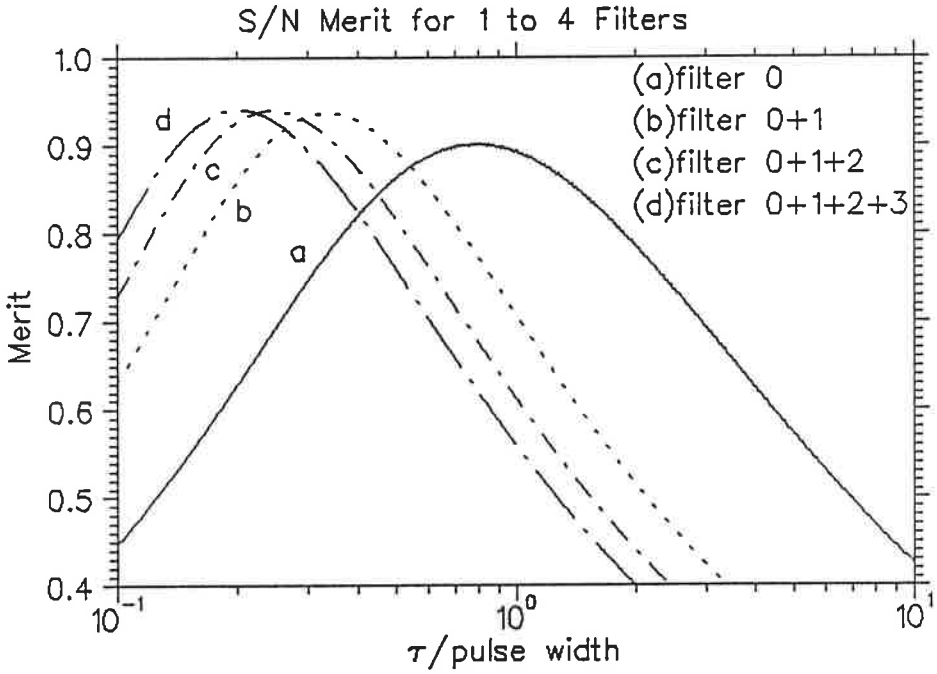

Figure B.3: Relative effectiveness for increasing number of filter stages. The horizontal axis is the ratio of the filters' time constant to the signal width.

B.2 *F*-Fold Logic

B.2.1 *F*-Fold Coincidence

One of the oldest techniques in particle detection is the coincidence circuit. If one has noisy detectors that randomly produce "false" signals one can still achieve reliable particle detection by looking at when F of these detectors simultaneously see something. As F increases, the probability of a coincidental simultaneous signal from all the detectors drops drastically while the probability of detecting a given particle remains high (assuming, of course, that the particle is sufficiently penetrating to traverse all the detectors).

If R_s is the "singles" rate, that is the average rate at which each detector sees "false" events, and we are using F-fold coincidence, then the rate R_{acc} at which accidental triggering will occur is

$$R_{acc} = F R_s^F \tau^{F-1} \tag{B.7}$$

$$= F\{\frac{1}{\tau}P(N_B > N_T)\}^F \tau^{F-1} \tag{B.8}$$

$$= \frac{F}{\tau}\{P(N_B > N_T)\}^F, \tag{B.9}$$

where τ is both the width of the discriminator outputs and a characteristic time which is determined by the detector and filter bandwidths as discussed in the previous section. N_B is the number of PMT photoelectrons due to background light received in a time interval τ and B_T is the number of photoelectrons that must be received in time interval τ in order to trigger a discriminator. Because the arrival time of background-light photons (and thus PMT photoelectrons) is random and obeys Poisson statistics, the number of photoelectrons in time interval τ has a Gaussian distribution. Therefore $P(N_B > N_T) = \frac{1}{2}\,\mathrm{erfc}(T)$ where $T = (N_T - \overline{N_B})/\sqrt{2\overline{N_B}}$ where $\overline{N_B}$ is the average number of photoelectrons in time τ.

So R_{acc} is the rate at which an experiment will "mistakenly" think an event has occurred when actually it was only a coincidence of noise fluctuations.

We must now consider the odds that a *real* event will be detected. If N_P is the number of "real event" photons (all arriving in time τ), then the F-fold trigger probability (or reliability) P_F is:

$$P_F = [P(N_B + N_P > N_T)]^F. \tag{B.10}$$

If one decides that a certain maximum rate, R_{acc}, of accidental triggers is acceptable, then, all other parameters being fixed, one can find the value of N_T which achieves this rate. (This is equivalent to adjusting the discriminator levels.) One can use this value of N_T to compute the reliability, P_F, for a given event size N_P. Figure B.4 shows this for $F = 4, 5$ and 6 in curves a, b and g, respectively. It can be seen that of these choices, $F = 6$ gives the best reliability, thus confirming the old rule-of-thumb of experimental particle physics, that the higher F is, the better[1].

Late in the course of the testing of the SLD experiment it was pointed out by Prof. Hill and Prof. Hsieh that the trigger reliability could be improved by using 4-of-6 or 5-of-6 triggering. This is because the signal being small, and somewhat buried in the noise, the odds that one of the 6 discriminators would *not* trigger was significant. This problem manifested itself as a poor trigger ($\approx$ 70%) reliability on test flashes. We will discuss this type of triggering next.

B.2.2 M-Out-of-F-Majority Logic

Now we shall consider the advantages of not requiring that all, but only a portion, of the discriminators trigger. M is the minimum number that must trigger, and is the called the Majority level.

[1]Up to a point, that is. If F is too large, then the small chance that a detector will fail to see a real particle becomes significant.

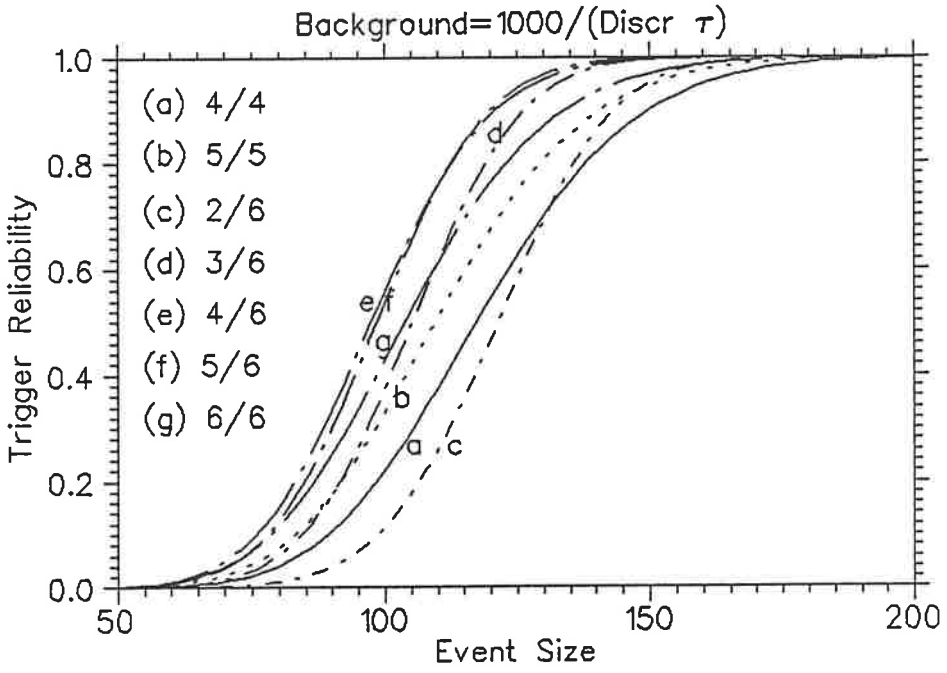

Figure B.4: Reliability of triggering using M of F (M/F) Majority Logic. Each logic combination has been adjusted to give 0.001 accidental triggers per second. Note that the best performance is given by 4 of 6 and 5 of 6 majority logic.

The probability $P_{M,F}$ that M discriminators out of F will trigger is

$$P_{M,F} = \frac{F!}{(F-M)!M!} p^M q^{F-M} \tag{B.11}$$

where $p \equiv P(N_B + N_P > N_T)$ is the probability of the combined noise and signal triggering a given discriminator, and $q \equiv 1 - p$ is the probability of *not* triggering a given discriminator. The overall probability (or reliability) of M *or more* discriminators triggering is

$$P_{M,F,total} = P_{M,F} + P_{M+1,F} + P_{M+2,F} + \cdots + P_{F,F}. \tag{B.12}$$

The accidental rate is $R_{acc} = (F/\tau)P_{M,F,total}$, where τ is the same time constant as in the previous section. In the limit of $M = F$ these equations reduce to the results of the previous section. The resulting reliability for $F = 6, M = 2, 3, 4, 5$ are graphed in figure B.4 where it can be seen that over a limited range the trigger reliability can be improved by typically 25% if M is chosen to be 4 or 5. As it happens, the SLD experiment is forced to work in this range since we are trying to detect very faint signals in a sea of photoelectron shot noise.

One might ask: is this always the case? Is $M \approx \frac{4}{6}F$ always going to give better results? It appears that the answer is yes. Figure B.5 shows the same results but with the requirement of a ten times lower accidental rate. Figure B.6 show the same results but for twice as many inputs (and adjusted for half as many photons entering each detector). Each case is consistent with the proposition that $M \approx \frac{4}{6}F$ is a close to optimal setting for N-fold majority logic.

B.3 An Alternative to Majority Logic

The question of noise analysis and trigger rates is fraught with confusion and the discussion within our group was ongoing. Mr. Chen brought up the point: why separately trigger on each signal and then use a complicated logic scheme to decide

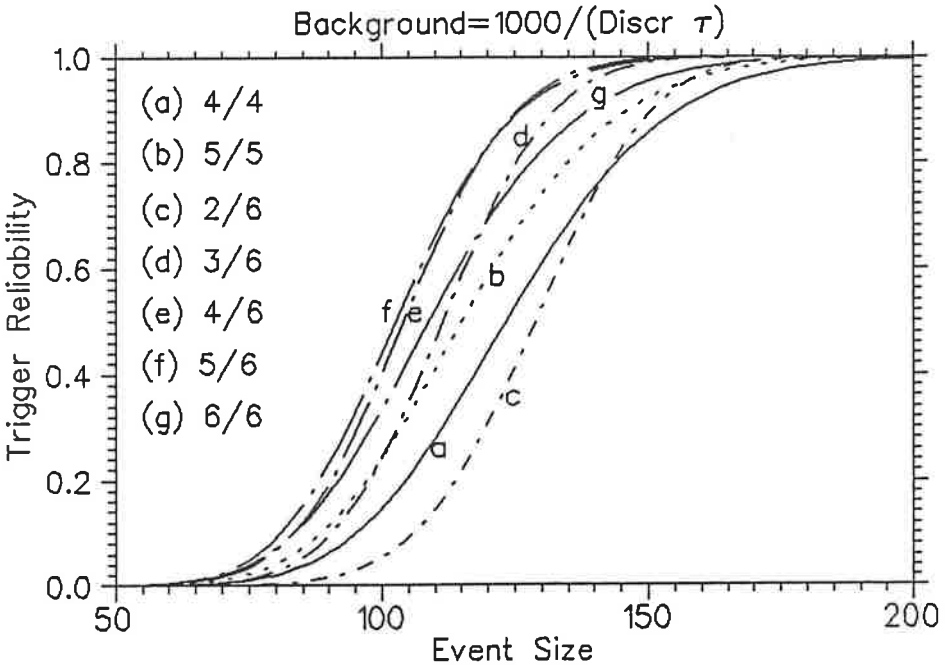

Figure B.5: Reliability of triggering using M of F (M/F) Majority Logic. Each logic combination has been adjusted to give 0.0001 accidental triggers per second.

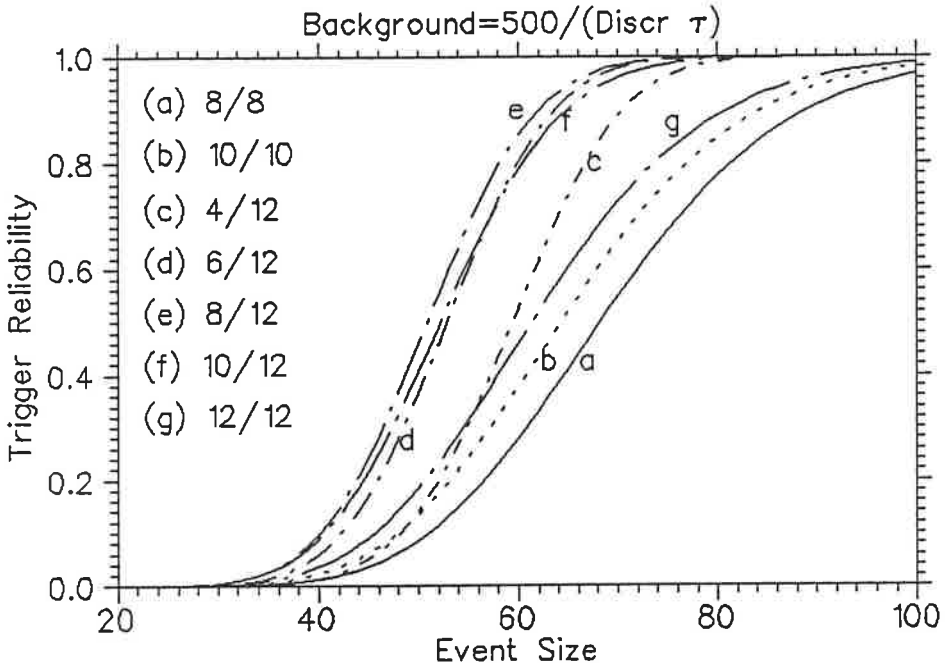

Figure B.6: Reliability of triggering using M of F (M/F) Majority Logic with twice as many inputs. Each logic combination has been adjusted to give 0.001 accidental triggers per second. Note that the best performance is given by 8 of 12 majority logic.

whether to trigger? Indeed, why not take the naive approach and simply linearly add the signals and use a single discriminator to trigger on the sum exceeding a threshold value? The initial reaction of most particle physicists to that idea would be no, that defeats the whole point of coincidence logic. However, the author did run the computer code that generated the curves of the previous section and found (to his great surprise) that the reliability of such a scheme would be slightly better than the best majority logic combinations. (We are comparing schemes with equal numbers of inputs.) So perhaps simply triggering on the sum of the six PMT signals of the SLD would be just as effective as the 4-out-of-6 logic in use up until the present time. This would allow a small cost savings in future SLD projects and simplify the electronics.

A preliminary test of this triggering arrangement has confirmed its effectiveness. However, we have found that individual PMTs see large pulses which are presumably due to Cherenkov light or particles passing through the photocathodes. These pulses trigger the system which is undesirable. As discussed in section 5.2, this problem could be eliminated by online data analysis.

Appendix C

Cosmic Ray Detectors

The detection of cosmic rays is a venerable subject dating back to the 1920's and the pioneering advances in modern physics of those days. This subject is well treated in various texts such as [2] and [32] so we will only list them below for the sake of comparison with the new type of detector that is the subject of this dissertation. At the end of this section there is table C.1 which summarizes the relative detection areas and costs of the available techniques.

Cloud Chambers

Principle: Consists of a vessel filled with gas such as argon super-saturated with a fluid, such as ethyl alcohol. Ions produced by the passage of charged particles provide nucleation points for liquid droplets marking the path. The positron was first seen in this type of apparatus with an added magnetic field for charge identification. Acceptance: $\approx$1 m^{2}sr.

Photographic Emulsion

Principle: Consists of stacked layers of silver-based photographic emulsion which is sensitive to ionizing particles (as well as to light) which are left for long periods of time (typically months) at mountain locations or are taken aloft by balloons. Emulsion layers are later developed and examined for particle tracks. Charge identification is possible because the density of the tracks scales as Z^2. Acceptance:

$\approx$10 m^2sr.

Radiation Sensitive Plastic

Principle: This is a modern analog of the photographic emulsion technique. Consists of sheets of plastic which can be radiation damaged by cosmic rays. Development is done by etching in acid to reveal the particle tracks. This type of experiment is presently orbiting earth in the Long Duration Exposure Facility which was launched in 1984. It is due for retrieval by the space shuttle in November of 1989 [33]. Acceptance: $\approx$10 m^2sr, but detects only very heavily ionizing tracks due to heavy nuclei, fission fragments etc.

Geiger Counters.

Principle: A strong electric field is set up in a gas by two high voltage electrodes. Passage of a charged particle provides enough ions to destabilize the gas initiating a discharge. Charge identification is not possible with this technique. Acceptance: $<$10 m^2sr.

Multi-Wire Proportional Chambers.

Principle: Again a strong electric field is established in a gas, however a spark quenching "cocktail" of organic vapors is added and the high voltage is carefully monitored so that the output pulse is proportional to the initial ionization. Ions from passing particles are collected by wire arrays and readout electronics, providing position and, if a magnetic field is present to make a spectrometer, charge information. Acceptance: $\approx$10 m^2sr.

Scintillators

Principle: Organic liquid or plastic doped with organic compounds that fluoresce when excited by the passage of ionizing particles are coupled to sensitive photodetectors, usually photomultiplier tubes. Although the amount of light produced does in principle scale as Z^2, fluctuations in the light detected and nonlinearity of response severely limit this approach to charge identification. Finely divided arrays of scintillators can be arranged to provide timing and, if a magnetic field is available to make spectrometer, charge information. Acceptance: $\approx$10 m^{2}sr

Large Scintillator Arrays

Principle: Large numbers of scintillators are scattered over hundreds of square kilometers to create a very large effective area. This technique uses the fact that UHE cascades have large lateral spreads so that even if the core of the shower misses a scintillator, the "halo" of electrons and positrons will still be detected. Thus arrays with scintillator spacings on the order of 1 km are workable. The largest array ever built, located in Adelaide (Australia) has an acceptance of 10^8 m^{2}sr. (This array is not longer operating, but there are plans tp expand the Akeno (Japan) array to a similar scale.)

Cherenkov Detectors

Principle: Relativistic charged particles passing through a medium at a velocity $v > c/n$, where n is the index of refraction of light in the medium, will produce a pulse of Cherenkov light in the forward direction. This light tends to be brightest in the visible and U.V. so photomultiplier tubes are typically used to detect it. The amount of light produced is a sensitive function of the velocity of the particle and scales as Z^2, so it is often used in conjunction with scintillators and magnetic fields to provide mass and charge information. Acceptance: $\approx$10 m^{2}sr.

Cherenkov Telescopes

Principle: Very high energy ($E > 10^{13}$ eV) particles impinge on the top of the atmosphere and form electromagnetic cascades, and the e^+ and e^- particles emit Cherenkov light in the forward direction. A large mirror system collects this light and focuses it on photomultiplier tubes. The mirrors are actually observing Cherenkov light emitted at high altitude so in a sense the actual detector is the air in the field of view. A representative system such as the one on Mount Hopkins [34], has a mirror radius $\approx$ 75 m^2 and a field of view full angle $\approx 3.5°$. It will trigger at 50% efficiency for events whose axis passes about 100 meters from the detector and whose direction is up to 2° off the optical axis. This converts to an acceptance of $\approx$120 m^{2}sr. (The effective area would grow somewhat for higher energy primaries.)

Looking at the numbers this way does not express what such an instrument is *really* good at, which is the high sensitivity observation of a point source of cosmic rays, once its position is known. Acceptance: $\approx$100 m^{2}sr.

Thermo-Accoustic Detection

Principle: Shower cores from UHE events would deposit a fraction of their energy in the form of heat in a large container of some homogeneous material such as a pool of water or mineral oil [35]. Since the some events have on the order of a Joule of energy to begin with, even with very low conversion efficiency an appreciable amount of thermal energy is available. This would cause sudden thermal expansion detectable by hydrophones as an accoustic pulse. The author has participated in an attempt to make this technique work, but with disappointing results. It appears that the available accoustic energy was smaller than we expected. Acceptance: $\approx$ 5 m^{2}sr, however 100 km^2 would be possible if a large body of water, such as a lake, could be used.

Table C.1: Summary of available cosmic ray detection techniques.

Technique	Approximate Acceptance	Approximate Cost
Cloud Chambers	1 m^2sr	10^8 \$/km^2sr
Photographic Emulsion	10 m^2sr	10^7 \$/km^2sr†
Radiation Sensitive Plastic	10 m^2sr	10^6 \$/km^2sr†*
Geiger Counters	10 m^2sr	10^9 \$/km^2sr
Multi Wire Proportional Chambers	10 m^2sr	10^9 \$/km^2sr
Scintillators	10 m^2sr	10^8 \$/km^2sr
Large Scintillator Arrays	$10^8 m^2sr$	10^5 \$/km^2sr
Cherenkov Detectors	10 m^2sr	10^8 \$/km^2sr
Cherenkov Telescopes	100 m^2sr	10^5 \$/km^2sr
Thermo-Accoustic	Not available	
Atmospheric Electric	Not available	
Air Fluorescence Detection		
– – – Fly's Eye	$10^8 m^2sr$	10^4 \$/km^2sr
– – – Side Looking Detector	$10^8 m^2sr$	10^3 \$/km^2sr

†Limited to a single limited-duration exposure.
*Sensitive to heavy nuclei only.

Atmospheric Electric Detection

Principle: The atmosphere normally has a vertical electrical field of about 200 V/m. An UHE cosmic ray cascade might create enough ions to measurably disrupt this electric field. The author has also been involved in an attempt to make this technique work [20], again with disappointing results.

Air Fluorescence Detection

Principle: This is the approach the present technique is based upon. It is summarized in section 1.3.

Appendix D

Design Details

D.1 Mirror Design

The mirrror used in the SLD was designed to give a large light collecting area and reasonable accuracy at a minimal cost.

We started with two 4 ft by 8 ft by 1/8 in thick Plexiglass or acrylic mirrors (nominal dimensions; actual dimensions were 294 cm by 125 cm). The front surface of the Plexiglass came coated with aluminum and a thin protective layer of lacquer [36].

The mirrors were reinforced by a series of horizontal plexiglass "T"–shaped bars glued to the back side. As shown in figure D.1, each mirror has 19 T-bars above and below the center line. (The figure D.1 shows 18 T-bars, each, above and below; the discrepancy is due to the difference between the actual and nominal dimensions.) Figure D.2 shows how the T–bars were glued to the mirrors. The mirrors were provided with a fixed support at the center line where each was glued to a 3/4 inch thick by 2 inch wide bar of Plexiglass bolted to the steel Unistrut [37] framework behind the mirrors. The glue used for bonding the mirror to the T-bars and the support bar was silicone rubber [38], which provides a flexible bond that allows the mirror to bend without cracking the glue. (Note that the plexiglass-silicone rubber bond is not very resistant to pulling forces which could detach the T-bars from the mirror.)

The figure of each mirror was adjusted by turning wing-nuts on the threaded

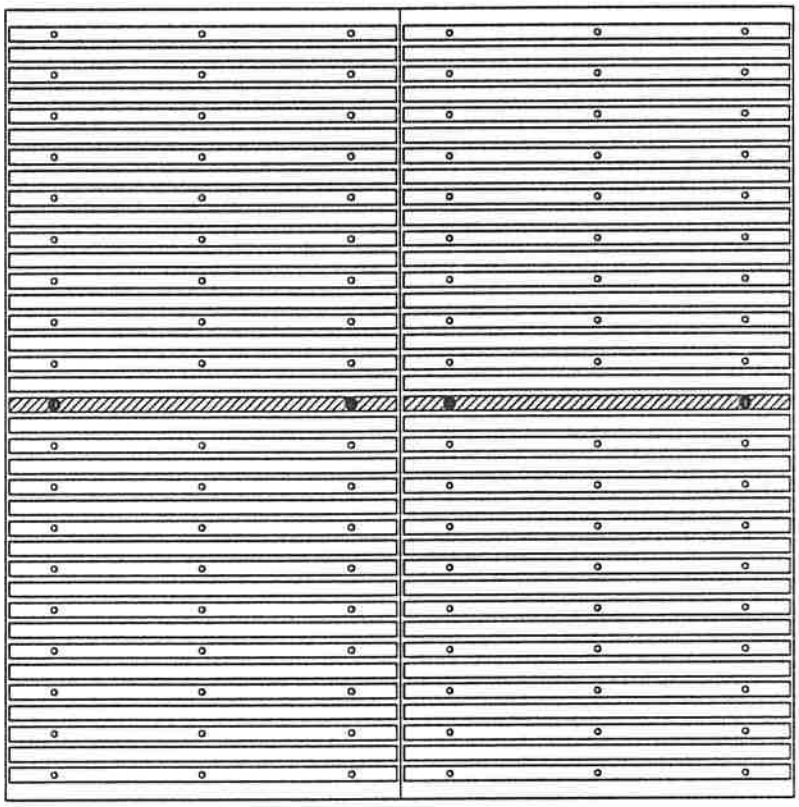

Figure D.1: Back view of the SLD's mirror which consists of two side-by-side units. Also shown are the horizontal reinforcing T-bars (open rectangles), adjustment locations (small circles) and fixed support bars (shaded rectangles).

rods connecting the T-bars to the steel framework. The positions of the adjustment rods are marked in figure D.1 as small open circles which are attached to alternate T-bars, as shown.

The focal length of the mirror had to be very short, 1.8 m, in order to fit the entire system inside the trailer. This meant that the mirrors had a pronounced curvature, with the center being about 23 cm behind an imaginary straight line connecting the edges.

As shown in figure D.2, we had originally designed the mirrors such that every T-bar had adjustments, one at each end of the bar. We later found that it was

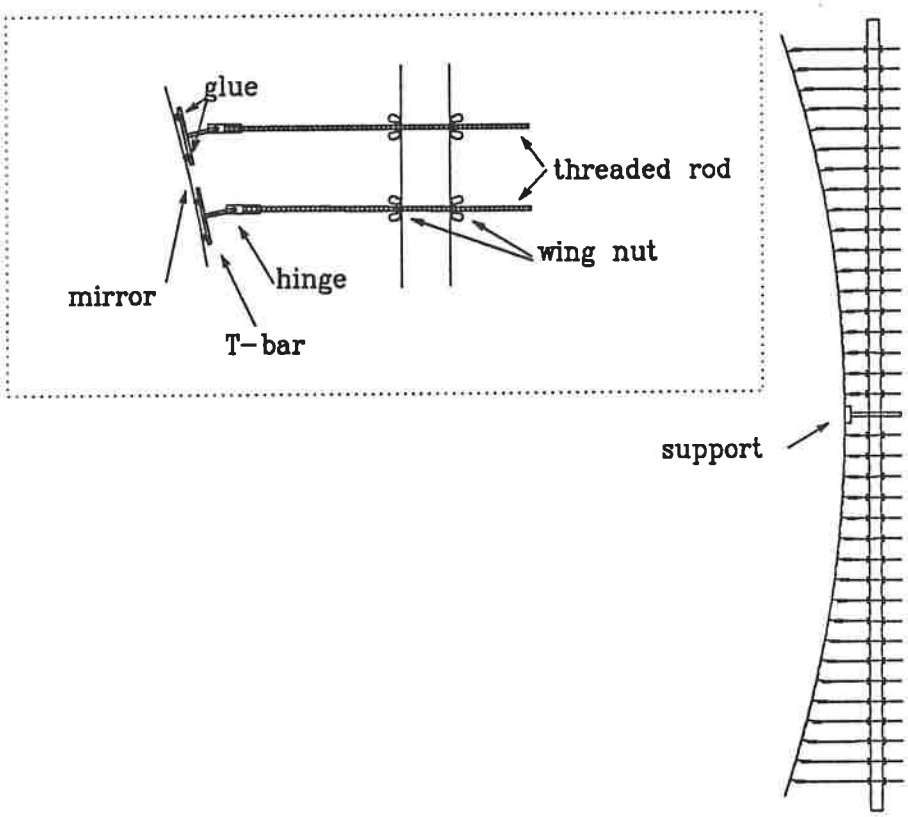

Figure D.2: Side view of the mirror assembly and expanded detail showing how the reinforcing T-bars were glued and positioned with adjustment rods. Rotating the wing-nuts pushed or pulled the mirror to achieve a parabolic profile. (Only alternate adjustment rods were used in the actual prototype.)

not necessary to have every T-bar adjustable and, in fact, the mirror adjustment improved when only every other T-bar was adjusted and the skipped bars were left "floating". But we did encounter a problem with the center of the mirrors sagging when the summer temperatures rose to ≈50° C. A third, middle row of adjustments [1] was added which effectively eliminated this problem. The positions of the adjustments that were actually needed are shown in figure D.1 as small open circles.

[1] One of our undergraduate students, Steve Syracuse, suggested and implemented this modification.

The only remaining problems with our mirrors were: (a) Small scale "ripples" which are probably caused by variations in the plastic and in the thickness of the glue bonding the T-bars to the mirrors. (b) Large aberrations at the horizontal centerline and top and bottom extremities which were not adjustable. These areas were masked off with black tape. (c) Large temperature changes in the SLD trailer caused the adjustments to drift, necessitating readjustments after each period when the temperature exceeded 30° C. Cold weather ($\approx$0° C) did not seem to affect the mirror adjustment.

Our experience with this mirror design is that while inexpensive in terms of materials, it is very expensive in man-hours needed to fabricate and adjust. The presence many adjustments made for a very long process of alignment.

Bibliography

[1] A.M. Hillas. In T. Gaisser, editor, *Proceedings of the Cosmic Ray Workshop*, University of Utah, January 1983. Bartol Research Foundation, Newark, DE.

[2] M.S.Longair. *High Energy Astrophysics.* Cambridge University Press, 1981.

[3] Christopher T. Hill, David N. Schramm, and Terry P. Walker. Technical Report FERMILAB-Pub-86/146-T, Fermi National Accelerator Laboratory, November 1986.

[4] Kenneth Greisen. *Physical Review Letters*, 16(17), April 1966.

[5] R. M. Baltrusaitis et al. *Physical Review Letters*, 54(16), April 1985.

[6] V. S. Berezinkii and S. I. Grigor'eva. *Soviet Astronomy Letters*, 14(1), January 1988.

[7] J.R.Jokipii and G.Morfill. *Astrophysical Journal*, 312:170–177, January 1987.

[8] Bertram Schwarzschild. *Physics Today*, pages 17–21, November 1988.

[9] B.L. Dingus et al. *Physical Review Letters*, 61(17), October 1988.

[10] Alan N.Bunner. *Sky and Telescope*, 34(4), October 1967. (This article contains the first mention of the term "Fly's Eye" in reference to an optical cosmic ray detector).

[11] Kenneth Greisen. Technical Report Final Report, AEC Contract No. AT(30-1)-3038 and AT(11-1)-3157, Laboratory of Nuclear Studies, Cornell University, May 1972.

[12] H.E.Bergeson, J. C. Boone, and G. L. Cassiday. In *14th International Cosmic Ray Conference*, volume 8, pages 3059–3063, Munich, Germany, August 1975.

[13] Pierre Sokolsky. *The Physics Teacher*, April 1985.

[14] J.L. Elliot. *Atmospheric Fluorescence as a Ground Based Method of Detecting Cosmic X-Rays.* PhD dissertation, Harvard University, Department of Astronomy, January 1972.

[15] C. L. Bhat. *Detection of Cosmic X-Ray and Gamma-Ray Bursts Through Atmospheric and Cerenkov Techniques.* PhD dissertation, University of Kashmir, Bhabha Atomic Research Centre, India, August 1982.

[16] R. Cady et al. In *18th International Cosmic Ray Conference*, volume 9, pages 351–354, Bangalore, India, August 1983.

[17] Eugene Loh. Verbal communication, results of measuring mirror samples on the fly's eye equipment test apparatus. August 1988.

[18] B. Barish et al. *IEEE Transactions on Nuclear Science*, NS-25(1):532–536, February 1978.

[19] V. Eckardt et al. *Nuclear Instruments and Methods*, 155:389–398, 1978.

[20] Chuxing Chen. *Local Atmospheric Electricity and its Possible Application in High Energy Cosmic Ray Air Shower Detection.* PhD dissertation, University of Arizona, Department of Physics, August 1989.

[21] Kenneth Greisen. *The Extensive Air Showers*, volume 3 of *Progress Cosmic Ray Physics*, chapter 1, pages 3–141. North-Holland Publishing Company, 1956.

[22] Dwight E. Gray, editor. *American Institute of Physics Handbook.* McGraw-Hill Book Company, 1972.

[23] Pierre Sokolsky. *Introduction to Ultrahigh Energy Cosmic Ray Physics.* Addison-Wesley Publishing Company, Inc, 1991.

[24] G. Davidson and R. O'Neil. *The Journal of Chemical Physics*, 41(12), December 1964.

[25] Paul L. Hartman. *Planetary and Space Science*, 16(11):1315–1340, 1968.

[26] A.Lyle Broadfoot and Kenneth R. Kendall. *Journal of Geophysical Research, Space Physics*, 73(1):426–428, January 1968.

[27] T. Bowen and P. Halverson. In *Proceedings on the Workshop on Cosmic Ray and Gamma Ray Experiments for the Space Station Era*, pages 363–371, Lousiana State University, Baton Rouge, LA, October 1984.

[28] George L. Cassiday. Verbal communication. March 1989.

[29] *The Times Atlas of the World.* Houghton Mifflin Books (1957) and Times Books Limited (1985). (The 1957 edition of the Times Atlas has more detailed topographical information.).

[30] RCA Solid State Division. *RCA Electro-Optics Handbook.* Burle Industries, Inc., Lancaster, Pensylvania, 1974.

[31] Rudolf Kingslake. *Applied Optics and Engineering.* Academic Press, 1965.

[32] Bruno Rossi. *High–Energy Particles.* Prentice–Hall, Inc., 1952.

[33] J. Eberhart. *Science News*, 135(1), January 1989.

[34] Trevor Weekes. Verbal communication. February 1989.

[35] Raymond Bell and Theodore Bowen. In *19th International Cosmic Ray Conference*, volume 8, pages 322–324, La Jolla, USA, August 1985.

[36] Mir-Acryl Company. The lacquer overcoating feature is called an "Armadillo" coating by Mir-Acryl.

[37] Unistrut Building Systems. We selected the 1 5/8 inch Unistrut system for our mirror framework.

[38] Silicone rubber glue. For example: General Electric or Dow Corning RTV, sold in hardware stores under various labels as silicone bathtub sealant.